DEPARTMENT OF ELECTRONIC AND ELECTRICAL ENGINEERING
FACULTY OF ENGINEERING
LOUGHBOROUGH UNIVERSITY

IMAGING PHOTOPLETHYSMOGRAPHY: TOWARDS EFFECTIVE PHYSIOLOGICAL MEASUREMENTS

BY

YU SUN

A Doctoral Thesis
Submitted in partial fulfilment of the requirements for the award of
Doctor of Philosophy of Loughborough University

September 2011

Supervisor: Dr. Sijung Hu
Co-supervisor: Prof. Jonathon Chambers
Department of Electronic & Electrical Engineering

For my parents and dear wife

"*There is no royal road to science, and only those who do not dread the fatiguing climb of its steep paths have a chance of gaining its luminous summits.*"

----- **Karl Marx**

Loughborough University

CERTIFICATE OF ORIGINALITY

This is to certify that I, Yu SUN, am responsible for the work submitted in this thesis, that the original work is my own except as specified in acknowledgements or in references, and that neither the thesis nor the original work contained therein has been submitted to this or any other institution for a higher degree.

…… (Signed)

……. (Date)

ABSTRACT

Since its conception decades ago, Photoplethysmography (PPG) – the non-invasive opto-electronic technique that measures arterial pulsations *in-vivo* – has proven its worth by achieving and maintaining its rank as a compulsory standard of patient monitoring. However successful, conventional contact monitoring mode is not suitable in certain clinical and biomedical situations, e.g., in the case of skin damage, or when unconstrained movement is required. With the advance of computer and photonics technologies, there has been a resurgence of interest in PPG and one potential route to overcome the abovementioned issues has been increasingly explored, i.e., imaging photoplethysmography (iPPG).

The emerging field of iPPG offers some nascent opportunities in effective and comprehensive interpretation of the physiological phenomena, indicating a promising alternative to conventional PPG. Heart and respiration rate, perfusion mapping, and pulse rate variability have been accessed using iPPG. To effectively and remotely access physiological information through this emerging technique, a number of key issues are still to be addressed. The engineering issues of iPPG, particularly the influence of motion artefacts on signal quality, are addressed in this thesis, where an engineering model based on the revised Beer-Lambert law was developed and used to describe opto-physiological phenomena relevant to iPPG.

An iPPG setup consisting of both hardware and software elements was developed to investigate its reliability and reproducibility in the context of effective remote physiological assessment. Specifically, a first study was conducted for the acquisition of vital physiological signs under various exercise conditions, i.e. resting, light and heavy cardiovascular exercise, in ten healthy subjects. The physiological parameters derived from the images captured by the iPPG system exhibited functional characteristics comparable to conventional contact PPG, i.e., maximum heart rate difference was <3 bpm and a significant ($p < 0.05$) correlation between both measurements were also revealed. Using a method for attenuation of motion artefacts, the heart rate and respiration rate information was successfully assessed from different anatomical locations even in high-intensity physical exercise situations. This study thereby leads to a new avenue for noncontact sensing of vital signs and remote physiological assessment, showing

clear and promising applications in clinical triage and sports training.

A second study was conducted to remotely assess pulse rate variability (PRV), which has been considered a valuable indicator of autonomic nervous system (ANS) status. The PRV information was obtained using the iPPG setup to appraise the ANS in ten normal subjects. The performance of the iPPG system in accessing PRV was evaluated via comparison with the readings from a contact PPG sensor. Strong correlation and good agreement between these two techniques verify the effectiveness of iPPG in the remote monitoring of PRV, thereby promoting iPPG as a potential alternative to the interpretation of physiological dynamics related to the ANS.

The outcomes revealed in the thesis could present the trend of a robust non-contact technique for cardiovascular monitoring and evaluation.

ACKNOWLEDGEMENTS

I would like to express my sincere gratitude and appreciation to the following people who have contributed tirelessly to rendering this work possible:

- First and foremost, I want to thank my parents and dear wife, whose unconditional love and unwavering support during the past years has played a critical role in the completion of this research.

- It gives me great pleasure to acknowledge my supervisor, Dr. Sijung Hu for his greatest leadership and guidance during my entire PhD studies. It has been a privilege to be under his supervision, whose contributions have gone well beyond the scope of this work.

- I also want to express my thanks to Prof. Stephen Greenwald, Queen Mary, University of London, for his suggestions, discussions and great help of the clinical study in Royal London Hospital and London Chest Hospital.

- I would like to express my sincere thanks to Prof. Yisheng Zhu, and Prof. Shanbao Tong, Shanghai Jiao Tong University, for their heuristic discussions and undying support during the lonely PhD period abroad.

- Besides, I wish to express my gratitude to Prof. Jonathon Chambers, my co-supervisor who is always willing to help me in broadening my scope in research and improving my English writing skills.

- Members of the Photonics Engineering and Health Care Technology Group deserve thanks for their effort to make the laboratory an environment conducive for learning and numerous enlightening discussions and advices. I am also grateful to Dr. Vicente Azorin-Peris and Charlotte Papin for their personal contribution to this research and for countless lessons and discussions in engineering and life.

- Finally, I am grateful to Loughborough University and Shanghai Jiao Tong University for their support.

TABLE OF CONTENTS

SECTION 2 METHODOGY

SECTION 3 EXPERIMENTS

LIST OF TABLES

LIST OF FIGURES

ACRONYMS

ANOVA	Analysis of variance
ANS	Autonomic nervous system
BP	Blood pressure
BMI	Body mass index
CCD	Charge coupled device
CMOS	Complementary metal oxide semiconductor
CO	Cardiac output
cPPG	Contact photoplethysmography
DBP	Diastolic blood pressure
DE	Dynamical embedding
DFA	Detrended fluctuation analysis
ECG	Electrocardiograph
EEG	Electroencephalogram
fMRI	Functional magnetic resonance imaging
FT	Fourier transform
Hb	Hemoglobin
HbO_2	Oxyhemoglobin
HF	High frequency components of HRV (0.15-0.4 Hz)
HF_{nu}	HF expressed in normalized units (n.u.)
HR	Heart rate
HRV	Heart rate variability
IC	Independent component
ICA	Independent component analysis
iPPG	Imaging photoplethysmography
IR	Infrared
PPG	Photoplethysmography
PRV	Pulse rate variability
LASCA	Laser speckle contrast imaging
LDI	Laser Doppler imaging
LED	Light emitting diode
LF	Low frequency components of HRV (0.04-0.15 Hz)
LF_{nu}	LF expressed in normalized units (n.u.)

MC	Monte Carlo
NIR	Near infrared
OCT	Optical coherence tomography
PP	Mean value of pulse to pulse intervals
PPI	Pulse-to-pulse interval
PSD	Power spectral density
PTT	Pulse transit time
PWV	Pulse wave velocity
QE	Quantum efficiency
RCLED	Resonant cavity light emitting diode
RIS	Ring-light illumination source
ROI	Region of interest
RR	Respiration rate
RTT	Radiative transport theorem
SaO_2	Blood oxygen saturation
SBP	Systolic blood pressure
SCICA	Single-channel independent component analysis
SDPP	Standard deviation of pulse to pulse intervals
SNR	Signal to noise ratio
SPWD	Smoothed pseudo Wigner distribution
SPWVD	Smoothed pseudo WVD
STFT	Short time Fourier transform
TFR	Time-frequency representation
WT	Wavelet transform
WD	Wigner distribution
WVD	Wigner-Ville distribution

SECTION 1 INTRODUCTION

1 SUMMARY OF RESEARCH

Optical assessment of physiological parameters is attractive for its simple, low-cost, convenience and continuous monitoring. Since its conception decades ago, photoplethysmography (PPG) such an optical biomonitoring technique that non-invasively measures arterial pulsations in-vivo has proven its usefulness by achieving and maintaining its rank as a standard of patient monitoring in anesthesia, recovery room and under intensive care. Although successful, the contact measurement has limited its applicability and halted its evolution to a near standstill over the last few decades. Therefore, it is worth to develop a remote diagnostic technique that could be used for contactless and effective cardiovascular system assessments.

1.1 BACKGROUND

Noninvasive biomedical monitoring and noninvasive medical diagnosis are preferred whenever possible to avoid the risks and expense associated with surgical opening of the body surface. Optical techniques, such as laser speckle imaging, laser Doppler, photoacoustic tomography, and photoplethysmography, which provide noninvasive physiological monitoring, seem to be a promising route for remote physiological assessments. Among those optical techniques, photoplethysmography (PPG), first introduced in the 1930's [1], has proved superior to others in assessing the blood volume variations in the microvascular tissue bed. Its ease of use, low-cost and convenience makes it an attractive area of research in the biomedical and clinical community for measuring oxygen saturation, blood pressure, cardiac output, heart rate and respiration rate, all of which are relevant parameters in the assessment of cardiovascular status. Although successful, conventional contact PPG is not suitable in situations of skin damage, i.e., burn, ulcer, trauma, or when free movement is required. Furthermore, it has been demonstrated that the spring-loaded clips affect the waveform of PPG signals by contacting force between the sensor and the measurement site [2, 3]. All these factors limit the applicability of PPG.

The past few years have witnessed a resurgence of interest in the PPG technique thanks to the latest advances in computing and photonics, as well as the better understanding of the interaction between tissue optics and physiology. One emerging technology, named imaging PPG (iPPG), has been recently proposed and already gained extensive interest in the remote assessment of cardiovascular physiology. Compared to conventional PPG, the iPPG technique offers added value by removing the primary limitations of spot measurement and contact sensing such as the physical restrictions, cabling, and lack of spatial characterisation associated with the latter approaches. As an emerging technique iPPG has a number of factors that limits its usefulness for routine clinical assessments.

This thesis presents a viable approach to effective non-contact physiological assessment by means of an iPPG setup consisting of hardware and software. The hardware element, consisting of light sources and digital camera arrangements, provides the empirical image recordings for processing using custom software algorithms. The PPG signal is known to be susceptible to motion-induced signal corruption, making the removal or attenuation of motion artefacts a key issue in iPPG signal processing. Pioneering iPPG studies to date have typically addressed motion artefacts by operating in still conditions and requiring subjects to be

motionless during recordings. This research also addresses the performance of several algorithms which were developed and used to compensate for motion artefacts in iPPG recordings prior to the extraction of physiological parameters.

Two experimental protocols were conducted for the effective assessment of the physiological parameters. In the first study, vital physiological signs under various exercise conditions, i.e. resting, light and heavy cardiovascular exercise, were obtained. The physiological parameters, e.g., heart rate and respiration rate, derived from the images captured by the iPPG system exhibited functional characteristics comparable to conventional contact PPG. Using a method for attenuation of motion artefacts, the physiological information was successfully assessed from different anatomical locations even in high-intensity physical exercise situations. This study thereby leads to a new avenue for noncontact sensing of vital signs and remote physiological assessment, showing clear and promising applications in triage and sports training. A second study was conducted to remotely assess pulse rate variability (PRV), which has been considered a valuable indicator of autonomic nervous system (ANS) status. The performance of the iPPG system in accessing PRV was evaluated via comparison with the readings from a contact PPG sensor.

1.2 AIMS AND OBJECTIVES

A mature imaging PPG (iPPG) technique ideally provides a wide variety of physiological assessments reliably, accurately, quickly, and under a range of operating conditions, i.e., in the presence of motion artefacts.

The aim of this research work is to **effectively and remotely assess physiological parameters related to the human cardiovascular system by means of imaging photoplethysmography** (iPPG).

For these aims, the following objectives are inferred in the context of this thesis:

1) ***To provide the background context of PPG/iPPG, from a biomedical engineering research perspective.*** For PPG the relevant concepts of tissue optics, physiology, principles of implementation, the applicability and the limitations are presented. While, for iPPG, recently introduced iPPG systems compared with advantages over conventional PPG, common research area and potential applications are also recounted (**Chapter 2**).

2) ***To illustrate the concepts relevant to tissue optics underlying physiology, and mathematically describe those which pertain to human tissue optics and the circulatory system.*** Currently used mathematical models such as radiative transport theorem (RTT) and Beer-Lambert law are detailed from the standpoint of the application in iPPG. The strengths and weaknesses of these models are discussed in order to develop an opto-physiological model particularly for iPPG signal processing (**Chapter 3**).

3) ***To establish the Imaging PPG setup to be applied in physiological studies.*** The experimental setup consisting of hardware and software elements, aims to provide detailed biomedical information, i.e. heart rate, pulse waveform, pulse transit time, for effective physiological assessments. Specifically, a series of studies pertaining to sensor design, light source and digital camera arrangement have been explored while the software was developed for the comprehensive processing of physiological signals. A methodology for motion artefacts attenuation was introduced to improve extraction of the physiological parameters. Furthermore, specific processing approaches for the pulse rate variability (PRV) analysis, considering trough detection, interpolation, re-sampling, and relevant time and frequency domain methods are detailed. (**Chapter 4**).

4) ***To interpret the experimental results of remote physiological assessments under exercise conditions.*** An experimental protocol targeting intensity, duration, and frequency of exercise is described, implemented, and evaluated for the recovery of physiological parameters from several anatomical locations under various exercise conditions (**Chapter 5**).

5) ***To interpret the experimental results of the remote assessment of pulse rate variability (PRV) with respect to the autonomic nervous system (ANS).*** Physiological signals captured remotely from the palm of the hand via iPPG were compared to contact PPG sensor results in the context of PRV assessment (**Chapter 6**).

6) ***To summarise the research trajectories indicated by the results of this research.*** Suggestions and recommendations are made for future studies in this area according to the findings of the experimental studies and iPPG setup (**Chapter 7**).

Referenced works are collected in a common section following the main body of the thesis. Appendices are included to provide theoretical and technical details about the volunteer information and anonymous laboratory trial form, camera configuration software front panel and image acquisition software front panel.

1.3 PERSONAL CONTRIBUTIONS

The original contributions of this thesis are focused upon a non-contact imaging photoplethysmography technique for effective physiological assessments. The novelty of the contributions is supported by one published full journal paper, one submitted full journal paper, one journal article in preparation, and two published conference papers. Personal contributions in this thesis can be summarized as follows:

1) A proprietary opto-physiological model for reflection PPG is created to theoretically reflect effective physiological assessment by means of imaging PPG setup (**Chapter 3**). The motion artefact dependent iPPG signal quality is also introduced to resolve practical issue for remote assessment.
2) The imaging PPG setup comprising hardware and operation package is introduced to implement two designated protocols (Exercise study and PRV) in collaboration with the existing platform. The post signal processing algorithms with, motion compensation, blind source separation, time-frequency representation, trough detection, and time/frequency-domain PRV analysis methods is developed to reflect these effective non-contact physiological assessments (**Chapter 4**).
3) One experimental protocol was to appraise the iPPG in remote physiological assessments during various motion states. Measurement setup, post-signal processing, and interpretation are generated to reach the practical physiological monitoring. The results demonstrate that the physiological measurements could be tracked with the help of image registration and blind source separation technique in different physical states (**Chapter 5**).
4) The iPPG system is configured to a fast mode to facilitate the non-contact pulse rate variability (PRV) assessments. The experimental protocol, measurement setup and post analysis are conducted to remotely assess the autonomic nervous system. The physiological parameters derived from iPPG system exhibit functional characteristics comparable to conventional contact PPG sensor, suggesting a potential route to remotely appraise the autonomic nervous activities (**Chapter 6**).

1.4 RELEVANT PUBLICATIONS

The following articles related to the work presented in this thesis have been published:

[1] **Y. SUN**, S. Hu, V. Azorin-Peris, J. Zheng, S. Greenwald, J. Chambers, Y. Zhu, (2010), "Detection of physiological changes after exercise via a remote opto-physiological imaging system", ***Proc. of SPIE***, San Francisco, 7891, pp: 13-20, 2011.

[2] **Y. SUN**, S. Hu, V. Azorin-Peris, S. Greenwald, J. Chambers, Y. Zhu, "Motion-compensated non-contact imaging photoplethysmography to monitor cardiorespiratory status during exercise", ***J. Biomed. Opt.***, Vol. 16(7), pp. 077010/1-9, 2011.

[3] **Y. SUN,** C. Papin, V. Azorin-Peris, R. Kalawsky, S. Greenwald, S. Hu, "Comparison of scientific CMOS camera and webcam for monitoring cardiac pulse after exercise", ***Proc. of SPIE***, San Diego, 8135, 813506-1, 2011.

[4] **Y. SUN,** C. Papin, V. Azorin-Peris, R. Kalawsky, S. Greenwald, S. Hu, "The use of ambient light in remote photoplethysmographic systems a comparison between a high performance camera and a low cost webcam", ***J. Biomed. Opt.,*** (Submitted).

[5] **Y. SUN**, S. Hu, V. Azorin-Peris, S. Greenwald, J. Chambers, Y. Zhu, "Remote pulse transit time measurement via imaging photoplethysmography", ***Opt. Express***, (Manuscript).

2 IMAGING PHOTOPLETHYSMOGRAPHY

Imaging PPG is an emerging medical imaging technique that non-invasively monitors blood perfusion in the microvascular bed of tissue. Compared to the conventional contact PPG, imaging PPG provides added information yet removes the primary limitations of spot measurement and contact sensing which might facilitate the continuous and real-time measurements of blood perfusion. However, it has a number of factors that limits its usefulness for routine clinical assessments. As such, these are potential areas of research when attempting to increase the reliability and applicability of the infant technology.

2.1 INTRODUCTION

Photoplethysmography (PPG) is a simple and low-cost optical bio-monitoring technique used to measure the blood volume changes that occur in the human body due to the pulsatile nature of the circulatory system [4]. PPG was introduced almost simultaneously by Hertzman in the United States and Matthes and Hauss in Germany in the 1930s [5]. As the pioneers who helped establish the PPG technique, Hertzman and colleagues first introduced the term 'photoplethysmography' and suggested that it represented the volumetric changes ('plethysmo' means enlargement in Greek) in the dermal vasculature [1]. Since its conception decades ago, its ability of real time monitoring vital physiological parameters, i.e., pulse oximetry, heart/respiration rates, blood pressure and cardiac output, has made PPG a standard of patient monitoring during anaesthesia, in recovery room and under intensive care. Besides, it has also proven its usefulness in the vascular diagnostics and autonomic functions assessment.

2.2 PRINCIPLES OF PHOTOPLETHYSMOGRAPHY

PPG is the core technology upon which imaging PPG (iPPG) is based. Hence, an introduction of the fundamental concepts related to PPG could help to illustrate the principles of iPPG and reveal the development of iPPG technique. In order to better understand the PPG technique, a basic knowledge of the human circulatory system and of the optical properties of human tissue is required and will be detailed in this section.

2.2.1 Background Physiology

The human circulatory system, which essentially includes the heart, lungs and vascular tree, is an organ system that delivers the oxygen, nutrients, and hormones to the cells in the body and removes the waste products from the cells. It also plays a part in the immune system of the body and helps stabilize body temperature and pH to maintain homeostasis. The closed path of blood circulation is as follows: the heart pumps deoxygenated blood out of the right ventricle into the lungs via the pulmonary arteries. In the lungs, carbon dioxide is released from the blood and replaced by oxygen. Four pulmonary veins, two draining each lung, carry the oxygenated blood to the left atrium of the heart. The oxygenated blood from left atrium then passes to the left ventricle from which the blood is pumped to the whole body via the arteries. After the oxygen in the blood is released and consumed in the tissue and organs of the body and carbon dioxide is

collected, the blood returns to the right atrium via the veins, where it passes to the right ventricle through the tricuspid valve and the cycle repeats. Blood circulation as described above contains two circuits: pulmonary and systemic circulation as shown in Figure 2.1. Specifically, the pulmonary circulation transports oxygen-depleted blood away from the heart to the lungs and returns oxygenated blood back to the heart while systemic circulation delivers oxygenated blood away from the heart to the rest of the body and returns oxygen-depleted blood back to the heart. A heart cycle covers two heart beats; during systole, the heart pumps blood both to the body and to the lungs, while during diastole, both ventricles fill with blood.

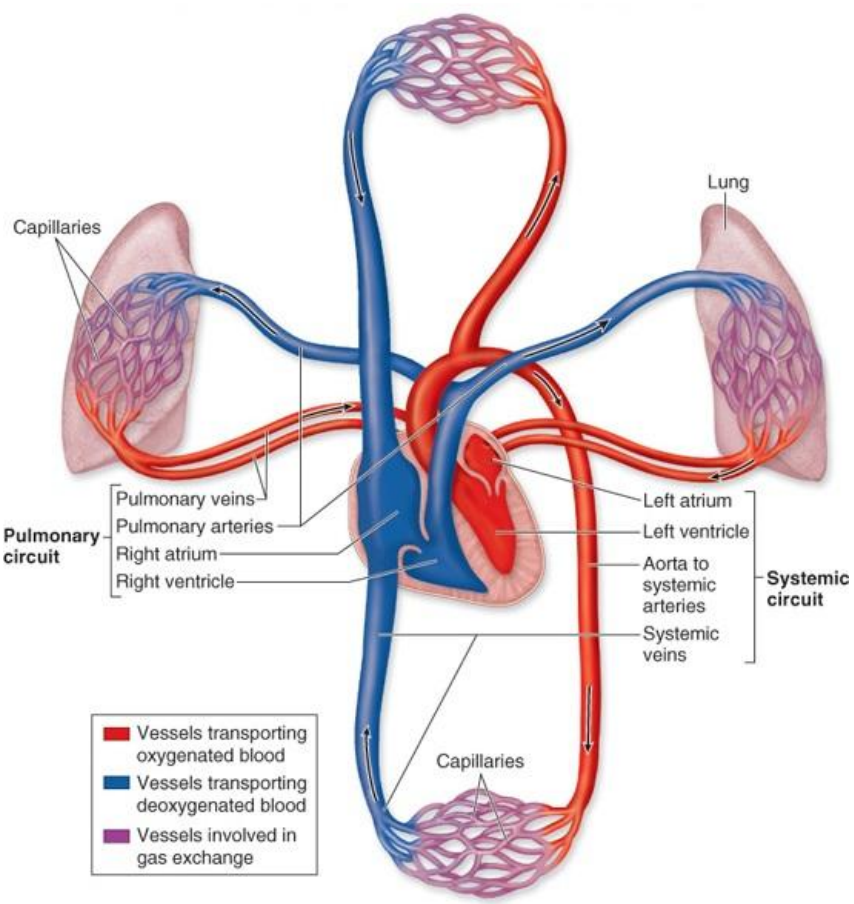

Figure 2.1 – Simplified diagram of the circulatory system with schematic view of the blood pathway. Oxygenated blood is shown in red; deoxygenated blood in blue; blood flow is indicated with arrow (image courtesy of The McGraw-Hill Companies, Inc.).

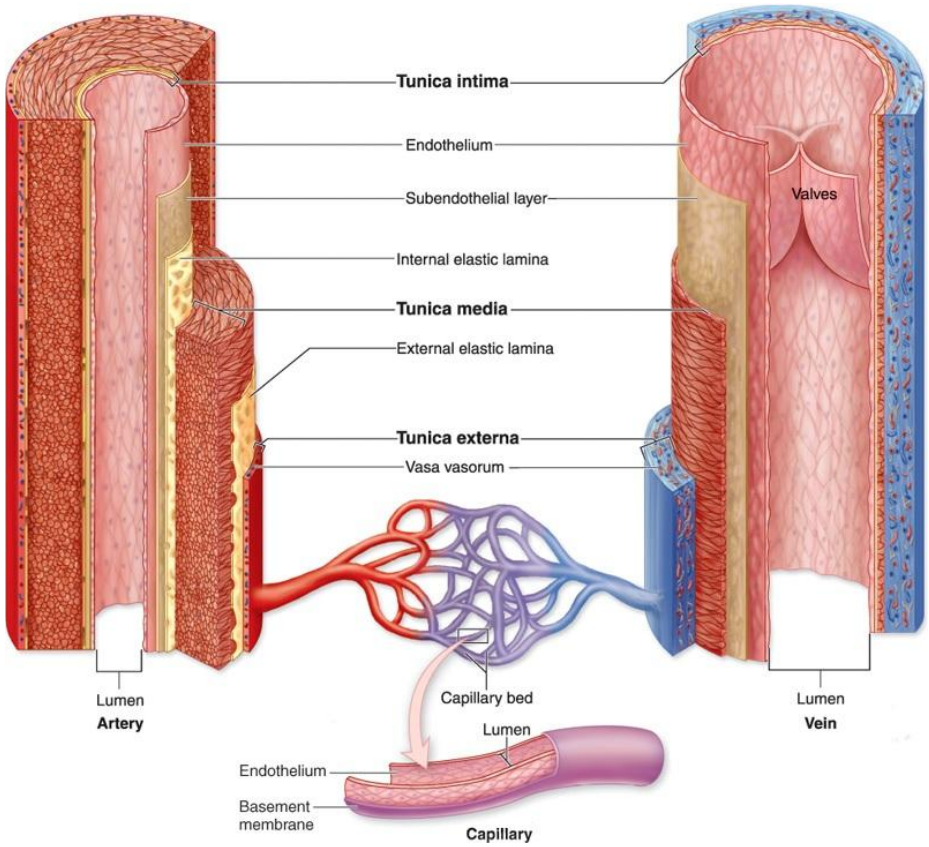

Figure 2.2 – Structure of the vascular tree with relative vessel wall thickness. The small diameters of the capillaries provide a relative large surface area for the exchange of gases and nutrients (image courtesy of The McGraw-Hill Companies, Inc.).

The arteries are the thick walled vessels (see Figure 2.2) that withstand the highest pressures and largest pressure oscillations in the vascular tree. Arteries branch into arterioles and then into capillaries, thus reducing blood pressure, pressure oscillation and velocity due to an increase in corresponding cross-sectional area in the capillaries (see Figure 2.3). Then blood leaving the capillaries converges into venules which are drained by veins. The latter are large, thin walled vessels where blood travels with the aid of gravitational pressure. Another effect exists, named anastomosis, in which arterial blood is shunted directly to the venous system without traversing capillaries. PPG measures the blood volume changes in the microvascular bed; therefore the pulsatile nature of arterial blood flow is inherently important to the technology.

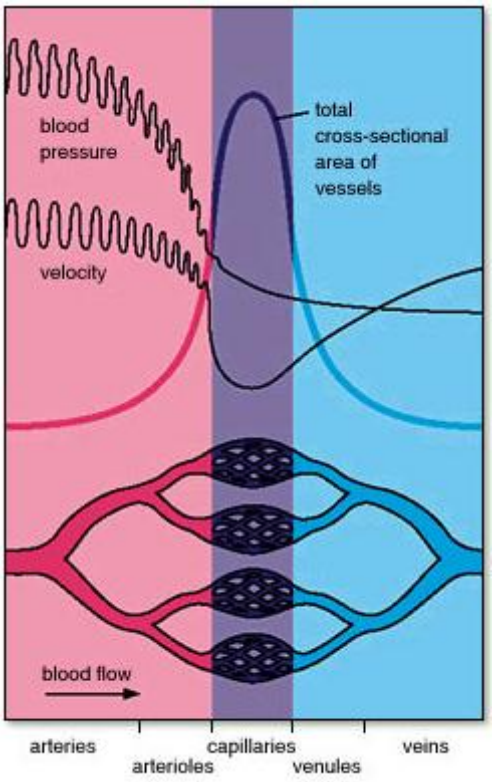

Figure 2.3 – Comparative cross-sectional analysis of scales in the cardiovascular tree (image courtesy of The McGraw-Hill Companies, Inc.).

An exchange of oxygen, nutrients and waste products and carbon dioxide takes place between the blood and adjacent tissues as the blood traverses the capillaries, where its reduced pressure/speed and increased cross-sectional area allows this to occur effectively. All cells in the body require this exchange; therefore, all tissue in the human body is literally perfused with blood. Out of all the organs of the body that are fed by the cardiovascular system, skin has a high relevance in non-invasive techniques as its surface is the site onto which sensing probes are placed. Consequently, its anatomical and physiological characteristics always play a role in these technologies. Typically, PPG is used to take measurements from the skin surface.

Human skin could be essentially divided into three layers, namely epidermis, dermis and fat layers. Further specification could be conducted in the dermis layer, which thereby provides a five-layer model (Figure 2.4). The epidermis is the outermost layer, in which the skin pigment melanin is produced by cells called melanocytes. This pigment is responsible for the protection of the skin against harmful radiation by means of absorption. The dermis layer consists of three distinct layers that can contain different concentrations of blood. The first layer of the dermis

accounts for the superficial blood plexus and the capillary loops located in the upper dermis, and the third layer of the dermis accounts for the deep blood plexus in the lower dermis [6, 7].

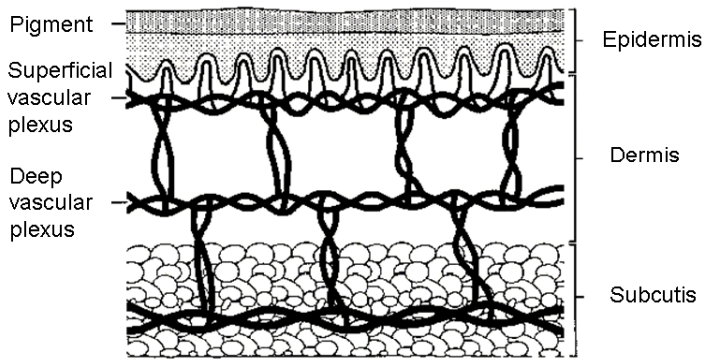

Figure 2.4 – The representative diagram of the skin with basic anatomy structures [8].

2.2.2 Optical Principles

As an optical bio-monitoring technique, PPG requires a light source and detector to function and relies on the optical properties of biological tissue at a selected area. The human tissue bed is composed of tissue, bone, blood vessels, fluids, skin and blood. Each of these components has their unique optical properties. Hence, the interaction of light with these biological tissues is complex and includes the processes of (multiple) scattering, absorption, reflection, transmission and fluorescence [9].

2.2.2.1 The Beer-Lambert Law

The common physical assumption implicit in PPG is that changes in measurement light intensity are mostly due to changes in blood volume. The fairly uniform distribution of blood within the peripheral vasculature leads us to suppose that we may model those blood volume changes by corresponding changes in the homogenous and macroscopic optical properties of the tissue. In early PPG studies, the Beer-Lambert law was adopted to provide a simple model that aids physiological understanding. Beer-Lambert law relates light transmitted through a homogeneous medium of a known optical path length and absorbance to the concentration of the medium. Specifically, if monochromatic incident light of intensity I_0 enters the medium, a part of the light is transmitted through the medium while another part is absorbed. The intensity I of light travelling through the medium decreases exponentially with the distance:

$$I = I_0 e^{-\mu(\lambda)cd} \qquad [\mathbf{2.1}]$$

where $\mu(\lambda)$ is the extinction coefficient or absorptive of the absorbing substance at a specific wavelength, c the concentration of the absorbing substance which is constant in the medium, and d the optical path length through the medium.

2.2.2.2 Wavelength Choices

Several research groups have investigated the complex optical processes in relation to PPG technique and highlighted the key factors that might affect the amount of light received by the photodetector: the blood volume, blood vessel wall movement and orientation of red blood cells (for a review, see [4]). Among these factors, the blood volume change is the most important one which limits practical wavelengths of a PPG light source.

a) The optical water window

Modern PPG sensors often utilize low cost semiconductor technology with LED/RCLED and matched photodetector devices working at the red and/or infrared wavelengths. Ideally for PPG, human blood would absorb greatly and all other tissue would absorb weakly as this would allow for accurate monitoring of blood volume changes with low light source intensity. Human tissue is mainly composed of water that absorbs light very strongly in the ultraviolet and the longer infrared wavelengths. The shorter wavelengths of light are greatly absorbed by melanin (Figure 2.5). Hence, a window in the absorption spectra, e.g., 600-1300 nm, which allows visible and near infrared light to pass more easily is often employed in PPG to facilitate the measurement of blood flow or volume change.

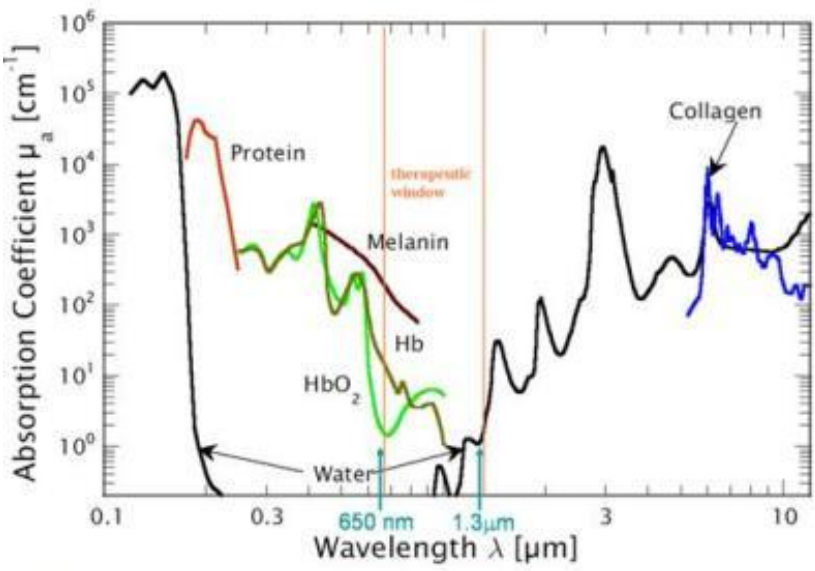

Figure 2.5 – An optimal optical window exists between 600 and 1300 nm, owing mainly to lack of strong absorption by water and melanin (image courtesy of www.chem.duke.edu/~wwarren/).

b) Tissue penetration depth

In order to monitor the blood volume change in the microvascular bed which typically has the depth around 400 to 4000 μm, the wavelength-dependent penetration depth of the light source is another factor that limits the practical wavelength of the PPG light source. For instance, red light penetrates into living skin at about 0.5 to 1.5 mm while for blue light this depth may be reduced by as much as a factor of four due to increased scattering and absorption in the dermis. Table 2.1 lists the approximate penetration depths which the radiation is attenuated to 1/e of the incident energy density, for fair Caucasian skin.

Table 2.1 – Approximate depth for penetration of optical radiation in Caucasian skin to a value of 1/e (37%) of the incident energy density [10].

Wavelength (nm)	Depth (μm)
250	2
280	1.5
300	6
350	60
400	90
450	150
500	230
600	550
700	750
800	1200
1000	1600
1200	2200

c) Isobestic wavelength

Absorption in the vascular dermis is dominated by the blood-borne pigments such as the haemoglobin (Hb) contained in the red blood cells. Haemoglobin combines with oxygen in the lung to form oxyhemoglobin (HbO_2) which is the carrier of oxygen through the body. The concentrations variation of Hb and HbO_2, indicating the metabolism of the tissue, thereby provide clinically useful physiological information. This is the fundamental principle of pulse oximetry, another widespread application of PPG technique. The technique oximetry itself is made possible by the significant differences that exist in absorption between HbO_2 and Hb except at the isobestic wavelength (Figure 2.6). The ratio of absorption due to arterial blood at two wavelengths carefully selected from either side of the isobestic point can thus be linked to a corresponding level of blood oxygen saturation. Conventionally selected wavelengths are in the 660 and 900 nm bands [11].

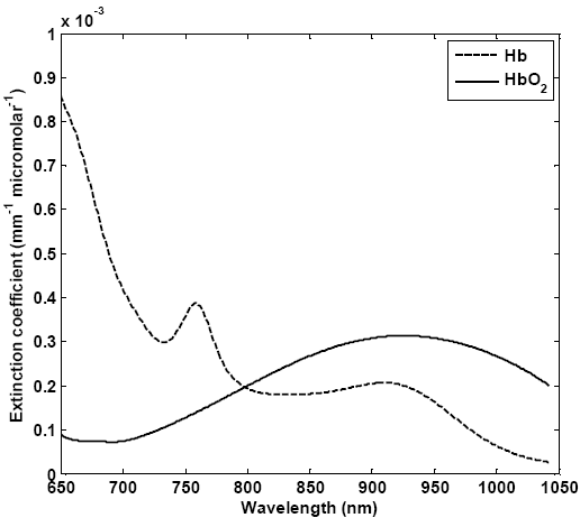

Figure 2.6 – Absorption spectra of Hb and HbO_2. The isobestic point within red and infrared range (around 805 nm) is the wavelength where the absorption by the two forms of the molecule is the same (data courtesy of http://www.ucl.ac.uk/medphys/).

2.2.3 Two Modes of PPG Operation

Based upon the relative positions of the light source and the photodetector, two modes of PPG measurements are generally employed, namely the reflection and transmission mode, shown in Figure 2.7 (a) and (b) respectively.

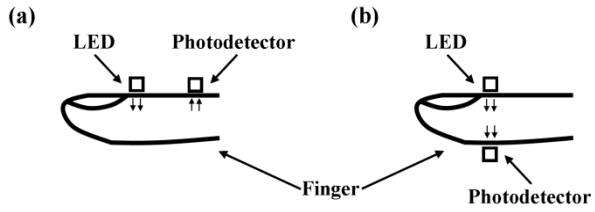

Figure 2.7 – Schematic of the two PPG operation modes: (a) reflection mode and (b) transmission mode.

a) Reflection mode

In a reflection PPG assessment system, the light source and the photodetector are positioned adjacently in close proximity to the skin surface (Figure 2.7 (a)). The intensity of the back scattered light from the skin shows the information of the blood volume changes together with the structure and pigmentation of the skin. Specifically, due to intravascular increases of red blood cells and Hb in the systole period, a pulse of blood increases the optical density and the path length which thereby decreases the light intensity detected by the photodetector. An opaque shield is usually positioned between the optoelectronics to prevent any direct illumination from the light source to the photodetector without first passing through the tissue. This configuration enables measurements virtually from any point of the skin surface which is hard to access using transmission mode, and has gained much attention since 1949 [12]. For an accurate measurement, the sensor should be attached firmly to the skin, thus the measurement site normally requires a flat skin surface, e.g., chest, forehead, temple, forearms and limbs.

b) Transmission mode

Normally, in a transmission mode PPG assessment system, tissue is irradiated by the light source, and the light intensity measured by the photodetector on the other side of the tissue is influenced by the tissue optics variations (Figure 2.7 (b)). In transmission mode, since the photodetector has to detect the light transmitted through the tissue, the photodetector should be placed as close as possible to the skin without exerting force on the tissue. If the force exerted by the probe is significant, the blood under the tissue, where the probe is placed, may influence the obtained waveform due to the pressure applied. However, if the distance between the LED and the photodetector increases, the optical path length increases consequently and the amount of detected light decreases. Hence, due to these factors, the transmission mode PPG measurement system is typically employed on the subject's finger, toe, ear or nose.

2.2.4 PPG Waveform

As mentioned above, a heart cycle covers two heart beats. Specifically, during systole, the heart pumps blood both to the body and to the lungs, the amount of blood increases resulting in more light absorption. While during diastole, both ventricles fill with blood, the amount of blood decreases in arteries resulting in less light absorption. Thus, the measured PPG waveform, comprises a pulsatile ('AC') physiological waveform, attributing to cardiac synchronous changes in the blood volume with each heart beat, which is superimposed on a slowly varying quasi-static ('DC') baseline with various lower frequency components attributed to respiration, sympathetic nervous system activity and thermoregulation [4]. A representative schematic of the pulsatile photoelectric output is demonstrated in Figure 2.8.

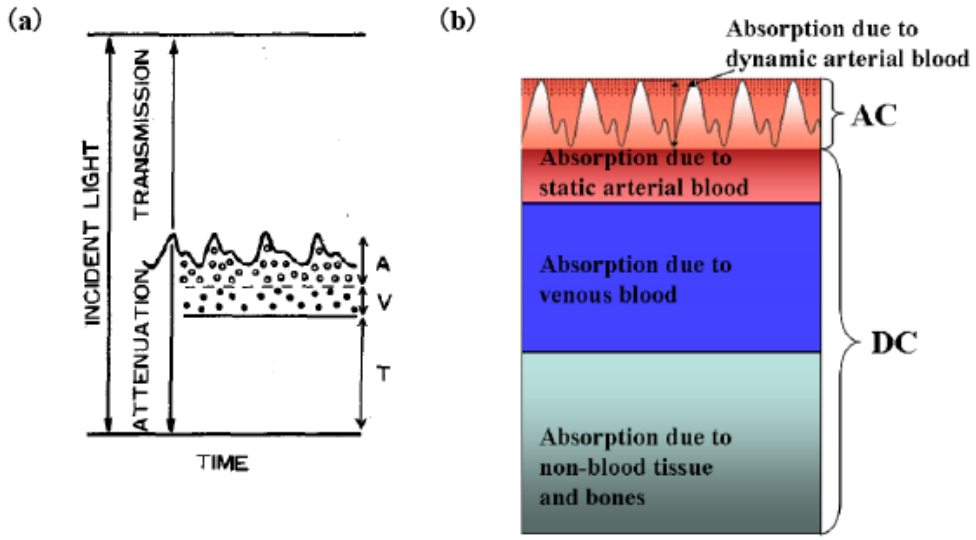

Figure 2.8 – Schematic of the pulsatile photoelectric output. (a) A transmission mode: the attenuation of the incident light is caused by A–arterial blood, V–venous blood, T–tissue [13]. (b) The relative absorption of blood and tissue, specifically the differentiation of absorption due to dynamic arterial blood and to the static/quasi-static arterial blood.

Observation of measured intensity indicates that the AC components accounts for only a very small proportion of the total intensity. This indication results from the fact that a skin vascular bed contains only a small amount of blood about 2-5% [14], which itself experiences only a volumetric change of a few percent (typically 5%) with the cardiovascular pulse wave [15]. In spite of the small amount of the measured intensity, AC components have shown its usefulness in assessing the arterial compliance, vascular disease and cardiac performance. In this thesis,

without further specification, only the AC components, referred as PPG signals, are analyzed and discussed.

2.2.5 Applications of PPG

Since its conception, PPG has been widely utilized in clinical community and proven its ability not only in real time monitoring physiological parameters, such as blood oxygen saturation (SaO_2), heart rate (HR), blood pressure (BP), respiration, and cardiac output (CO), but also in vascular assessment (arterial disease, arterial stiffness and aging, endothelial function, and vasospastic conditions) and autonomic function assessment (heart rate variability, thermoregulation, blood pressure, orthostatic intolerance) [4].

a) Physiological parameters

Blood oxygen saturation (SaO_2): The human body cannot survive for more than a few minutes without oxygen intake, as opposed to the days or weeks that it can survive without water or food intake. The capacity to provide real-time knowledge of arterial oxygen saturation makes pulse oximetry effective at giving an early warning for hypoxia [16], which is the most common cause of morbidity and mortality during and after anaesthesia. Hence, in the early 1990s, pulse oximetry became a mandated international standard for monitoring during anaesthesia [4]. SaO_2 can be determined through shining red and then near infrared light in vascular tissue with rapid switching between both wavelengths. Because of the light absorption differences of HbO_2 and Hb at these two wavelengths (see Figure 2.6), SaO_2 could be estimated from the amplitude ratio of AC signals, and corresponding DC components. Conventionally selected wavelengths are in the 660 and 900 nm bands [11].

Heart rate (HR): The heart rate, referred as the number of heartbeats per unit of time, typically expressed as beats per minute (bpm), is an important physiological parameter to measure for a wide range of clinical settings, i.e., hospital-based and ambulatory patient monitoring. The AC component of the PPG signal is synchronous with the heart beat which provides a route for accessing the HR information. The HR information is always obtained and displayed alongside the SaO_2 measurement system. The practicability of PPG technique in HR monitoring has been validated with electrocardiograph (ECG), the gold standard for HR measurement, and shown approximately ±1% false beats [17]. Given the condition that an adult patient with a heart rate over 100 bpm is considered to be tachycardic in the Emergency Severity Index triage [18], the difference of PPG and ECG is only 1 bpm. Fourier Transform (FT) which offers a passage from

the time domain to the frequency domain is often applied in conventional PPG signal processing for HR and respiration rate estimation. However, FT assumes that signals are steady-state when physiological signals are transient in nature. Most recently, more sophisticated algorithms have been adopted to extract heart rate information from PPG waveforms, including time-frequency techniques based upon the smoothed Wigner Ville distribution [19]. The time-frequency approaches convert a one-dimensional time signal into a two dimensional function of time and frequency so that frequency components can be localized with good temporal resolution [20], the missing information in conventional FT technique.

Respiration: Physiological monitoring of respiratory rate is clinically important in many applications, i.e., neonatal care, sleep study, sports study assessment and anaesthetics. Respiration causes a slow variation in the peripheral circulation which makes it possible to monitor using a PPG sensor attached to the skin. Though the physiological mechanisms behind the low frequency respiratory induced intensity variations is not fully understood, it is believed to include contributions from the venous return to the heart caused by alterations in intra-thoracic pressure and also changes in the sympathetic tone control of cutaneous blood vessels [4]. The respiration information embedded in the quasi-static DC component could be extracted through a digital bandpass filter.

Blood pressure (BP): Arterial blood pressure is another important clinical parameter. The effort of employing PPG technique in the BP monitoring started from the early 1980s [21]. Since then, a substantial number of comparative and methodological studies have been reported on the technology (for a review, see [22]). Technically, the method is based upon the dynamic (pulsatile) vascular unloading of the finger arterial walls using an inflatable finger cuff with built-in PPG sensor. Besides, a pulse transit time based algorithm has also been introduced and validated with conventional arm blood pressure measurements [23]. The comparable results indicate the practicability and usefulness of PPG technique for home monitoring of blood pressure.

b) Vascular assessment

Arterial disease: Among the non-invasive biomedical diagnostic techniques in assessing peripheral arterial disease, PPG occupies a unique position. Much of vascular physiology and pathophysiology has been established based upon PPG studies. Disease detection with PPG is possible because the peripheral pulse usually becomes damped, delayed and diminished with increasing severity of vascular disease, such as lower limb arterial disease, carotid artery

disease, and thromboangiitis obliterans. For example, Allen and colleagues reported a damped, relatively delayed and reduced PPG waveform from the affected side of limb arterial disease patients [24]; Cooke *et. al.*, characterized the PPG pulse shape in healthy subjects and Raynaud's patients and found that both the pulse amplitude and the slope changes of the rising edge were trait-like marker for the condition [25]. Most recently, multi-body site PPG measurements have been proposed for peripheral vascular disease which could be employed for reliably locating disease within an arterial segment and assessing responses to vascular therapy.

Arterial stiffness and aging: The assessment of arterial stiffness is clinically important due to its strong collection with the cardiovascular morbidity and mortality. The process of hardening (stiffening) of the arteries has been shown to start from around the first or second decades of life in healthy subjects, and the process could be accelerated by medical conditions including renal disease and diabetes mellitus [26]. Objective assessment of vascular aging could also provide valuable information about hypertension, a risk factor for stroke and heart disease. However, direct assessment of the arterial stiffness is complicate which stimulates the investigation of surrogate indirect non-invasive measurements for arterial stiffness evaluation. Basically, the stiffer the artery the faster the pulse will travel through it to the periphery. Hence, the measurements of pulse wave velocity (PWV) and pulse transit time (PTT) seem to be applicable and reliable for non-invasive arterial stiffness assessment. Generally, the PTT – the time it takes a pulse wave to travel between two arterial sites – is inversely related to the PWV [27]. A cumulated number of studies have been published on the PPG based arterial compliance assessment. Nitzan and colleagues have recently demonstrated a decreased of PTT with age which is attributed to the direct structural decrease of the arterial compliance with age [28]. This result has been further confirmed by Allen and Murray [29]. Age-related changes in the pulse shape characteristics can also yield valuable diagnostic information about the cardiovascular system, i.e., characteristic changes in crest time and 'triangulation' of the digital volume pulse were noted in patients with hypertension and arteriosclerosis [30].

c) Autonomic function

Heart rate variability (HRV) & Pulse rate variability (PRV): The last two decades have witnessed the recognition of a significant relationship between the autonomic nervous system and cardiovascular mortality, including sudden cardiac death. Experimental evidence for an association between a propensity for lethal arrhythmias and signs of either increased sympathetic or reduced vagal activity has encouraged the development of quantitative markers of autonomic activity [31]. The beat-to-beat fluctuation in heart rate, e.g., heart rate variability

(HRV), represents one of most promising such markers and has attracted considerable attention in biomedical and clinical community. The sinoatrial node as the 'pacemaker', located at the posterior wall of the right atrium, initiates each heartbeat in normal physiology. The frequency generated by the auto-rhythmicity of the sinoatrial node is relatively constant and modulated by many factors, e.g., temperature regulation, cardiac sympathetic nerve activity, respiratory rhythm and cardiac parasympathetic innervations [32]. The genesis of HRV thereby is determined by complex interactions of hemodynamic, electrophysiological, humoral variables, as well as by autonomic and central nervous regulation [31]. The clinical relevance of HRV was first appreciated in 1965 [33]. Since then, considerable studies have been published and links between HRV and several cardiological and non-cardiological diseases have been established (for a review, see [31]). The heart rate and its variability could easily be extracted from PPG pulse signals since the AC component of the PPG pulse is synchronous with the beating heart.

Thermoregulation: Thermoregulation refers to the ability of keeping body temperature within certain boundaries and maintaining the state of stability between the internal environment and external environment. Skin blood flow in humans can increase substantially in response to thermal stress, i.e., vasodilation and increased skin blood flow (in concert sweating) are essential to heat dissipation during heat exposure and exercise while vasoconstriction in the skin decreases heat loss from the body and protests against hypothermia during cold exposure [34]. These responses in the skin circulation could be accessed via PPG technique. Hahn and colleagues showed that the PPG amplitude was significantly decreased during local cold exposure tests at a moderate cooling temperature (16 ℃) [35], indicating the potential usefulness of PPG in the assessment of secondary Raynaud's phenomenon and complex regional pain syndrome.

2.2.6 Limitations of Conventional PPG

In spite of the wide application, there are several drawbacks which in some level limit the usefulness and evolution of the conventional PPG sensor: (1) *spot measurement*: the use of the transmission PPG sensor is limited to areas of the body sites, such as fingers, toes, and earlobes while the reflection mode enables measurements virtually from any point of the skin surface. However, both modes could only monitor blood volume changes at a single site/point per probe. The blood perfusion information which offers added value for appraising the cardiovascular system is lacking, (2) *contact measurement and contact force*: for accurate measurements, the sensor should be attached/clipped to the skin which is obviously not suitable in situations of

skin damage (burn/ulcer/trauma). Besides, the contact force of the sensor should also be carefully considered as the arterial geometry could be deformed by compression which consequently would influence the obtained PPG waveform, (3) *cable*: conventional contact PPG sensor often comes with a soft cable which constrains the free movements during measurement and to some extent causes inconvenience in the situation of long-term monitoring and clutter in the neonatal ICU. Therefore, it is worth to develop a non-contact remote imaging technique to overcome these drawbacks. Indeed, driven by the dramatic developments of imaging technique and achievements in imaging instrumentation, there has been a resurgence of interest in PPG in recent years.

2.3 IMAGING PHOTOPLETHYSMOGRAPHY

Remote-sensing imaging offers additional values for any parameter by appealing to human cognition and literally facilitates insights that would otherwise be difficult or even impossible to obtain. Among these imaging techniques, the recently introduced non-contact remote camera based imaging PPG, originated from the PPG technique, has provided some of the first quantitative insights into assessment of skin blood flow and related rhythmical phenomena. The investigation of the iPPG technique starts from 2000 [36] and has attracted significant attention in the last decade. The introduction of the fast digital camera also inspires the development of this methodology to allow non-contact monitoring from a large field of view with assistance of an array of (multi-wavelength) light sources. In this section, the operation principles, applicability, engineering issues, challenges and research directions are recounted.

2.3.1 Biomedical Imaging Techniques

The last decade has witnessed the enormous progress of optical imaging technologies for various biomedical and clinical applications. Among these applications, the blood perfusion assessment has proven its usefulness in appraising the cardiovascular system. Strictly speaking, both *flow* and *perfusion* imply the amount of fluid being moved per unit time rather than the velocity alone [37]. In this section, several optical blood perfusion imaging techniques, e.g., laser Doppler imaging (LDI), laser speckle contrast imaging (LASCA), and imaging photoplethysmography (iPPG), have been briefly reviewed to help the understanding of the emergence and advantages of the iPPG technique.

a) Laser Doppler Imaging (LDI)

The Doppler Effect has been known since the middle of the 19th century. It explains the change in frequency of a wave when there is relative movement between the source of the wave and the observer: $f' - f = \frac{v}{c-v} f$, where f is the original frequency of the light, f' is the shifted frequency, v is the relative velocity of the source and the observer and c is the velocity of the wave. Laser Doppler velocimetry has been developed and used to measure blood flow velocity for several decades, making it an established tool for monitoring tissue blood flow at a single point. Moreover, via scanning the area of interest, a map of velocity distribution could be obtained which provides important diagnostic information in many medical and surgical situations, e.g., inflammation, healing process, burn assessment, dermatology and physiology (for a review, see [37, 38]). However, the emphasis of the researchers in this field in recent years has been on the theory of the technique, especially the effect of multiple scattering and the use of statistical methods. This, and an increasing sophistication in the experimental techniques has led to laser Doppler imaging being a relatively expensive method to implement (for a review, see [37]). The same is generally true of photon correlation techniques.

b) Laser Speckle Contrast Imaging (LASCA)

Laser speckle is a random interference effect that gives a grainy appearance to objects illuminated by laser light. If the object consists of individual moving scatterers, e.g., blood cells, the speckle pattern fluctuates. These fluctuations provide information about the velocity distribution of the scatterers. A technique developed in the early 1980s [39] simultaneously achieves velocity assessments (without scanning) and very simple data gathering and processing – laser speckle contrast (LASCA) imaging which was originally developed for the measurement of the retinal blood flow. Briefly, a spatial statistics of time-integrated speckle approach was employed to reveal the velocity information. For instance, a short exposure time would freeze the speckle and result in a high-contrast speckle pattern, whereas a long exposure time would allow the speckle to average out, leading to a low contrast. Hence, the velocity distribution in the region of interest is mapped as variations in speckle contrast. The principle of LASCA has been successfully demonstrated in the laboratory and many of the problems solved [40, 41]. With the help of the LASCA, Dunn and colleagues have achieved the monitoring of the cerebral blood flow in rats [42]. Nevertheless, a number of key questions still remain, chief among them include multiple scattering, the difficulty of accurately modelling the complex velocity distributions in the capillaries, and the effect of light scattered from stationary tissue (for a review, see [37]). Much work is going on into these effects and the question is far from

settled [43-45].

c) Imaging Photoplethysmography (iPPG)

Among the blood perfusion assessment techniques, imaging photoplethysmography (iPPG), as originated from the PPG technique, has proven to be superior in its ease of use, low-cost, absolutely safe, convenience, and multiple physiological assessments. Compared to the LDI and LASCA, iPPG has a relative shorter history. With the recent evolution of these optical blood perfusion imaging technologies, it is soon realized that PPG could be extended to imaging as well, i.e., Schultz-Ehrenburg and colleagues have demonstrated an experimental cooled near infrared CCD PPG imaging system for studying skin blood flow and related rhythmical phenomena [46]. The basic concept of iPPG is to illuminate the specific tissue with an array of light sources and to measure the light leaving the tissue with multiple detectors. The introduction of the fast digital camera inspires the development of this concept to allow non-contact monitoring from a large field of view. The main difference between iPPG and the aforementioned blood perfusion assessment techniques is that iPPG is able to detect the blood volume change of tissue rather than blood velocity, thereby facilitating the assessments of multiple physiological parameters, e.g., heart rate, respiration rate, blood pressure, heart rate variability and pulse transit time and making it an attractive area of research in the biomedical and clinical community.

2.3.2 Principles of Operation

Imaging PPG is a technique that enables remote physiological sensing and reduces the physical restrictions and cabling associated with patient monitoring. Indeed, iPPG has many similarities with conventional PPG since both of them operate on similar physiological systems and optical principles. For instance, iPPG also requires a light source and a photodetector to function. However, the capability and the functionality of the light source and photodetector are different in iPPG setup. A schematic diagram of an iPPG system is presented in Figure 2.9.

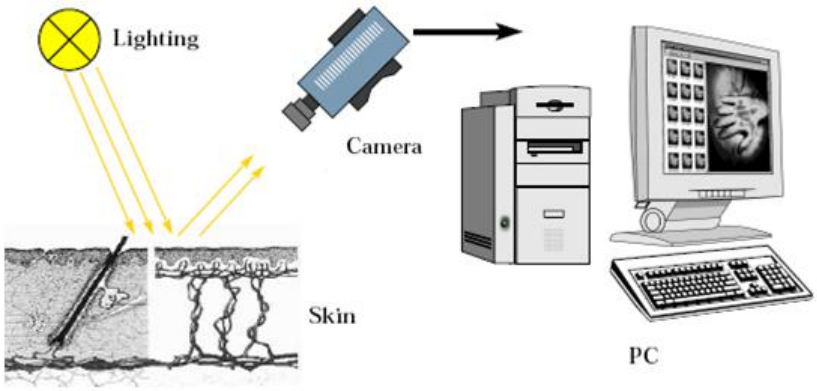

Figure 2.9 – A schematic setup of an iPPG system which includes a light source and a camera (image courtesy of [46]). Physiological information could then be extracted from the obtained images.

a) Light source

Differing from the simplicity of conventional PPG, the light source design, particularly the wavelength and structure, should be carefully handled in an iPPG setup. *Wavelength*: as mentioned above, the practical wavelength suitable for iPPG is also limited in the red/near-infrared spectral range, typically from 600 to 1000 nm, allowing high contrast in the absorption of blood compared to other components of tissue, i.e., the absorption of hemoglobin is about 10 times higher than that of bloodless tissue. The near-infrared light will enter the skin relatively unrestrained and penetrate deeper into the skin whereas extinction of green light will be much higher, which leads to reduced penetration depth. Thus by choosing different wavelengths for illumination different depths of skin for investigation can be targeted. The green light also features clear plethysmographic signals in several recently introduced iPPG systems [47, 48]. *Structure*: differing from contact PPG which normally utilizes single LEDs/RCLEDs per channel as the light source, the light intensity should be large and relatively uniform in iPPG system to allow the blood perfusion measurement of multi-layered tissue from a large area. Several LED/RCLED arrangements have been introduced and have shown their advantage in different application areas. Specifically, a dual wavelength array of LED light sources has been adopted for pulse oximetry measurements [49], while in our previous study, a ringlight has been introduced and proven its usefulness in heart rate monitoring [50].

b) Camera

In contrast to the contact PPG which uses photodiodes to measure the light intensity; a fast digital camera is normally employed in the iPPG system. As the key component of an iPPG system, the camera collects the scattered photons coming from the illuminated tissue. The

detected blood volume change, i.e., the photoplethysmographic signal (AC), is very small compared to the non-pulsatile signal. Hence, the camera should have a high sensitivity over the chosen light source spectral range and the flexibility of choosing variable readout speed and exposure time due to different applications. Typically, the charge-coupled device (CCD) and complimentary metal-oxide semiconductor (CMOS) cameras as optic sensors have been widely applied in iPPG studies. A CCD sensor moves photo-generated charge from pixel to pixel and converts it to voltage at an output node, while a CMOS sensor converts charge to voltage inside each pixel [51]. Hence, CCD cameras could create a high-quality and low noise image; CMOS cameras have a higher frame rate and comparable imaging performance whilst consuming less power. With the latest advances in opto-electronics, an upgraded CMOS camera could achieve a higher frame rate with a high sensitivity. In this thesis, a monochrome CMOS camera is employed for the remote physiological measurements.

2.3.3 Imaging PPG Signal Acquisition

Compared to the conventional PPG system which straightforwardly presents the plethysmographic waveforms, the signals captured by the iPPG is embedded in a sequence of raw image frames. Hence, to obtain the PPG signals, several pre-processing approaches have been carefully considered. The pixel value sequence with the tissue area contains the raw PPG signals together with different noise signals, including electric noise and motion artefact noise. One approach has been adopted in the iPPG publications up to date and shown its ability in improving the signal to noise ratio (SNR) significantly [48] under the presence of minor motion artefacts. Specifically, once a set of recordings is successfully acquired, the raw image frames are divided into discrete sub-windows to produce a new set of reduced frames, where the value of each pixel in the reduced frame is set as the average of all the pixel values within each sub-window. Subsequent processing is performed on the reduced frames. The disadvantage of such approach is the reduced spatial resolution and only suitable for minor motion artefacts conditions. A schematic diagram of the iPPG signal acquisition is presented in Figure 2.10.

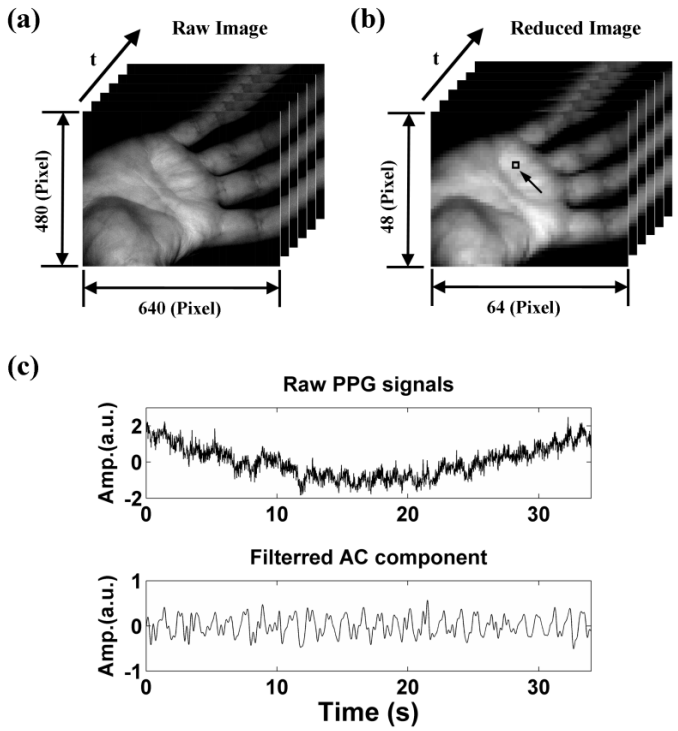

Figure 2.10 – A schematic diagram of the iPPG signal acquisition approach. (a) The raw image frame sequence (palm). (b) The reduced image frame sequence via a 10×10 pixel sub-window. (c) The raw average iPPG signals and the band-passed (5^{th} order Butterworth bandpass filter with a cut-off frequencies set at [0.5, 5] Hz) filtered AC components. The position where the iPPG signal was selected is highlighted with a box and an arrow.

2.3.4 Research in iPPG

As detailed before, compared to the conventional contact PPG and other perfusion imaging technologies, i.e., laser speckle contrast analysis (LASCA), iPPG shows its unique advantage of non-invasive, non-radiative and remote monitoring of blood volume changes from a large area. Such combined features explain the widespread attraction in the biomedical and clinical community. As a substitute of conventional PPG, iPPG could be employed to assess almost all of the physiological measurements that the contact PPG can currently provide. In this section, some typical applications of iPPG are enumerated from the selected studies; several applicable potential research areas are also demonstrated.

a) Blood oxygen saturation (SaO_2)

The same principles utilized in the contact pulse oximetry sensor, i.e., the Hb and HbO_2 have different absorption coefficients in the red and infrared range, could be employed for remote

SaO_2 measurements via iPPG system. However, the involvement of a multiple wavelength light source needs an additional illumination control circuit to alternately energize each wavelength. The investigation of 'SaO2 camera' technology can be said to start in 2005, Wieringa and colleagues first introduced a contactless photoplethysmographic imaging technique and obtained heartbeat-related photoplethysmograms at multiple wavelengths (λ_1=660nm, λ_2=810nm, and λ_3=940nm) [52]. This study thereby presents a practical iPPG system and sets a basic model of remote blood oxygen saturation measurement for the following research. Since then, several studies have been published to make a further step toward noncontact pulse oximetry [49]. The experimental setup in Wieringa's study [52] is schematically presented in Figure 2.11.

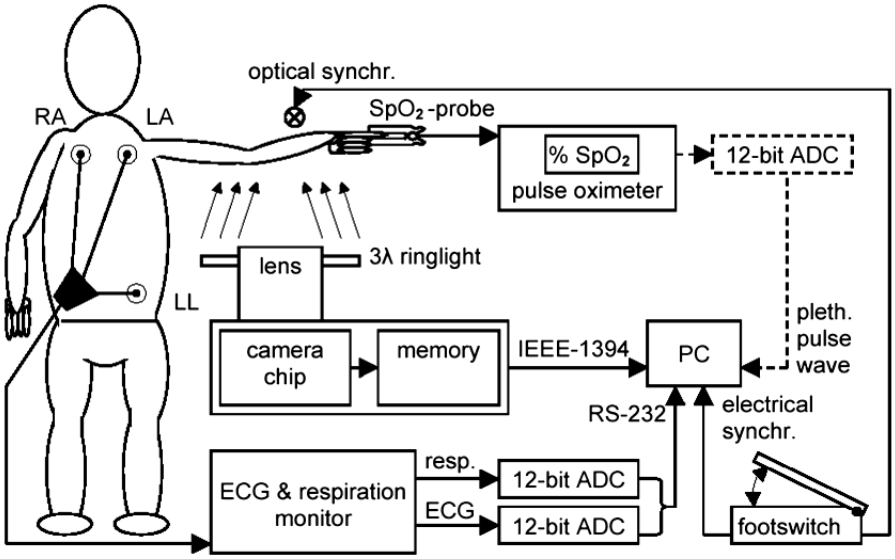

Figure 2.11 – Experimental setup for the blood oxygen saturation measurement [52]. Movies at three wavelengths (3λ) were acquired via a monochrome CMOS camera in order to extract imaging photoplethysmography signals. Simultaneously reference ECG, respiration and contact PPG signals were recorded for further verification. Synchronization between the reference signals and images was achieved via a footswitch.

b) Heart rate (HR)

The heart rate is an important physiological parameter to measure for a wide range of clinical settings, i.e., hospital-based and ambulatory patient monitoring. Several studies have been presented different remote heart rate estimation technologies which lead to a new avenue for non-contact sensing of vital signs and remote physiological assessment, with clear applications in triage and sports training. A low cost consumer level digital camera based iPPG system using

ambient light has been reported and evaluated by Verkruysse and colleagues [48]: not only the heart and respiration rates could be obtained, the iPPG system also proves its usefulness in the characterization of vascular skin lesions (port wine stains). Besides, Ming-Zher Poh and colleagues have presented a webcam based iPPG system (Figure 2.12). Compared to a standard blood volume pulse sensor, the cardiac pulse extracted from videos achieved high accuracy and correlation even in the presence of movement artefacts [47]. This study thereby leads to new insights into medical technology trends such as telemedicine. Recently, an iPPG system has been proposed in our previous study to provide reliable assessment of the cardiovascular system during/after exercise [50].

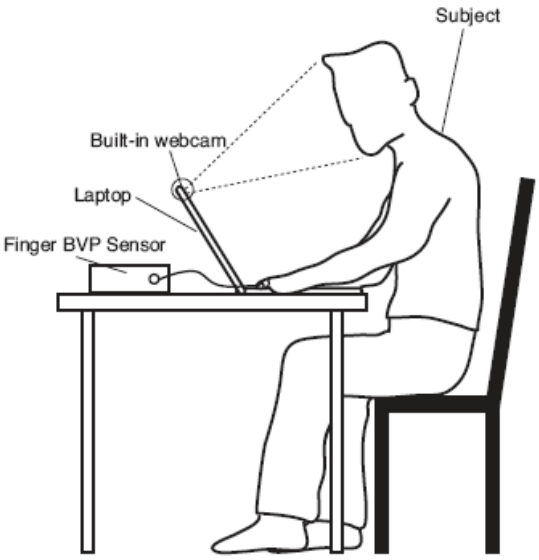

Figure 2.12 – A webcam based iPPG system for the cardiac pulse measurement [47].

c) Pulse rate variability

ECG is the recording of electrical activity generated by the heart taken from the body surface. Accordingly, HRV signals can be obtained from continuous ECG recordings, in which the heart rates at any point in time or the intervals between successive normal complexes can be determined. Despite its wide applicability, the measurement of typical multiple-lead ECG requires several adhesive electrodes to be carefully placed on the body by a trained operator. The clinical users must either confirm that the leads are correctly placed or optimise their positions before the recording. Such procedures could preclude frequent assessments of HRV in general populations. The AC component of the PPG pulse rate can be estimated from the time between systolic peaks of a PPG pulse wave, enabling the simple acquisition of pulse rate variability (PRV). One recent effort has been made to remotely assess PRV via a webcam [53].

This feasibility study has demonstrated a relatively strong correlation between the physiological parameters obtained from the webcam recordings and standard reference sensors. However a number of key questions still remain, chief among them is the sample rate of the webcam configured in the study (only 15 fps), which is much lower than the recommended sample frequency for HRV analysis (in any case >100 fps) [31]. Though the sample frequency increases to 256 Hz via interpolation technique in post signal processing, such results are not definitive and a qualified non-contact PRV technique is still missing.

d) Burn and ulcer assessment

Burns and ulcers to extremities limit the sites available for contact measurement of blood volume change due to the added risk of infection and damage from such contact. However, the assessment of the healing process within burns or ulcers could provide useful information for therapeutic evaluation. For instance, high perfusion corresponds to superficial dermal burns and only requires clinical dressing and conservative management, while low perfusion areas might require surgical treatment [54]. iPPG is configured to be a contactless technique to image the blood perfusion of tissue which make it possible for the assessment of burns and ulcers. Huelsbusch and colleagues have introduced a near-infrared CCD camera based iPPG system which provides some new insights into the functional sequences of physiological tissue perfusion and the perfusion status in ulcer formation and wound healing.

e) Remote pulse transit time (PTT)

As mentioned above, pulse transit time is clinically important due to its ability to non-invasively assess arterial stiffness, a parameter related to the cardiovascular morbidity and mortality. The time difference between the R-wave of the electrocardiography (ECG) and the onset time of the corresponding PPG pulse obtained at the fingers/toes is employed in PTT estimation, all requiring the sensors to be positioned on the tissue. More importantly, these spot measurements could only provide relatively little information about the PTT/PWV propagation. As time domain estimation, PTT analysis always requires relatively fast sample frequency which offers accurate time-domain resolution (<5 ms). The development of digital imaging techniques and achievements of imaging instruments in the past decade make it possible to capture the image at a fast speed, i.e., 500 fps in this study, which offers a nascent opportunity in remote PTT measurement.

2.3.5 Research Direction

Although the iPPG shows great advantages as its non-invasive, non-radioactive and remote measurement, there are several issues need to be considered when the iPPG setup in employed in a physiological measurement. We believe that extensive acceptance of iPPG will happen when the technique reaches the same maturity as contact PPG.

1) *Motion artefact*: PPG is susceptible to motion-induced signal corruption, making motion artefact removal or attenuation one of the most challenging issues in iPPG signal processing. In pioneering iPPG works, motion artefacts were not addressed directly and the associated PPG setups were usually operated under conditions that required the subjects to be motionless. This drawback limits the physiological monitoring capabilities of the technique in real application environments, i.e., hospital, homecare, ambulance, and sports performance assessment. In recent years, several methods, such as blind source separation [47], least-mean-square adaptive filtering [55], independent component analysis (ICA) [56], and single channel ICA [57], have been proposed for removal of noise from biomedical signals. Specifically, one recent study has been published to introduce a novel approach to attenuate the motion artefacts from iPPG signals. The method was based upon automatic face tracking and blind source separation of multichannel signals, i.e., R, G, & B colour signals, into independent components. Such an approach combining image and signal processing techniques leads to new insights in motion artefact compensation for iPPG signals.

2) *Standard of the illumination source*: differing from the contact PPG, the illuminator of iPPG setup is not in direct contact with the skin surface. Hence, a more powerful and relatively uniform illumination source is required. An illumination surface of variable intensity with respect to surface position would result in a similar variability in the final output iPPG signals [46] which thereby would influence the final blood perfusion assessments. However, the output power should be carefully considered to avoid harmful radiation. As mentioned above, different illumination sources (ambient/red/near-infrared light) and LED/RCLED arrangement methods (array/ring) have been proposed for various applications. Besides, multiple wavelength light sources have normally been employed in remote blood oxygen saturation assessments, requiring an additional illumination control circuit to alternately energize each wavelength and synchronize with the camera. Therefore, a standard of the illumination source warrants further investigation.

3) *Data handling*: in spite of the ability and facility for the iPPG system to obtain PPG signals from a region which offers added information for appraising the cardiovascular system, it is inevitable that the larger recorded datasets occupy a larger capacity and increase the complexity of data processing. For example, in our previous study, a sequence of monochrome frames with image size of 640×480 pixels (pixel resolution = 10 bits) and a sample frequency at 100 fps may easily occupy more than 1 GB of storage space after only 15 seconds acquisition. Hence, an image segmentation technique is one potential way to handle the massive amounts of data. The experimental protocol of remote physiological assessments should also be carefully considered. For example, a PTT estimation study normally requires a fast sample frequency at a relevantly short duration while in a heart rate variability investigation, a medium sample rate with several minutes monitoring is normally required.

This chapter has provided an introduction of the fundamental concepts related to photoplethysmography (PPG), specifically its physiological background, principles of operation, applicability, engineering issues and limitations. Additionally, an emerging medical imaging technique, named imaging PPG (iPPG), that remote monitors blood perfusion in the microvascular bed of tissue has been recounted together with its common research area and potential applications.

SECTION 2 METHODOGY

3 ENGINEERING MODEL

The objective of this chapter is to establish an opto-physiological model for iPPG signal processing, particularly the various multiple physiological parameters measurements. This inevitably requires a degree of simplification brought about by a series of assumptions pertaining to the macroscopic interaction of light with human tissue. Hence, this chapter explains the optical and physiological phenomena that govern diffuse optical bio-monitoring techniques, revisits some of the relevant concepts of optics and physiology, specifically those pertaining to human tissue optics and the circulatory arterial system, and describes the model relevant to this investigation.

3.1 PRINCIPLES OF TISSUE OPTICS

Optical bio-monitoring modalities can be described in general terms as systems that modify a specific light intensity, where the transfer function of the systems is determined by a number of anatomical and physiological parameters. As illustrated in the *Introduction* chapter, the interaction of light with the biological tissues is complex, however, a finite number of optical phenomena govern the behaviour of light propagating through an optically dense medium, such as skin. These are considered at a macroscopic scale and are explained in the context of their relative contributions to the effective output intensity in trans-illuminated tissue. Figure 3.1 demonstrates these phenomena which include the processes of scattering, absorption, reflection, refraction, and transmission.

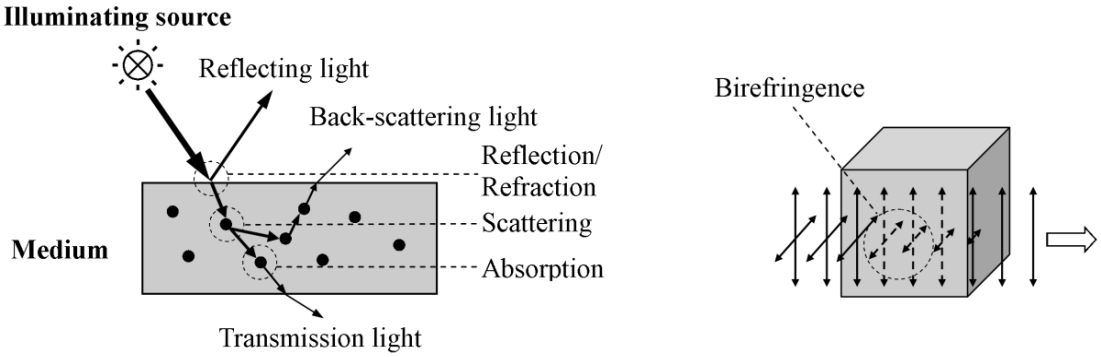

Figure 3.1 – Optical phenomena affecting studies in tissue optics.

The quantification of the optical propagation in tissue is a question of growing concern for the biomedical and clinical applications, where numerous studies have been published to propose different models related to this issue. A better understanding of these models and the related optical phenomena thereby would be of great use when creating an appropriate model for iPPG signal processing. The relevant concepts of optical phenomena, specifically those pertaining to human tissue optics are recounted in this section.

3.1.1 Refraction

Refraction occurs under any circumstance where light propagation through a medium encounters a change in its refractive index. One such occurrence is the surface effects due to index mismatched macroscopic boundaries between skin layers. A schematic diagram of this phenomenon is presented in Figure 3.2.

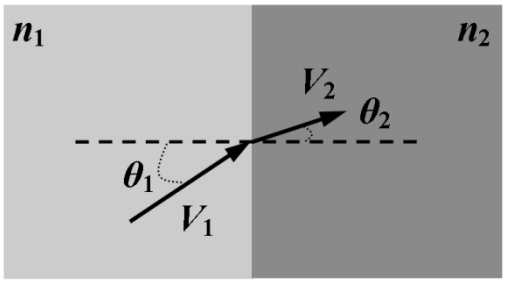

Figure 3.2 – Refraction of light between two media with different refractive index (n_1, n_2), where θ_1 is the incident angle and θ_2 is the refracted angle, V_1 and V_2 are the speeds of light in each media which follows the Snell's law: $\sin\theta_1/\sin\theta_2 = V_1/V_2 = n_2/n_1$.

The refractive indices of most soft tissues types at a macroscopic scale are in the range of 1.38-1.41, with the exception of adipose tissue which has a refractive index of approximately 1.46. The index-of-refraction disparities at the layer interfaces have been reported to be negligible in a simulation study of a multilayer model of photon diffusion in skin by Schmitt and colleagues [58]. These results have been further confirmed by Churmakov and colleagues, who concluded that the spatial photon sensitivity profile which shows the photon density distribution under normal conditions was nearly identical to that achieved when disregarding total internal reflection at the boundary between a highly scattering and absorbing medium and vacuum [59]. Consequently, the refraction phenomenon is disregarded in most photon transport models [60].

3.1.2 Scattering

Refractive index mismatches within tissue also exist at a microscopic scale, where collagen fibres, blood vessels, cell membranes and organelles etc., submit light to refractive effects. This microscopic refraction is called scattering, the effectiveness of which in practice is described with the scattering coefficient (μ_s) and the anisotropy factor g. Here, μ_s (mm^{-1}) is the mean path length between scattering events and g is the mean cosine angle of deflection upon scattering. Numerous studies employing simplified optical models for skin have yielded reliable results employing isotropic scattering. The diffusion of light through a medium has a direct effect on its irradiance distribution, thus making scattering a dominant effect in such studies.

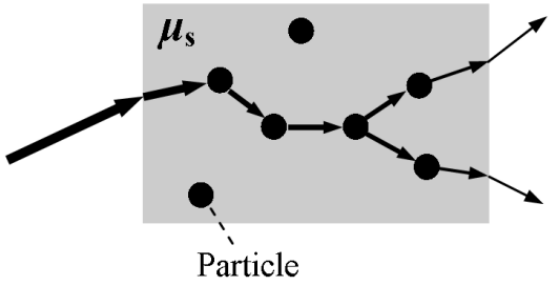

Figure 3.3 – A schematic diagram of scattering of light through a scattering medium with scattering index of μ_s.

Indeed, the scattering effect is determined by the microscopic structure of the tissue, which extends from membranes to membranes aggregates to collagen fibres to nuclei to cells. Basically, light is most strongly scattered by those biological structures whose size matches the wavelength of the incident light. However, in the common employed near-infrared region, the structures of skin that contribute the most to scattering are collagen fibre bundles and red blood cells which are at least three times larger than the wavelength. Thus, the scattering coefficient is expected to change slightly with the minor shift of wavelength. An anisotropy factor g is used to describe the scattering anisotropy of a medium, where $g = 0$ represents isotropic scattering and $g \to 1$ as scattering becomes more forward biased. The diffusion approximation assumes isotropic scattering through all media by using the transport scattering coefficient: $\mu_s^{'} = \mu_s(1 - g)$.

3.1.3 Absorption

Absorption is an effect that is explained at the atomic scale as the conversion of photons into other forms of energy, such as thermal energy upon collision with atoms. More specifically, the effect is most likely to occur when the energy of a photon (determined by its frequency) coincides with one of the excited states of the atom it is colliding with. The direct relationship to the effective transmission of light through a medium makes absorption a key effect in most photon transport models. The absorption coefficient (μ_a) of a medium describes the effectiveness of absorption for a given wavelength λ. A schematic diagram of absorption is shown in Figure 3.4.

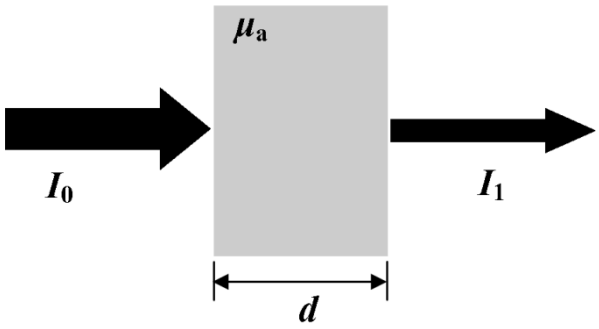

Figure 3.4 – Absorption of light through a homogeneous medium with absorption coefficient μ_a and thickness d. The output light intensity of a purely absorptive medium follows the Beer-Lambert law: $I_1 = I_0 \exp(-\mu_a d)$.

As mentioned in the Chapter 2, blood is responsible for most of the fluid exchange taking place in the human body, and as such, represents its dynamic nature in terms of tissue optics. The applicability of PPG techniques relies on the relative differences in the absorption of light from different haemoglobin species in the blood. The cardiovascular pulsations lead to an oscillation in tissue absorption due to variation in blood perfusion and optical path length. Consequently, the quality of PPG signals relies on the fact that blood is a high absorber in relation to other tissues.

3.1.4 Birefringence

Birefringence is the property of a material whose refractive index is a function of both the polarization and the orientation of incident light, and it is commonly found in biological tissue due to their fibrous nature at a microscopic scale. Standard photosensitive devices are generally assumed to have negligible polarisation sensitivity when detecting normally incident radiation, but they do present increasing sensitivity as the angle of incidence is increased. When using a randomly polarized light source, the nonlinearity of a detector under randomly incident light originating from a randomly polarized light source such as a LED can be considered negligible. In general terms, polarisation-sensitive detection methods make use of polarising materials to measure the effects of birefringence on the transmission of light in a sample. For instance, optical coherence tomography (OCT) can provide additional structural information of biological tissue [61], which is lack in its polarisation-insensitive counterpart. It is reasonable to disregard polarisation as a contributing effect in light propagation studies that do not specifically seek characterisation of birefringence effects.

3.2 MATHEMATICAL MODELS

In this section, we introduce mathematical models used to describe the propagation of light through human tissue. Most biological tissue is a turbid medium with strong scattering; hence, it is possible to describe the propagation of light in tissue from the wave perspective by using multiple scattering electromagnetic theory [62]. Tissue can be considered as a random medium whose permittivity, fluctuates with respect to position in 3D space. However, the lack of information pertaining to the permittivity of human tissue and the lack of readily applied models means that this formulation finds little applicability in tissue optics. The remaining models rely on the photon perspective of light. Actually numerous photon diffusion model have been developed attempting to address the problem. For instance, a rigorous mathematical description based upon the Radiative Transport Theorem which incorporates anisotropic scattering has been introduced to provide a more accurate photon propagation model. Nevertheless, the greatly increasing mathematic complexity and calculation consumption for the complicated multilayer tissue structure limits the application of this model. In contrast, the simplified Beer-Lambert model describes the effective optical absorbance of a medium when light travels through a given path length, disregarding scattering effects within human tissue. A modified Beer-Lambert model which considers the scattering effect has been introduced and gained a resurgence of interest. In this section, these three models used for *in-vivo* optical propagation are recounted towards investigating an accurate yet applicable opto-physiological model.

3.2.1 Radiative Transport Theorem

Propagation of light in tissue can, in principle, be described using fundamental electromagnetic theory. Based upon radiative transport theory, the propagation can be simplified by only considering the flow of energy through the medium, which gives a very good approximation for large thickness of biological tissue in the near infrared region. The following formulation of the radiative transport equation considers monochromatic light and disregards polarization:

$$\frac{\partial I(\boldsymbol{r},\boldsymbol{s})}{\partial \boldsymbol{s}} = -\mu_t I(\boldsymbol{r},\boldsymbol{s}) + \frac{\mu_s}{4\pi}\int_{4\pi} I(\boldsymbol{r},\boldsymbol{s}')P(\boldsymbol{s},\boldsymbol{s}')d\boldsymbol{\Omega}' \qquad [\mathbf{3.1}]$$

The first term represents the net change in energy due to energy flow, where $I(\boldsymbol{r},\boldsymbol{s})$ is the radiance at the position $\boldsymbol{r}$ in direction $\boldsymbol{s}$. The second term represents the radiance lost due to absorption and scattering: $\mu_t = \mu_a + \mu_s$, where μ_s is the scattering coefficient and μ_a is the

absorption coefficient. The last term denotes the gain in radiance due to scattered light incident from all directions. The light energy per unit area confined within solid angle $d\boldsymbol{\Omega}'$ coming from the direction $\boldsymbol{s}'$ is $I(\boldsymbol{r},\boldsymbol{s}')d\boldsymbol{\Omega}'$ with scattering probability density function $P(\boldsymbol{s},\boldsymbol{s}')$ for scattering from $\boldsymbol{s}'$ to direction $\boldsymbol{s}$.

A linear increase in the accuracy of a model for light propagation in *in-vivo* human tissue results in an exponential increase in its complexity. The high computational cost of numerical solutions to the radiative transport equation is a clear illustration of this. Numerical methods, such as Monte Carlo (MC) simulation, have been widely used to solve the radiative transport equation. As a statistical based technique, MC ray-tracing simulates the process of macroscopic optical propagation in tissue and evaluates the losses due to absorption. MC simulation has been applied in different photon diffusion models of skin. For instance, Graaff and colleagues have emphasized the importance of light scattering in understanding reflectance pulse oximetry via MC simulation of light travelling through a homogeneous single layer skin model [63], and Tuchin has employed MC simulation to solve the inverse problem of obtaining optical parameters from tissue samples based upon a five-layer model [64].

3.2.2 Beer-Lambert Model

The Beer-Lambert law describes the light transmitted through a medium of a known optical length and absorbance to the concentration of the medium and has found its practicability in pulse oximetry. The degree of absorption depends upon the nature of the trans-illuminated material and the wavelength of the illumination. Experimental measurements are usually made in terms of incident and transmitted light intensity in transmission mode. The relationship between the incident and transmitted light could be obtained from the Beer-Lambert law as:

$$I_1 = I_0 \exp(-\mu_a d) \qquad [\mathbf{3.2}]$$

where I_0 is the incident and I_1 transmitted light intensity respectively, μ_a is the absorption coefficient at a specific wavelength in units of mm^{-1}, and d is the optical path length through the medium. When applying this formulation of the Beer-Lambert law to a dynamic opto-physiological system, μ_a is assumed to have static and dynamic components:

$$I_1 = I_0 \exp\left(-\left(\mu_{a,s} d + \mu_{a,a} r(t)\right)\right) \qquad [\mathbf{3.3}]$$

where $\mu_{a,s}$ is the wavelength-dependent absorption coefficient of the static component of tissue, and $\mu_{a,a}$ is the absorption coefficient of arterial blood. Here d and $r(t)$ represent the constant optical path length of static components and dynamic path length of arterial components respectively.

It has previously been demonstrated that when transilluminating a thick section of a highly scattering medium, it is still possible to apply a simple Beer-Lambert calculation to convert the measured variations in attenuation to changes in the absolute concentration of chromophores [65]. In transmission mode PPG measurements, it is possible to know the minimum optical path length (i.e., the distance between light source and detector). However, the effective optical path length, as used in the calculation, increases when taking into account the effects of multiple scattering [66].

3.2.3 Modified Beer-Lambert Model

As mentioned above, in Beer-Lambert model, the absorbance A of tissue can be expressed as the log to the base e of the ratio of the intensity of the incident light I_0 to the transmitted light I_1:

$$A = -ln\left(\frac{I_1}{I_0}\right) = \mu_a d \qquad [\mathbf{3.4}]$$

If scattering and tissue geometry are considered, the attenuation in optical density will be a complex function of detector and transmitter geometry, scattering and absorption properties of tissue:

$$A = -ln\left(\frac{I_1}{I_0}\right) = B\mu_a d + G \qquad [\mathbf{3.5}]$$

where G is a geometry dependent factor which is independent of absorption and represents intensity loss caused by scattering, B is a path length factor dependent upon the absorption and scattering coefficients and scattering phase function, and d is the inter-optode distance between source and detector. This equation is referred to as the modified Beer-Lambert law [66]. Since its conception in 1988, the modified Beer-Lambert law has been widely applied in near-infrared tissue spectroscopy to quantify the concentration changes of tissue chromophores, mainly oxy- and deoxyhemoglobin [67]. For instance, under the simple assumptions that G is constant and the time varying physiological components lead to changes in absorption but not

to changes in scattering or tissue geometry, the differential form of the modified Beer-Lambert law could be expressed as:

$$\Delta A = -ln\left(\frac{I_{1,t_1}}{I_{2,t_2}}\right) = B\Delta\mu_a d \qquad [\mathbf{3.6}]$$

Here, the attenuation change can be calculated from the detected intensity values of two different states of the tissue, and is proportional to the change in absorption, i.e., the concentration of tissue chromophores: $\Delta\mu_a = \alpha_{\mathrm{HbO_2}}\Delta c_{\mathrm{HbO_2}} + \alpha_{\mathrm{Hb}}\Delta c_{\mathrm{Hb}}$, where α weights demote the specific absorption coefficients of the chromophores.

3.3 PROPRIETARY OPTO-PHYSIOLOGICAL MODEL

As mentioned above, the radiative transport theorem considers light as the flow of energy through a medium. However, a high degree of accuracy in its implementation manifests as a high computational cost, thereby limiting its practicability and applicability especially when being applied to complex tissue structures. On the other hand, the Beer-Lambert law which assumes a homogeneous non-scattering medium is clearly oversimplified. Following the assumptions of the Beer-Lambert law, the detected irradiance in a transmission mode PPG would depend on the perpendicular alignment between light source and sensor and the path length for a given source beam profile. However, this is not the case in real tissue optics settings, where scattering results in the diffusion of transmitted intensity, which in turn modulates the effective irradiance at a detector. The modified Beer-Lambert law, which accounts the effects of both absorption and scattering, increases the accuracy of the model predictions. Nevertheless, a proper and applicable optical model for a reflection imaging PPG system is still lacking.

In the model developed in this thesis, the skin tissue is treated as a multi-layered structure with respectively dynamic blood volume changes. Following this idea, quantification of the iPPG signals requires knowledge, or at least an estimate of the optical path in the medium. To date, various methods have been proposed to estimate the optical path length through tissue. For instance, in the application of the modified Beer-Lambert law, the time-resolved and intensity-modulated spectroscopy that determines the photon mean time-of-flight or the phase shift of an intensity-modulated light wave have been applied to estimate the optical path length [65, 68]. However, the complexity and the cost of these systems prohibit their implementations in iPPG. Another approach is relying on Monte Carlo (MC) simulation, a numerical solution of the radiative transport equation, to theoretically derive the optical path length. MC simulation

offers the chance to model light behaviour in arbitrarily complex tissue structures and correlates the optical path length with the various parts or segments of biological tissue. Therefore, an opto-physiological mode with reasonable computation complexity could be obtained via introducing the scattering-related time varying optical path length into the Beer-Lambert law since the path length could be derived from the output of the MC simulation. In this section, we consider the set of simplifying assumptions that can be made in order to find an optimal opto-physiological model for reflectance mode imaging PPG. More importantly, we have considered the motion artefacts modulation on the obtained PPG signals, and introduced a theoretical motion modulated function which might help to attenuate the motion artefacts to achieve reliable and effective physiological assessments. The applicability and proprietary of the opto-physiological model in theoretically estimating the physiological parameters, such as pulse rate, pulse rate variability, perfusion map and pulse transit time, is also demonstrated.

3.3.1 Revised Beer-Lambert Model

Light travelling a highly scattering medium (tissue) undergoes diffusion and on average travels a distance proportionally greater than the source-detector separation according to the degree of scattering in the medium. The following assumptions determine how subsequent post processing and modelling is performed:

- Time varying physiological components lead to changes in optical path length but not to changes in absorption and scattering coefficients and tissue geometry. The absorption is proportionally increased according to the effective path length increase due to scattering, which entails the use of a time-varying mean optical path length.
- The diffusion approximation provides a sufficiently rigorous description of optical scattering in all tissue of the arbitrary model [69], which involves the approximation of anisotropic scattering as isotropic where the diffusion approximation could be applied numerically by converting μ_s and g to through the relation $\mu_s' = (1 - g)\mu_s$.

Under these assumptions, the PPG formulation of the Beer-Lambert law can be modified to include a more descriptive characterization of optic-tissue interaction that is in line with standard tissue optics data found in the literature:

$$I_1 = I_0 exp(-\mu_a d(\mu_s', t)) \qquad [\mathbf{3.7}]$$

where μ_a is the wavelength-dependent absorption coefficient, $d(\mu_s', t)$ is the scattering dependent time varying optical path length. It follows that Equation 3.7 can only hold true if all light exiting the scattering medium is accounted for. A schematic diagram illustrates the light propagation in a reflection PPG detection model.

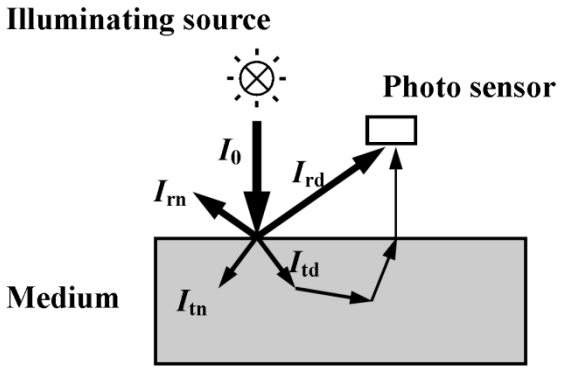

Figure 3.5 – Schematic diagram of the light propagation. I_0 is the total incident light, I_{rn} is the undetected reflected light intensity while I_{rd} is the detected directed reflected light intensity which accounts for the majority of the detected light intensity, I_{tn} is the undetected transilluminating light intensity while I_{td} is the detected transilluminating light intensity. These light intensity follows: $I_0 = I_{rn} + I_{rd} + I_{tn} + I_{td}$.

Therefore, only the transilluminating attenuated intensity term I_{td} contains the key physiological information and the Equation 3.7 could be rewritten as:

$$I_{det} = I_{rd} + I_{td} exp(-\mu_a d(\mu_s', t)) \quad [\mathbf{3.8}]$$

where I_{det} is the total detected light intensity and I_{rd} is the detected directed reflected light intensity which accounts for the major parts of DC components in PPG signals. We define the physiological part of the detected intensity as:

$$I_{sig} = I_{det} - I_{rd} = I_{td} exp(-\mu_a d(\mu_s', t)) \quad [\mathbf{3.9}]$$

3.3.2 Time-Variant Optical Path Length

It is well known that the time-varying nature in the PPG signal is a result of the periodic oscillation in the perfusion of blood vessels and that the periodic oscillation is synchronized with the heart beat. Here the assumption of tissue homogeneity is necessary due to the inherent difficulty to create a model that accurately distinguishes between tissues and their blood vessels. Subsequently, changes in perfusion can be modelled as a homogeneous change in the optical

path length of the tissue. Here we can use a coefficient to represent the variation in optical path length with respect to a static path length, thus developing a complete description of d:

$$d(\mu_s', t) = d(\mu_{s,t}') + d(\mu_{s,b}') \times (1 + \varepsilon\Phi(t)) \quad [\mathbf{3.10}]$$

where $d(\mu_{s,t}')$, is the static path length mainly attributed to the optical properties of tissue, $d(\mu_{s,b}')$ is the static path length attribute to the blood component, $\Phi(t)$ is a function that represents the time-varying nature of the PPG waveform and ε is the modulation coefficient of pulsatility. The function $\Phi(t)$ ranges from 0 to 1 for $d(\mu_s', t)$ oscillating between $d(\mu_{s,t}') + d(\mu_{s,b}')$ and $d(\mu_{s,t}') + d(\mu_{s,b}') \times (1 + \varepsilon)$. Therefore, we could re-write Equation 3.9 as:

$$I_{sig} = I_{td} exp\left(-\left(\mu_{a,t} d(\mu_{s,t}') + \mu_{a,b} d(\mu_{s,b}') + \varepsilon\mu_{a,b} d(\mu_{s,b}')\Phi(t)\right)\right) \quad [\mathbf{3.11}]$$

The first term on the right side represents the attenuation due to the static tissue components; the second term represents the absorption attributed to static blood components; while the last term indicates the optical attenuation caused by the dynamic blood volume variation that yields the pulsatile waveform in the PPG signal. Following the Equation 3.3, the first two terms together represent the static attenuation while the last term represents dynamic attenuation.

Mathematically, it is useful and convenient to work with Beer-Lambert equations in forms of the ratio-metric attenuation or optical density (OD). Equation 3.11 therefore can be re-written as:

$$OD_{sig} = ln\frac{I_{sig}}{I_{td}} = -\left(\mu_{a,t} d(\mu_{s,t}') + \mu_{a,b} d(\mu_{s,b}') + \varepsilon\mu_{a,b} d(\mu_{s,b}')\Phi(t)\right) \quad [\mathbf{3.12}]$$

In terms of optical density, the attenuation of light through a multi-layered medium ($M = \{m_1, m_2, \dots, m_n\}$) is simply $I_{td} exp\,(OD_{sig1} + OD_{sig2} + \cdots + OD_{sign})$. Within each layer, the attenuation is only influenced by its own optical and geometric properties. For instance, in the outermost layers of human skin, i.e., epidermis, there are no blood components consequently yielding second and third terms of right side Equation 3.12 equal to zero.

3.3.3 Signal Quality

The Equation 3.8 & 3.9 demonstrated the detected backscattered light intensity, which contains the important physiological information. However, these Equations will hold true only in ideal condition, e.g., without different kinds of noise. In practical monitoring, the obtained plethysmographic signals might be influenced by various noises, e.g., motion artefacts,

quantization effect, and electrical noise. As detailed in Chapter 2, PPG is susceptible to motion-induced signal corruption. Given the remote monitoring mode for iPPG technique, the motion artefacts corruption becomes even worse, making motion artefacts attenuation one of the most challenging issues in iPPG study. This significant disadvantage limits the applications of iPPG. Hence, in this thesis, a mathematical model regarding to qualify the motion artefacts modulated iPPG signals have been presented prior to the applicability of the opto-physiological model in various physiological parameters measurements.

If we consider the complicated motion corruption as a function (f_m) to modulate the obtained PPG signals, e.g., weights and phase, the Equation 3.8 could be re-written as:

$$I'_{det} = f_m(I_{det}) = f_m\left(I_{rd} + I_{td}exp(-\mu_a d(\mu'_s, t))\right) \quad [\mathbf{3.13}]$$

Then the motion artefacts cancellation problem could be regarded as find the inverse function of the motion corruption (f_m^{-1}) that:

$$\hat{I}_{det} = f_m^{-1}\left(f_m(I_{det})\right) = I_{det} \quad [\mathbf{3.14}]$$

However, the motion artefacts could be incredible complicated, e.g., planar shift, rotation and the distance between sensing system and the medium could be increased or decreased. Hence, it is virtually impossible to obtain the ideal inverse function (f_m^{-1}) which could remove all motion artefacts. And in real condition, if we consider the simple situation, e.g., motion (S_m) is a physiological independent additive components, Equation 3.14 should be written as:

$$\hat{I}_{det} = \hat{f}_m^{-1}\left(f_m(I_{det})\right) = \rho I_{det} + (1-\rho)S_m \quad [\mathbf{3.15}]$$

where ρ ranges from 0 to 1. Here, in the present study, I am trying to introduce a proprietary technique to make the ρ to be close to 1. To make the model simple and applicable, only planar motion artefact, which is the most common artefact in the obtained iPPG recordings, were considered in the present study.

The description of the model starts from the 1-D motion artefact. Figure 3.6 presents the schematic of the 1-D shift (a) and the proposed motion modulated function (b).

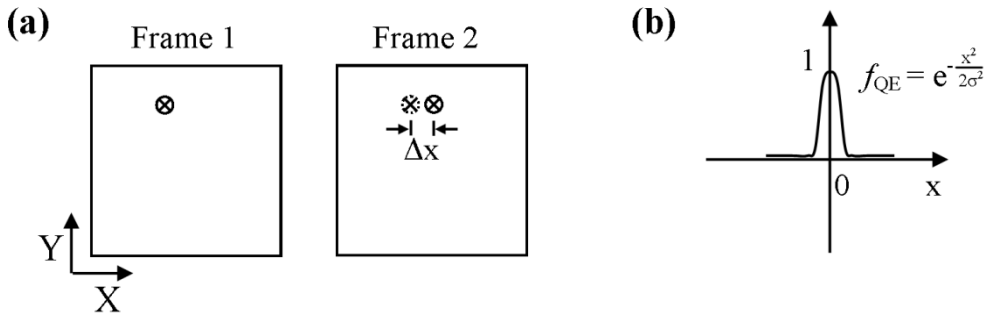

Figure 3.6 – Schematic diagram of the 1-D shift effect of the original frame (a) and the motion modulated function f_{QE} (b). Δx is the maximum 1-D shift.

Here, the motion modulated function is given as:

$$f_{QE_{1-\mathrm{D}}} = e^{-\frac{x^2}{2\sigma^2}} \qquad [\mathbf{3.16}]$$

where x is the shift and σ is the normalization parameter which is determined by the system setting. According to the definition of the motion modulated function, a simple yet efficient motion attenuation method could be achieved via spatial averaging. For instance, given the maximum shift of Δx, the signal quality might be increased via averaging approach because $\frac{1}{2\Delta x}\int_{-\Delta x}^{\Delta x} e^{-\frac{x^2}{2\sigma^2}}$ is bigger than the $e^{-\frac{\Delta x^2}{2\sigma^2}}$. However, with further increment of the averaging window size, the spatial resolution might be decreased yet the signal quality might not be significantly improved. The 1-D motion modulated function could be easily expended to 2-D:

$$f_{QE_{2-\mathrm{D}}} = e^{-\frac{x^2+y^2}{2\sigma^2}} \qquad [\mathbf{3.17}]$$

where x and y is the 2-D shift.

3.3.4 Applicability of the Opto-Physiological Model

Following from above, after the motion-compensation of the iPPG recordings, the proprietary opto-physiological model offers an opportunity to theoretically estimate the fundamental physiological parameters, e.g., pulse rate, pulse rate variability, perfusion map, and pulse transit time.

a) Pulse Rate

A heart cycle comprises two states, i.e., systole and diastole, where the optical density is different during these states. Specifically, the intensity of the attenuated light is highest during diastole when the diameter of the arterial vessels and hence the absorbance due to the blood volume is minimal, thus showing as a peak in the detected waveform. In contrast, the optical path length in the arteries increases during the systole period until the amount of absorbance reaches a maximum, which corresponds to the foot of the I_{sig}. Hence, the instantaneous heart rate can be extracted from the time interval of two successive peaks/feet which correspond to the local maximum/minimum point of the waveform. Mathematically, if there exists a $\lambda > 0$ such that $\Phi(t_i) \geq \Phi(t)$ where $|t - t_i| < \lambda$, the value at the point t_i is the local maximum point. Consequently we can obtain the time interval of two successive peaks: $\Delta t_i = t_{i+1} - t_i$, the inverse of which is the instantaneous heart rate. The average heart rate for a sequence of n heart cycles can therefore be calculated as:

$$HR = \sum_{i=1}^{n} \frac{1}{\Delta t_i} \qquad [\mathbf{3.18}]$$

Here the value of λ is very important since it determines the local range for the maximum detection. For example, if it is greater than a heart cycle; only one peak is detected yielding a missing peak thereby miscalculating the heart rate. In a practical setting, the local maximum/minimum points could be obtained via zero-crossing calculation methods through calculating the differences between adjacent elements of the original signal.

b) Pulse Rate Variability

Pulse rate variability (PRV), referring to the variations of the pulse-to-pulse intervals obtained from PPG signals, has recently been demonstrated as a surrogate for Heart rate variability (HRV) [70]. For instance, one recent PRV study has indicated that habitual smoking is associated with parasympathetic withdrawal and augments sympathetic nerve activity [70]. HRV is a physiological phenomenon where time interval between heart beats varies. The analysis of HRV is important when studying the autonomic nervous system for its potential in evaluating the equilibrium between the sympathetic system (which accelerates the heart rhythm) and parasympathetic system (which decelerates the heart rhythm). The continuous changes in the sympathetic-parasympathetic balance trigger the sinus rhythm to exhibit fluctuations around the mean heart rate. These fluctuations are adjusted by the cardiovascular control system. It is now well known that the properties of HRV may play an important role in the better

prognosis in patients with heart failure, diabetes and autonomic dysfunction [32]. Besides, it is generally believed that the variations between consecutive beats are a critical parameter in the cardiovascular assessment. As mentioned above, the sequence of the time interval between two successive peaks is denoted as $\{\Delta t_i\}$ for $i = 1,2,\dots,n$. The variations of the beat-to-beat interval can then be obtained and further analyzed.

c) Perfusion Map

As introduced in Chapter 2, one significant advantage of iPPG technique is the blood perfusion information, which offers added value for appraising the cardiovascular system and characterizing vascular skin lesions. The iPPG signal which contains a dynamic component attributed to the pulsation of arterial blood and a static component governed by the static part of tissue. Hence, the Equation 3.11 could be further divided according to Equation 3.3, which facilitates the separation of the dynamic and static components.

$$I_{sig} = I_{sig\_dc} exp\left(-\varepsilon \mu_{a,b} d\left(\mu'_{s,b}\right)\Phi(t)\right) \quad [\mathbf{3.19}]$$

where I_{sig_dc} could be obtained as:

$$I_{sig\_dc} = I_{sig} \exp\left(-\left(\mu_{a,t} d\left(\mu'_{s,t}\right) + \mu_{a,b} d(\mu'_{s,b})\right)\right) \quad [\mathbf{3.20}]$$

Taylor expansion of Equation 3.14:

$$I_{sig} = I_{sig\_dc} - I_{sig\_dc}\left(\varepsilon \mu_{a,b} d\left(\mu'_{s,b}\right)\Phi(t)\right) + O\left(\left(\varepsilon \mu_{a,b} d\left(\mu'_{s,b}\right)\Phi(t)\right)^2\right) \quad [\mathbf{3.21}]$$

As indicated in the literature that the dynamic component of the absorption only accounts for a few percent (0.1-2%) of the total absorption [46, 71], the third term of Equation 3.16 could be neglected. Hence, the Equation 3.16 could be approximated as:

$$I_{sig} \cong I_{sig\_dc} - I_{sig\_dc}\left(\varepsilon \mu_{a,b} d\left(\mu'_{s,b}\right)\Phi(t)\right) \quad [\mathbf{3.22}]$$

Then the perfusion information could be obtained through normalization to eliminate the influence of the light source:

$$I_{perfusion} = \left|\frac{I_{sig\_ac}}{I_{sig\_dc}}\right| = \frac{I_{sig\_dc}\left(\varepsilon \mu_{a,b} d\left(\mu'_{s,b}\right)\Phi(t)\right)}{I_{sig\_dc}} = \varepsilon \mu_{a,b} d\left(\mu'_{s,b}\right)\Phi(t) \quad [\mathbf{3.23}]$$

Several studies have been recently published to employ perfusion information in characterizing different vascular skin lesions [45, 48]. For instance, a higher strength of the signal has been observed in the wound skin region than the healthy skin [45]; Verkruysse and colleagues have reported an remote plethysmographic imaging technique and demonstrated its practicability in detecting the port wine stains [48], i.e., a higher intensity of the perfusion is revealed in the port wine stains as compared to surrounding normal skin.

d) Pulse Transit Time

As mentioned in Chapter 2, pulse transit time (PTT) – the time it takes a pulse wave to travel between two arterial sites – is clinically important due to its ability to assess the arterial stiffness, a parameter related to the cardiovascular morbidity and mortality. Originally PTT is measured by recording the time interval between the passages of the arterial pulse wave at two consecutive sites. Typically, the arrival time of the pulse is determined from the systolic foot of the PPG signal. In this thesis, we intend to derive these important physiological parameters from iPPG signals recorded from the back, i.e., from the 3rd thoracic vertebra to 12th thoracic vertebra. Hence, the following assumptions determine how the measuring site is modelled:

- All time-varying components derived from a PPG signal are solely attributed to dynamic blood volume variations. This entails the use of time-varying optical path lengths.
- The time taken for the physiological pulse wave to travel two arterial vessel segments of equal scale to the closest segments of skin surface is equivalent. This facilitates the use of time differences derived from PPG signals as a measure of PTT (t_{diff}).

Following the Equation 3.14 two iPPG signals could be obtained from two carefully selected regions (as indicated in Figure 3.7):

$$I_{ac1} = I_{sig\_dc1} exp\big(-\varepsilon \mu_{a,b} d(\mu'_{s,b}) \Phi(t_1)\big) \quad [\mathbf{3.24}]$$

$$I_{ac2} = I_{sig\_dc2} exp\big(-\varepsilon \mu_{a,b} d(\mu'_{s,b}) \Phi(t_2)\big) \quad [\mathbf{3.25}]$$

With the method mentioned above (local minimum/zero-crossing), the foot of these two signals could be extracted. The time difference ($t'_{diff} \cong t_{diff}$) between two feet thereby could be obtained.

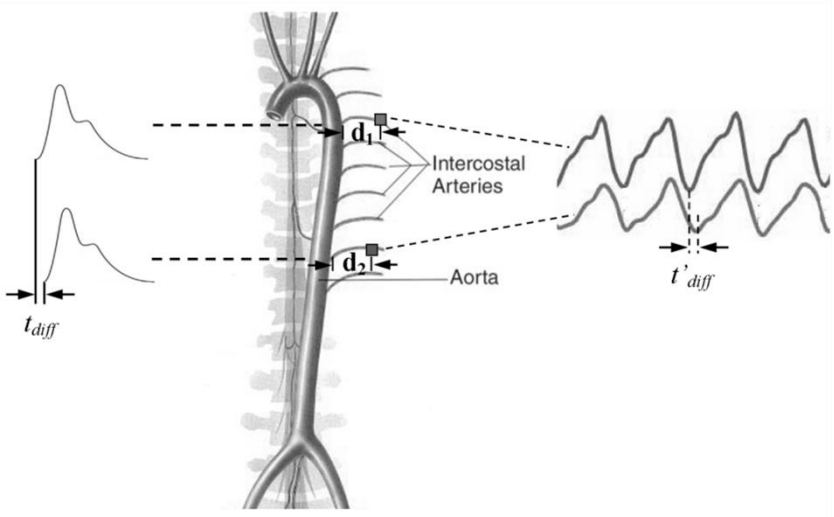

Figure 3.7 – Diagrammatic representation of the aorta and intercostal arteries. The time difference between two pulse waves is also demonstrated.

As introduced in Chapter 2, objective assessment of vascular aging is clinically important for its correlation to morbidity and mortality. A parameter, which is a measure for the arterial stiffness, is the arterial distensibility D defined by:

$$D = \frac{dV/dP}{V} \qquad [\mathbf{3.26}]$$

where dV is the increase in the arterial blood volume V in response to the increase dP in the arterial blood pressure. An indirect method for the assessment of D is by measuring the pulse wave velocity (PWV) which is related to D by Bramwell-Hill formula [72]:

$$\text{PWV} = (\rho D)^{-1/2} \qquad [\mathbf{3.27}]$$

where ρ is the blood density. Two PPG probes along an artery can measure the PTT between the two probe sites and consequently assess PTT along the artery under the assumption that the transit time from the artery to the tissue small arteries and arterioles. In practice, PWV calculation requires an accurate measurement of the vascular transit path between two measuring sites, i.e., in the present study, the two carefully chosen regions are corresponding to *a)* a common arterial vessel or *b)* two arterial vessels with a common parent vessel.

This chapter has recounted the concepts of optics and physiology that are relevant to the research project, specifically those pertaining to human tissue optics and the circulatory system. Two main mathematical models used to describe the propagation of light through human tissue have been presented: the rigorous radiative transport theorem and simplistic (modified) Beer-Lambert model. More importantly, the proprietary opto-physiological model has been derived from these aforementioned models and its applicability has been detailed.

4 EXPERIMENTAL SETUP AND METHODOLOGY

This chapter has provided the main aspects of the methodology applied in this project. Basically, the experimental platform of this research, consisting of hardware and software elements, aims to provide a detailed description of the physiological assessments involved in clinical environments. The hardware, containing a series of sensor design, light source and digital camera arrangements, provides the empirical image recordings while the software algorithms of the present iPPG platform, which consist of image registration, image segmentation, blind source separation, and time-frequency representation techniques, has been proposed to address the key issues of motion corruption and data handling in iPPG signal processing.

4.1 EXPERIMENTAL PLATFORM OVERVIEW

This section presents an experimental iPPG platform that has been created for the applicable and reliable implementation of non-contact physiological assessments. The complete experimental platform consists of a hardware setup used for recording of images and a software platform that extracts the important physiological parameters from these recorded images. The hardware setup includes two separate systems: sensing system and reference system. Sensing system, composing of camera, lens, light source and frame grabber, provides the empirical image recordings while the reference system serves as validation. PPG signals are known to be susceptible to motion-induced signal corruption; the software platform therefore attempts to solve this problem via motion artefacts attenuation techniques. Subsequent software stages perform the extraction and analysis of physiological parameters. An overview diagram of the experimental iPPG platform has been demonstrated in Figure 4.1.

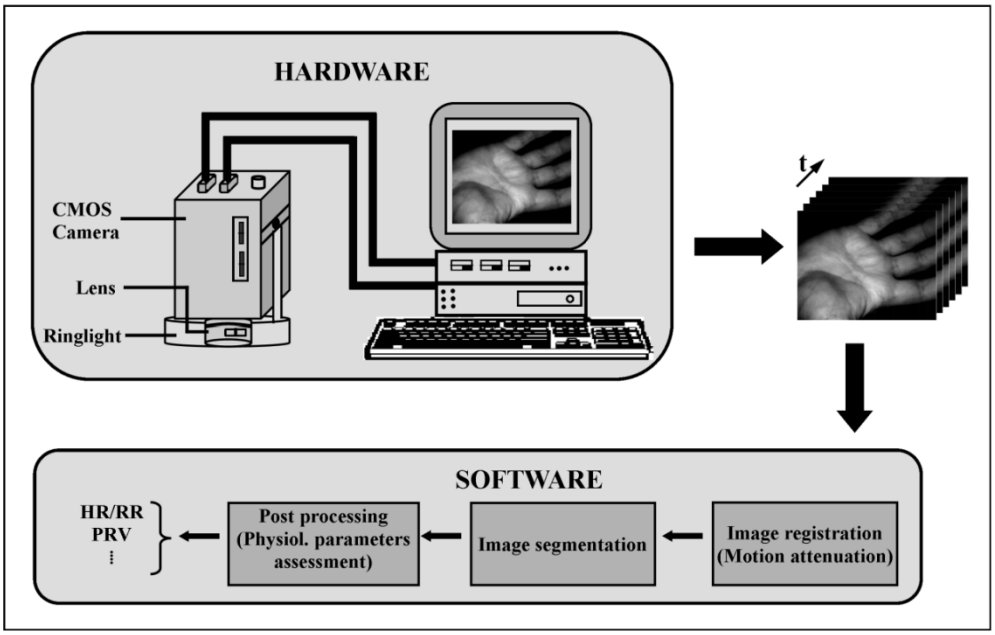

Figure 4.1 – The overview diagram of the novel experimental iPPG platform.

4.2 HARDWARE

In the past decade, an accumulation of iPPG studies have been published following the resurgence of PPG technology, where iPPG setups have been proposed for various biomedical and clinical applications. Nevertheless, no standard design that is suitable for multiple

physiological parameters assessments has been reported. Table 4.1 summarises the key publications of different iPPG systems. In the present study, a hardware platform that is able to record the images according to different requirements and situations was developed and validated for non-contact physiological assessments. These recorded images were further categorised and analyzed with the novel software platform to extract the embedded physiological parameters, e.g., heart/respiration rate. The novel iPPG setup introduced in the present study includes a sensing platform and a validation/reference platform.

4.2.1 Sensing Hardware

Similar to the conventional PPG sensor, an iPPG system also needs a light source and a sensor to function. Hence, the sensing hardware which includes (a) light source and (b) camera is the key component within an iPPG system. Nowadays, iPPG techniques could be further categorized into two aspects: webcam based iPPG and experimental camera based iPPG. The former setup shows its advantage of low cost and simplicity of usage, e.g., normally uses ambient light as the light source. The main drawback of the webcam iPPG system is the low sample speed, typically around 15/30 frames per second (fps). While experimental camera based iPPG, coupled with designed light source, could overcome this problem. Hence, in the present study, an experimental monochrome CMOS camera based iPPG system has been developed for remote physiological assessments.

4.2.1.1 Light source

In contrast to the simple structure in conventional PPG sensors, the light source for the iPPG setup, particularly the wavelength and structure, should be carefully handled. As detailed in Chapter 2, the practical wavelength suitable for iPPG is also limited in the red/near-infrared spectral range, typically from 600 to 1000nm, allowing high contrast in the absorption of blood. The near-infrared light, which has been proven to enter the skin relatively unrestrained and penetrate deeper, was deemed an optimum range for the present study. Besides, the light source of the iPPG setup should have a combination of uniformity and high intensity. Since there is no standard design of the light-source structure in iPPG setup, two different models, e.g., a ringlight source and a square light source have been employed and validated in the present study.

Table 4.1 – List of iPPG studies.

Study No.	Reference	Hardware setup			Physiological assessments				Remarks
		camera	Light-source	Sample rate (fps)	HR	RR	SaO_2	Perfusion	
1	Hulsbusch (2002) [46]	Experimental CCD camera	LED (800nm)	>8	X	X		X*	Time-frequency representation Wound skin
2	Wu (2003) [75]	B/W CCD camera	NIR Ringlight (875nm) /Multiple wavelength (green, red, infrared)	>5	X	X		X	Multitask perfusion tests
3	Wieringa (2005) [52]	Monochrome CMOS-camera	3λ-LED-rightlight (λ_1=660, λ_2=810, λ_3=940nm)	6.7/13.7	X	X	X†	X	Light source design (Multiple λ) Image pre-processing
4	Humphreys (2005) [74]	Monochrome CMOS-camera	2 NIR diodes (λ_1=760 λ_2=880nm)	30 per λ			X		Real SaO_2 assessments
5	Humphreys (2007) [49]	Monochrome CMOS-camera	2λ NIR LED array (λ1=760, n=18; λ2=880nm, n=18)	16 per λ	X		X		Statistical validation with cPPG
6	Verkruysse (2008) [48]	Digital camera	Ambient light	15/30	X	X		X‡	Wave propagation Characterization of vascular skin lesions (PWS)
7	Zheng (2008) [73]	CMOS-camera	2λ NIR ringlight (λ_1=660, λ_2=880nm)	21 per λ	X			X	—
8	Poh (2010) [47]	Webcam	Ambient light	15	X				Motion tolerant technique Multiple subjects' monitoring
9	Sun (2011) [76]	Monochrome CMOS-camera	NIR ringlight (870nm)	20/50	X	X			Motion attenuation method

* Both the heart beat and respiratory signal strengths are higher in the wounded skin region.

† A breakthrough study led to insights into contactless SaO_2 assessment though SaO_2 calculation was not actually conducted in the literature.

‡ Significant achievements in characterization of vascular skin lesions with phase mapping (port wine skin), with clear applications in clinical community.

a) Ring Light

A custom built infrared (λ=870nm, Δλ=15nm) ringlight illumination source (RIS) comprising 100 RCLEDs (model: 0603SMD, JMSienna) fitted into a ring reflector has been designed and verified initially in the present study. The RIS was mounted around the camera lens to collimate the distribution of light and current-controlled and synchronized with the camera capture cycle.

***Design*:** To increase the performance and integrability of the iPPG system, the ideal position of the ring light is around the camera. This coaxial setup provides a high light intensity within the centre of the captured image. To make the light distribution uniform, a parabolic reflector was further designed and validated with OptiCAD (OptiCAD 10, OptiCAD Corporation, USA). A 3-D model (Figure 4.2) was initially built and transferred to OptiCAD for simulation.

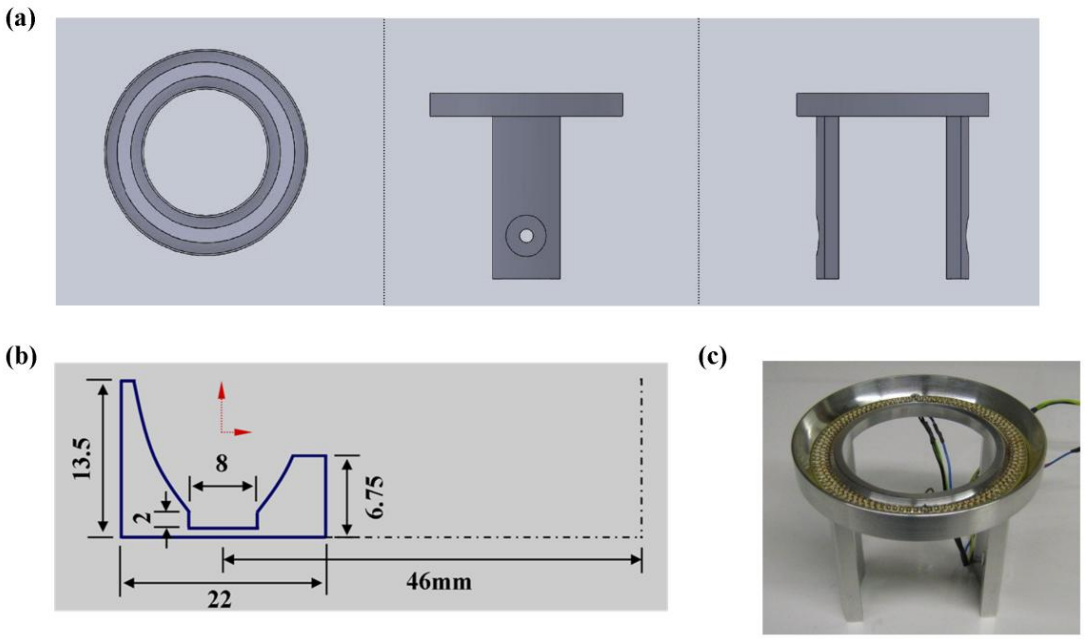

Figure 4.2 – (a) The 3-D scheme, (b) the parameters of the custom-built parabolic reflector, and (c) an image of the ringlight.

Once the parameters of the 3-D model were transferred into OptiCAD, a simulation was conducted, where multiple standard spherical surface LEDs, as provided within OptiCAD, were employed to demonstrate the performance of RCLEDs. To get the light intensity distribution for each LED, 20×20 rays were traced using a 130 degree viewing angle. The surface of the reflector was set to pure reflective (no energy loss upon reflection). A 500×500

mm square size frame was fixed 400 mm in front of the ringlight to quantify the energy and to assess the uniformity. Figure 4.3 shows the illumination configuration.

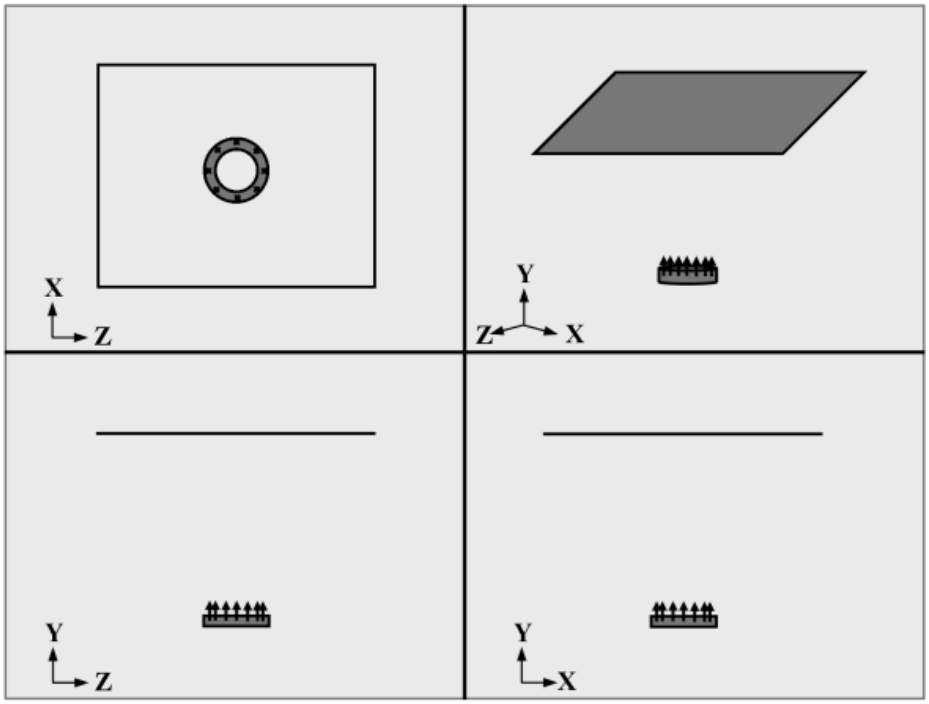

Figure 4.3 – The schematic of the simulation setup in OptiCAD, with the black arrow in the ring indicating the position of each LED (in this demonstration 8 LEDs).

To test the distribution of the light intensity, the rays hitting on a 50×50 mm sub-window within the frame were further numbered and normalized with respect with the total number/intensity (Figure 4.4). Here, the simulation was undertaken using 64 LEDs instead of 100, following the observation that quantisation effects on radiant power distribution were negligible for circular arrays of more than 32 LEDs.

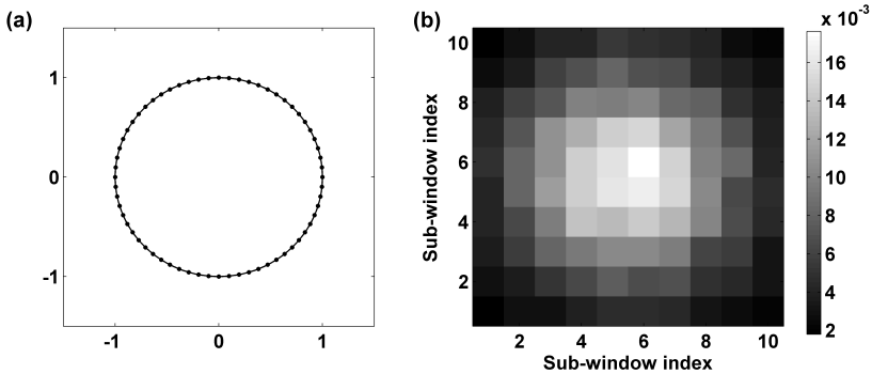

Figure 4.4 – The simulated performance of the ringlight (b) with colour bar showing the normalized light intensity within each sub-window. The position of each LED (64 total) is indicated with a black dot (a).

***Control circuit*:** To increase the temperature stability and accuracy of the light source, a circuit with a microcontroller (Model: PIC16F876-047SP, MicroChip, USA) was designed to current control the ringlight and guarantee the synchronization between light source and camera. Specifically, the control circuit receives a 'frame valid' signal from the digital camera, according to which the circuit drives the ringlight. The circuit also works in continuous power driven mode for short-term recordings. The image and structure of the control circuit is shown in Figure 4.5.

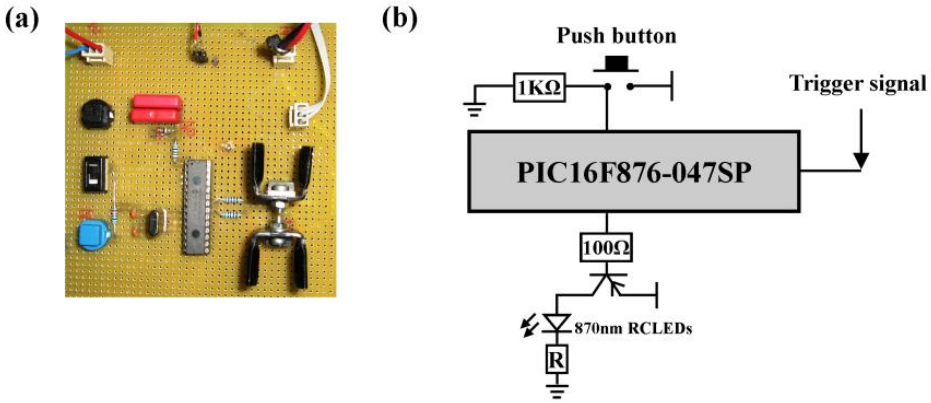

Figure 4.5 – The image (a) and structure (b) of the ringlight control circuit.

***Real Performance*:** The 100 RCLEDs were attached to a custom made printed circuit board with integral series resistors for each RCLED. The image of the ringlight and its working status is demonstrated in Figure 4.6. To test the real performance of the light source, a 400×400 mm square non-reflective target was initially employed, and the sub-window was set as 50×50 mm. The power distribution was obtained in a dark room through measuring the real power within each sub-window with an optical power meter (Model: 835 Optical power meter, Newport

Corp., USA) and a matched photodetector (Model: 818-SL, Newport Corp., Irvine, USA). The distance between the light source and target was set at 400 mm. Figure 4.6 (c) shows the real power distribution of the ringlight, which is in good agreement with the simulation results (Figure 4.4).

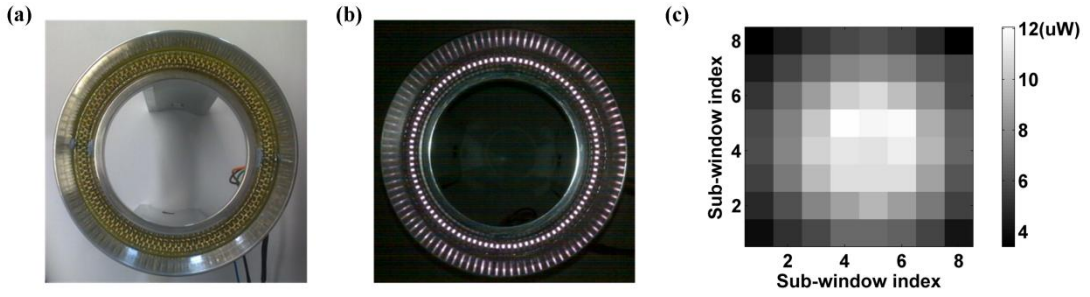

Figure 4.6 – The image of the ringlight (a), working status (b) and its performance (c).

Although the custom-built ringlight shows some qualities and advantages, e.g., integrability and uniformity, its intensity seems to be a drawback in the real recording situations. For instance, the maximum light intensity is only about 12 μW at a distance of 400 mm (Figure 4.6 (c)), which could not satisfy the requirements when a fast frame rate is needed, e.g., pulse transit time and pulse rate variability analysis. Therefore, to overcome this disadvantage, one commercial infrared light source with 56 infrared LEDs has been employed.

b) Commercial Light Source

As mentioned above, to increase the light intensity and maintain the uniformity, 56 infrared LEDs (λ=880 nm, Δλ=20 nm) commercial light source (Model: ABUS TV 6818, ABUS Security-Centre GmbH, German) has been verified in the present study (Figure 4.7 (a)). The horizontal and vertical angle of radiation is 60º and 40º respectively.

***Performance*:** The real performance of the commercial IR light source was obtained through measuring the power with an optical power meter (Model: 835 Optical power meter, Newport Corp., USA) and a matched photodetector (Model: 818-SL, Newport Corp., Irvine, USA) in a dark room. A 400×400 mm target frame was set 500 mm in front of the illuminator and the sub-window size is 50×50 mm. As it can be seen that a square high light intensity pattern is revealed in the power distribution map (Figure 4.7 (b)). Compare to the custom-built ringlight, the light intensity increase almost 100 times yet still safe for clinical experiments according to [77].

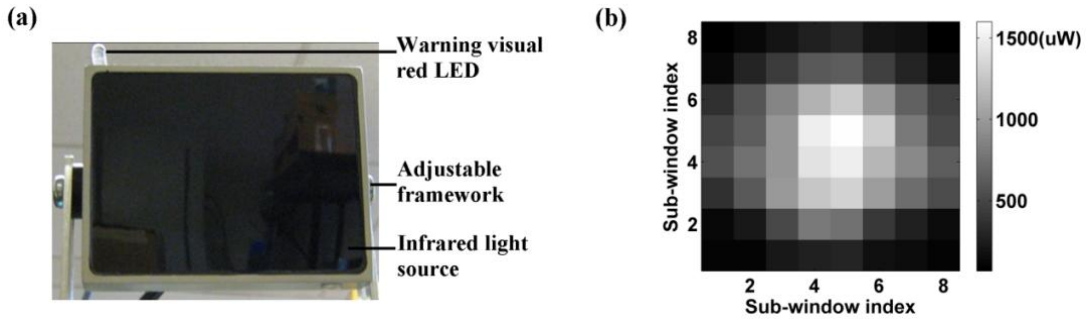

Figure 4.7 – The image of the commercial infrared light source (a), and its performance (b).

***Warning system*:** The significantly increased light intensity would become suitable for the measurements of PTT and PRV which requires fast frame rate and short exposure time. Accordingly, the light source was always on. With the invisible infrared light, a warning system, containing both auditory and visual warning signals, was also designed to indicate the working status of the light source. An image of the warning system is demonstrated in Figure 4.8.

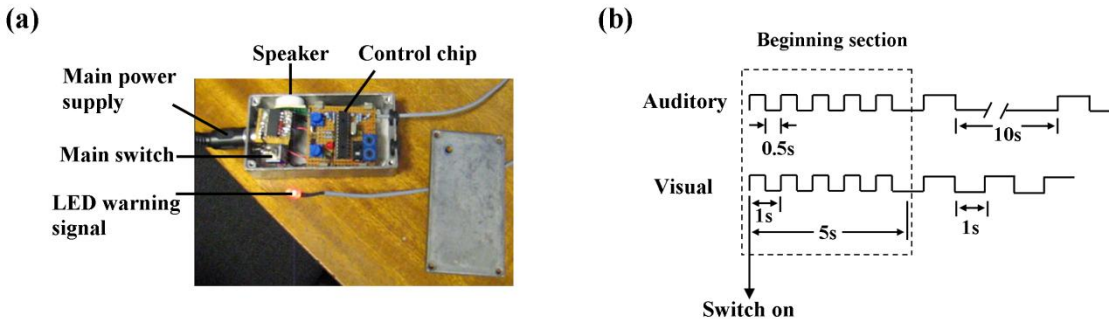

Figure 4.8 – The image of the waning system in working mode for the commercial light source (a) and the structure of the warning signal (b). In the beginning section (5 s), the visual and auditory warning signal will be triggered for 0.5s with a cycle of 1s. Then the visual warning signal will be on for 1s every other 2s, while the auditory warning signal will be triggered for 1s duration with 10s in-between break.

When turn on the main switch; both the light source and warning system will be powered. Within the first 5s (beginning section), a 0.5s long 1 kHz white noise signal will be generated every other second, synchronized with the shining of the red LED (Figure 4.8 (b)).

4.2.1.2 Camera

Within the iPPG setup, the digital camera is the most important component. Its characteristics would significantly influence the recorded images and consequently the physiological

parameters. As mentioned above, current iPPG studies could be further categorized into two aspects: webcam based low cost iPPG system [47] and experimental camera based iPPG setup [48]. The former setup typically coupled with ambient light source has been proven superior in its low cost and practicability in remote detecting some physiological parameters, e.g., heart rate [47] and respiration rate [48]. However, the main drawback of the webcam iPPG system is the image quality and frame rate. For instance, the colour webcam always encoded the image with 8 bit resolution in red, green, and blue channels. Besides, the limited frame rate (about 30 fps) could miss the important temporal information when assessing the physiological measurements like pulse transit time and pulse rate variability. The experimental camera which shows the flexibility to choose variable readout speed, sensitivity and exposure time seems to be a promising route to overcome these problems. CCD (charge-coupled device) and CMOS (complimentary metal-oxide semiconductor) camera as opto sensors have been widely used in biomedical and clinical applications. CCD camera moves photo-generated charge from pixel to pixel and convert it to voltage at an output node, while CMOS camera converts charge to voltage inside each pixel [51]. Hence, CCD cameras could create high-quality, low noise image, but consume more power and are more expensive. Compared to CCD, CMOS cameras have a comparable imaging performance whilst consuming less power. With the latest advances in opto-electronis, an upgraded CMOS camera could achieve a higher frame rate (>100 fps) with a higher sensitivity (QE>50%).

A monochrome CMOS camera (Model: Eo*Sens* MC 1360-63, Mikrotron GmbH, German) which has a maximum resolution of 1280×1024 pixels and a sample rate over 100 fps, has been employed and validated in the present study. The pixels were encoded in a 10 bit gray scale, allowing the camera to detect the weak pulsations of the microvascular tissue bed. As it can be seen in Figure 4.1, the camera was connected to a personal computer via a Camera Link® frame grabber PCI card (which will be detailed in next section). With the commercial image capture and control software (silicon-software Version 5.1, SILICON**SOFTWARE** GmbH, German), the camera can deliver quality images with flexible size, and the frame rate can reach 100 fps in full resolution and up to several thousand fps for a selected region of interest mode. A commercial F-mount zoom lens (Model: Nikkor 20 mm f/2.8D, Nikon, Japan) was adopted to couple to the camera. Depending on the lens, it was possible to focuses at arbitrary parts of tissue from a few square millimetres to several square centimetres as requested in the actual measurements. An image of the camera and the lens is presented in Figure 4.9.

Figure 4.9 – The image of the monochrome CMOS camera (model: Eo*Sens* MC 1360-63, Mikrotron GmbH, German) (Image courtesy of The Mikrotron GmbH.).

4.2.1.3 Frame grabber

Another key component in the present iPPG hardware setup is the frame-grabber. Its characteristics indirectly boundary the recorded images such as size, pixel resolution, and frame rate. For instance, the frame grabbers employed in the present study either has its own memory (1GB) or occupies the memory of the PC. As mentioned in Chapter 2, one of the challenge or drawback of the iPPG system is the inevitably larger datasets. Hence, the capacity of the frame grabber memory or the PC memory would influence the experimental protocol design, mainly a trade-off of the image size, frame rate, and recording duration. According to our experience gained from a previous feasibility study, if the physiological parameters do not requires relative high time domain resolution, e.g., heart rate/respiration rate, a medium frame rate (around 50 fps) with relative middle image size (320×240 pixels) might be enough for the measurements [50]. While if the spatial information is the key subject of research, e.g., characterization of vascular skin lesions (port wine stains), a big image size (640×480 pixels) with relative low frame rate (around 25 fps) might be suitable for the assessments [48]. In the case of pulse transit time and pulse rate variability analysis, a fast frame rate (around 100 fps) with relative large image size (640×480 pixels) and long-term recording (around 3 minutes) configuration is needed.

Specifically, the frame grabber, microEnable IV (SILICON**SOFTWARE** GmbH, German), has been employed in this study. The image and the schematic layout of the microEnable IV is presented in Figure 4.10.

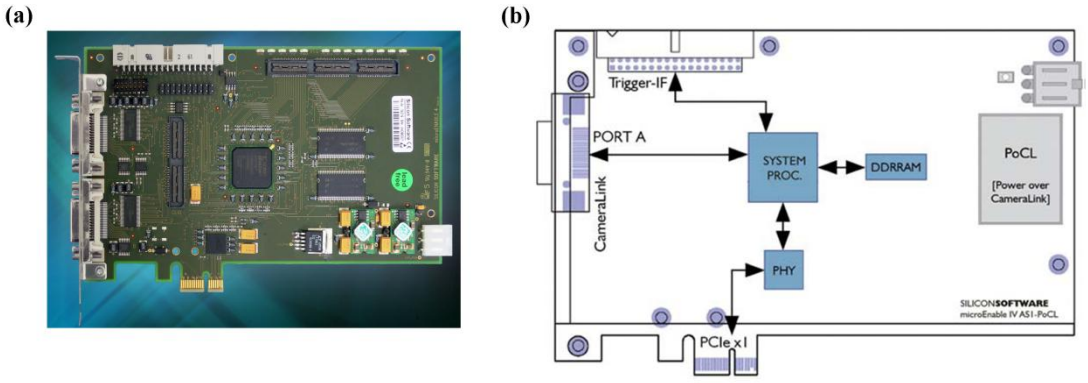

Figure 4.10 – The image (a) and the schematic layout (b) of the microEnable IV frame-grabber (image courtesy of SILICON**SOFTWARE,** GmbH, German).

The microEnable IV is a one-port frame grabber for a base configuration camera link camera. Besides powerful acquiring functions it additionally processes a high-precision trigger system for especially fulfilling requirements of line-scan camera applications. In addition it is shipped with valuable image pre-processing functions that can be run in real time without loading of the host CPU. For a monochrome camera it offers two separate pixel resolutions: 8 and 16 bit, making it possible for different applications under different situations. The most interesting feature of this frame grabber during our feasible experiments is that its real time data transferring to the RAM. Without the limit of the onboard memory capacity, it allows long duration recording (which is not 100% true, since the capacity of the recording is still limited by the PC memory) with relative high frame rate and medium image size. For instance, in our pulse rate variability study, the image configuration is set as the image size of 384×256 pixel at a frame rate of 200 fps and the duration of the video is 4 minutes. Thus, for a single measurement, the original image file size is close to 10 GB.

4.2.2 Reference LED-PPG Circuit

In order to validate the recorded iPPG signals, a reference LED-PPG system has been designed. This system consists of a hardware platform which is used to capture the reference PPG signal via a standard commercial contact PPG sensor (Model: SA30014C, Shanghai Berry Electronic Tech. Co. Ltd., Shanghai, China). The obtained cPPG signal was then transferred to a custom-built LabVIEW 8.5 (National Instruments Co., USA) software platform and served as the trigger signal to a red LED (λ=650 nm, $\Delta\lambda$=15 nm) through a DAQ (Model: USB-6008, National Instruments Co., USA). Therefore, during the recording of the images, the LED probe could be attached on the recorded area of tissue. The light intensity of the LED is actually

driven by the cPPG signal collected from the finger, thereby providing an accurate reference for the validation of the iPPG signals. A schematic diagram of the reference LED-PPG system cooperation with sensing system and an image of the reference system is presented in Figure 4.11.

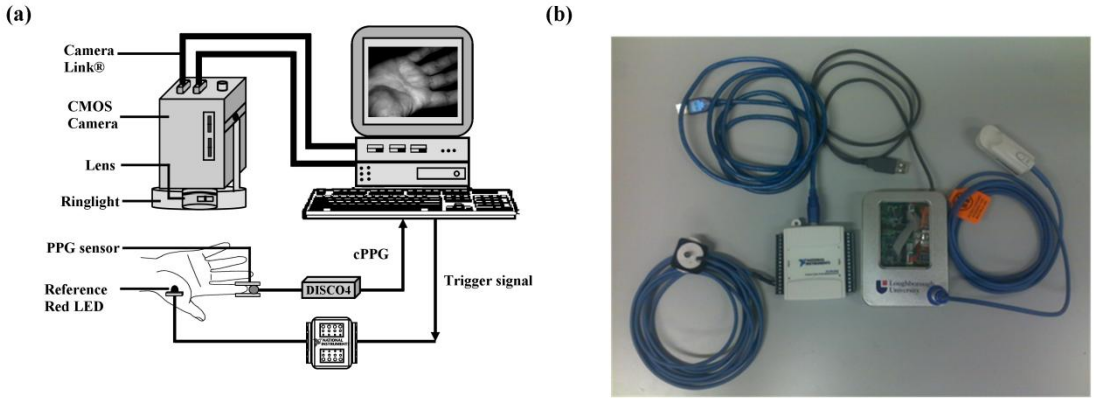

Figure 4.11 – A schematic diagram showing the reference system cooperation with the sensing system (a) and a picture of the reference LED-PPG system (b).

During the real recording, an additional usage of the reference LED-PPG system has been uncovered. The LED-PPG system could not only offer a reference signal but also provides a high contrast template for the following image registration technique. Briefly, through searching the position of the LED-PPG sensor, the motion coordinates could be obtained which would facilitate the motion artefacts attenuation. Besides, in the experiments where spatial information is essential, the standard size of the reference LED sensor (31×31 mm) presents relative accurate distance information. For instance, in the assessment of the pulse transit time (PTT), the real distance between the two windows where iPPG signals are obtained could easily recount thereby facilitating the calculation of the pulse wave velocity (PWV). One thing requires attention is that the reference cPPG signal re-obtained from the recorded images could only serve for the validation purpose and does not satisfy the accurate temporal calculation, e.g., the time delay between the iPPG signal obtained from the illuminated tissue and the reference cPPG signal is not the real time delay. This is because the duration for the cPPG signals transferring into computer and for the trigger signal generation is not defined.

4.3 ALGORITHMS & SOFTWARE

As detailed in Chapter 2, PPG signal is known to be susceptive to motion-induced signal corruption which consequently makes motion artefacts removal (or at least attenuation) one of the most challenging problems in conventional PPG signal processing. While in iPPG setup where the sensor has no contact with the skin, involuntary movements of the subject relative to the camera cannot be easily avoided, consequently introducing artefacts and leading inaccurate results. Such a drawback actually limits the physiological monitoring capabilities of the iPPG technique in real application environments, i.e., hospital, homecare, ambulance, triage, and sports performance assessment. Another inevitable limitation of iPPG is the recorded large datasets which would occupy a vast file capacity thus increase the complexity of post processing, in spite of the ability and facility for the iPPG system to obtain physiological information from a region which offers added information. For instance, in our previous feasible testing study, a sequence of monochrome frames with image size of 640×480 pixels (pixel resolution = 10 bits) and a sample frequency at 100 fps could easily occupy more than 1 GB of storage space after only 15 seconds acquisition. Also, based on our experience, different processing approaches should be carefully employed according to the desired physiological parameters and the recording situations. For instance, in exercise PPG signal processing, a motion compensation technique should be adopted before any further analysis. Last but not least, the joint time-frequency analysis, offering a potentially more revealing picture of the temporal localization of a signal's spectral components, should be adopted instead of the conventional Fourier transform which might lead to misinterpretation of the perfusion PPG signals. Hence, in this section, the software elements of the present iPPG platform are detailed, attempting to solve the aforementioned problems.

4.3.1 Image Registration

One recent iPPG study introduced a webcam based method for contact-free heart rate measurements that is automated and motion-tolerant [47]. This novel approach could be applied to colour video recordings and is based on automatic face tracking along with blind source separation. In this study, we propose an image processing technique prior to the common post PPG signal extraction approach. As detailed in Chapter 3, the motion artefacts could be considered as a modulated function. The motion artefacts attenuation problem can be theoretically solved by finding the inverse function of the motion modulated corruption function (see Equation **3.14**), and in practice consists of achieving a value close to 1 for parameter ρ in Equation **3.15**. Since motion artefacts corrupt all physiological signals

contained within a recorded frame sequence, it is reasonable to compensate the effect prior to the extraction of these signals.

4.3.1.1 Background

A frequent problem arises when images are taken, at different times, by different sensors or from different viewpoints need to be compared. The images need to be aligned with one another so that physiological information can be detected with confidence. To find the optimal match for the template in the image, the proper alignment between the image and template must be found. This problem and many related variations are solved by methods that perform image registration. Registration is a fundamental task in image process used to match two or more taken pictures. Over the years, a broad range of techniques have been developed for the various types of data and problems [78]. Specifically, within the current clinical setting, medical imaging is a vital component of a large number of applications. Registration is often necessary for (1) integrating information taken from different sensors, (2) finding changes in images taken at different times or under different conditions, *(3) inferring information from images in which either the camera or the objects in the scene have moved* and (4) for model-based object recognition [79]. To register two images, a transformation must be found so that each point in one image can be mapped to a point in the second. This mapping must 'optimally' find the similarity between two images and align the two images where optimality depends on what needs to be matched. Here, the determination of the similarity between two structured data sets (recorded images) is fundamental to the disciplines of image registration. The method most widely used for similarity detection is correlation. In fact, the similarity detection problem itself is generally called 'correlation' [80].

In the context of this thesis, image registration refers to the spatial mapping between two images. If we define these images as two 2-dimentional arrays of a given size denoted by I_1 and I_2 where $I_1(x,y)$ and $I_2(x,y)$ each map to their respective intensity values, then the mapping between images can be expressed as:

$$I_2(x,y) = g\left(I_1\big(f(x,y)\big)\right) \qquad [\mathbf{4.1}]$$

where f is a 2D spatial coordinate transformation and g is 1D intensity or radiometric transformation. Then the registration problem becomes the task involved in finding the optimal spatial and intensity transformations so that the images are matched with regard to the misregistration source. The intensity transformation is frequently not necessary [78], thereby

will not detailed in this study.

Let two images, S the *search area* and W the *window/template* be defined as shown in Figure 4.1. S is taken as an $L \times L$ array of digital picture elements which may assume one of K grey levels; i.e., $0 \leq S(i,j) \leq K-1 \ (1 \leq i,j \leq L)$. W is considered to be an $M \times M$, M smaller than L array of digital picture elements having the same grey scale range; i.e., $0 \leq W(l,m) \leq K-1 \ (1 \leq l,m \leq M)$. It will be convenient to introduce a notation for $M \times M$ wholly contained sub-images. $S_M^{i,j}(l,m) \equiv S(i+l-1, j+m-1) \quad (1 \leq l,m \leq M; 1 \leq i,j \leq L-M+1)$. Here, each $M \times M$ sub-image of S can be uniquely referenced by the specification of its upper left corner's coordinates (i,j). These will be further used to define reference points. Translational registration, therefore, is a search over some subset of the allowed range of reference points to find a point (i^*, j^*) which indicates a sub-image that is most similar to the given window.

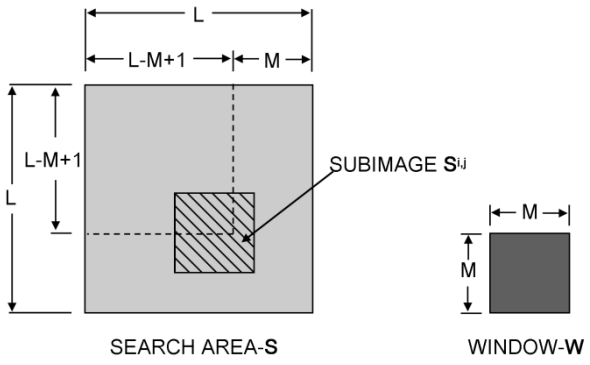

Figure 4.12 – A schematic diagram showing a complete sub-image is contained in the search area (image courtesy of [80]).

An important consideration for the selection of the registration method to be employed for a given problem is the source of mis-registration, which is the cause of the misalignment between images. Besides, the complexity of the registration method should be also carefully considered as the image sequence could be a vast amount of data from just several minutes of recording. Hence, the registration method should maintain the balance of the accuracy and complexity.

4.3.1.2 2-D Cross-correlation

As mentioned above, the method most widely used for the automatic determination of the translation is correlation. It is usually used for template matching or pattern recognition. The

elements of the un-normalized cross-correlation surface $R(i,j)$ are defined to be:

$$R(i,j) \equiv \sum_{l=1}^{M}\sum_{m=1}^{M} W(l,m)S_M^{i,j}(l,m), \qquad 1 \le i,j \le L-M+1 \qquad [\mathbf{4.2}]$$

In the correlation schema a representative output surface such as $R(i,j)$ is searched for a maximum $(\hat{\imath},\hat{\jmath})$. The procedure is successful if $(\hat{\imath},\hat{\jmath})$ and (i^*,j^*) are equivalent. As a counterexample, however, consider the un-normalised cross correlation of Equation 4.2 even in the ideal case when W exactly matches some subimage; i.e., $W = S_M^{i^*,j^*}$. Then

$$R(i^*,j^*) = \sum_{l=1}^{M}\sum_{m=1}^{M} W^2(l,m) \qquad [\mathbf{4.3}]$$

Also, for this ideal case, consider the non-matching point $(\hat{\imath},\hat{\jmath})$ where $S_M^{\hat{\imath},\hat{\jmath}}(l,m) = max_{l,m}W(l,m) = W_M$, for all (l,m). Clearly

$$R(\hat{\imath},\hat{\jmath}) = W_M \sum_{l=1}^{M}\sum_{m=1}^{M} \qquad W(l,m) \ge R(i^*,j^*) \qquad [\mathbf{4.4}]$$

Hence, a search for a maximum over $R(i,j)$ does not necessarily yield the registration point even in the ideal case [80]. Normalization is therefore necessary in even the simplest of cases. The 2-dimensional normalized cross-correlation function measures the similarity for each translation could then be obtained:

$$R_N(i,j) = \frac{\sum_l \sum_m W(l,m)S_M^{i,j}(l,m)}{\sqrt{\sum_l \sum_m (W(l,m))^2 \sum_l \sum_m \left(S_M^{i,j}(l,m)\right)^2}} \qquad [\mathbf{4.5}]$$

If the window/template matches the image exactly, except for an intensity scale factor, at a translation of (i,j), the cross-correlation will have its peak at $R_N(i,j)$. Thus by computing R over all possible translations in search area, it is possible to find the degree of similarity for any template-size window in the image [78]. Template matching using correlation has many variations. If the allowable transformations include rotation or scale, for example, multiple templates can be used. As the number of templates grows, however, the computational costs can quickly become unmanageable, i.e., the approximate number of calculations for ordinary normalized cross-correlation includes $L^2 + M^2$ (Multiplications), $M^2(L-M+1)^2$ (Adds), and $(L-M+1)^2$ (Multiplications & Divides) [77]. Therefore, smaller local features of the

template which are more invariant to shape and scale, such as edges, are often used. In the present study, a manually chosen template with high contrast compared to the rest image was initially chosen. Then, through searching the peak similarity along the frame sequence and re-aligning the image, the planar motion artefacts could be attenuated.

4.3.2 Image Segmentation

The measured conventional PPG waveform comprises a pulsatile ('AC') physiological waveform, attributing to cardiac synchronous changes in the blood volume with each heart beat, which is superimposed on a slowly varying quasi-static ('DC') baseline with various lower frequency components. Observation of measured intensity indicates that the AC components accounts for only a few small proportion of the total intensity. To detect this weak arterial pulsation, the pixel resolution in an iPPG setup should be at least 8 bits or above (10 bits in the present study). Inevitably, this configuration triggers a main drawback of the iPPG technique, e.g., larger datasets, and particularly increases the difficulties for the post processing. Besides, it left a trade-off between frame rate and recording duration. A fast sample rate would result in short recordings, and vice versa, which requires careful design of the experiment protocol. This will be detailed in the next chapter. To overcome the problem of large dataset handling and save the effort in iPPG signal post processing, one attempt has been made to segment the image and save as a sequence of data. A schematic diagram of the present image segmentation technique is presented in Figure 4.2.

After a video has been recorded and re-aligned, the image segmentation technique is conducted, resulting in sets of same length segmented frames. The spatial resolution decreases with each step of averaging; such an averaging procedure has been shown to improve the signal to noise ratio [48]. As presented in Chapter 3, an ideal motion artefact attenuation technique would completely remove all corruption due to motion, thus yielding the theoretical maximum point in the motion modulated function (Equation **3.16**). As this is not achievable in practice, a simple methodology to further attenuate motion artefacts after image registration is to average the signals within a window, which comes at the expense of spatial resolution.

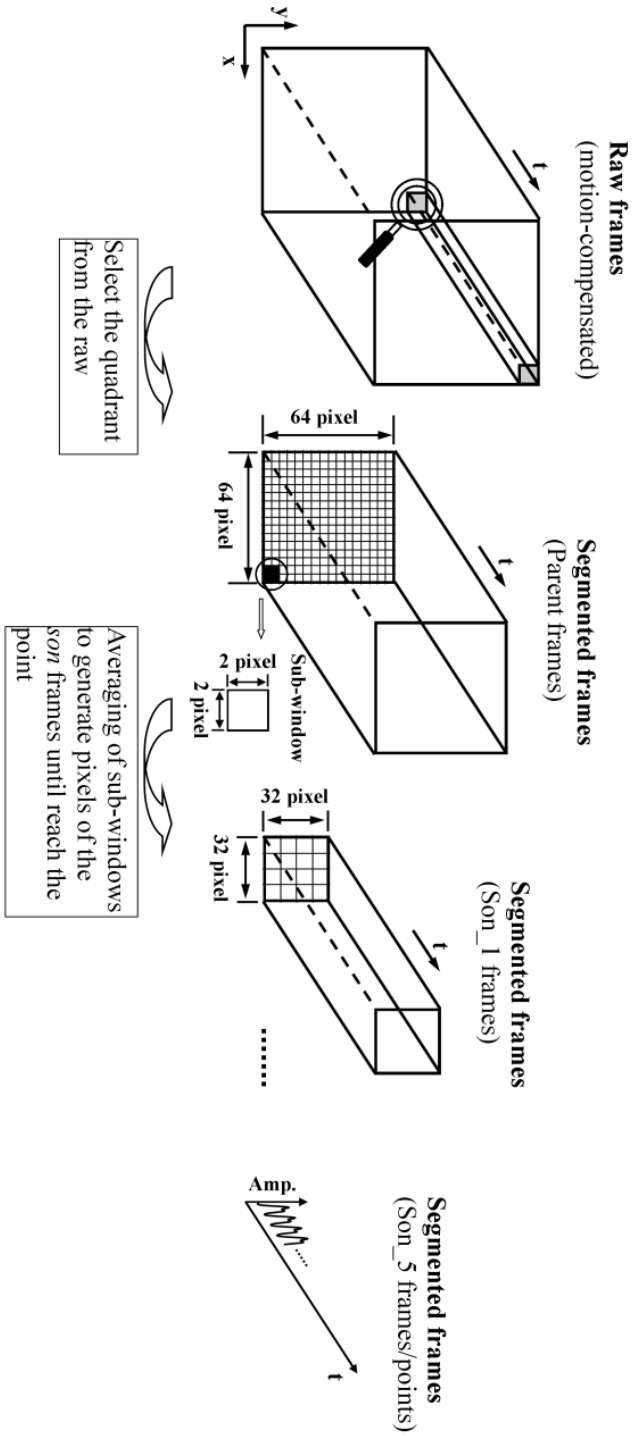

Figure 4.13 – A schematic diagram showing the image segmentation technique. Specifically, after a sequence of raw frames have been recorded, the motion compensation technique has been initially employed, then one quadrant (parent frames) with the size of 64×64 pixels is selected and saved with the name indicating its position in the original frame (the upper left corner's coordinates (i, j)). A sub-window is then chosen to shrink the image through averaging. In the present study, a 2×2 pixels window is served as the sub-window. A new set of frames with the same duration (son frames) could be obtained and saved accordingly. Such an approach is conducted until reach the point frame. All the frames with the same parent were saved in the same folder.

However, in some applications spatial information is needed, e.g., the characterization of vascular skin lesions. Our method could recall the different parent level segmented frames and acquire the spatial details. Based on our experience, the novel segmentation technique could save the time and effort in handling the original data set while maintaining the spatial information for various applications. The only drawback of this image segmentation approach, to the best of our knowledge, is the filling-up of storage space in the hard disk. For example, compared to the raw frames, nearly twice the storage space would be taken after the whole sets of segmented frames have been obtained.

4.3.3 Blind Source Separation

PPG is susceptible to motion-induced signal corruption, making motion artefact removal or attenuation one of the most challenging issues in iPPG signal processing. However, in recent pioneering works, motion artefacts were not carefully dealt with and the associated iPPG setups were usually operated under conditions that required the subjects to be motionless [46, 48, 49, 52]. This drawback limits the physiological monitoring capabilities of the technique in the real application environments, i.e., hospital, homecare, and sports assessment. In recent years, several methods, such as blind source separation (independent component analysis (ICA) (for a review, see [81]), single channel ICA (SCICA) [58, 82, 83]) and Least-Mean-Square adaptive filtering [56], have been proposed for removal of noise from biomedical signals. Specifically, for iPPG application, Poh and colleagues have introduced a web camera based iPPG setup as well as a motion attenuation technique relying on ICA, which shows a promising route for remote cardiovascular assessment [47]. Specifically, once the video has been obtained, an automatic face tracking technique (image registration) has been adopted prior to the ICA of multichannel signals, i.e., R, G, & B colour signals into independent components. The physiological parameters could then be extracted from these independent components. This pioneering research attempts an alternative approach to compensate for motion for a more effective extraction of physiological variables. Hence in this section, the blind source separation techniques, e.g., ICA & SCICA, would be detailed.

4.3.3.1 Independent component analysis (ICA)

Actually, a central problem in neural-network research, as well as in statistics and signal processing, is finding a suitable representation or transformation of the data. For computational and conceptual simplicity, the representation is often sought as a linear transformation of the original data. For instance, let us denote by $x = (x_1, x_2, \dots, x_m)^T$ a zero-mean m-dimensional

random variable that can be observed, and by $s = (s_1, s_2, \dots, s_n)^T$ its n-dimensional transform. Then the problem is to determine a constant (weight) matrix W so that the linear transformation of the observed variables $s = \mathrm{W}x$ has some suitable properties. The basic goal of independent component analysis (ICA), as the name implies, in determining the transformation is to find a representation in which the transformed components s_i are statistically as independent from each other as possible [84]. Two promising applications of ICA are blind source separation and feature extraction.

One popular way of formulating the ICA problem is to consider the estimation of the following generative model for the data:

$$\boldsymbol{x} = \mathrm{A}\boldsymbol{s} \qquad [\mathbf{4.6}]$$

where $\boldsymbol{x}$ is an observed m-dimensional vector, $\boldsymbol{s}$ is an n-dimensional (latent) random vector whose components are assumed mutually independent, and A is a constant $m \times n$ matrix to be estimated which is unknown but invertible. It is usually further assumed that the dimensions of $\boldsymbol{x}$ and $\boldsymbol{s}$ are equal, i.e., $m = n$. Hence, the observed signal $\boldsymbol{x}$ are assumed to be a linear mixture of an equal number of unknown yet statistically independent source signals $\boldsymbol{s}$. Then the problem is solvable up to a permutation, sign and power indeterminacy of the sources, through finding an appropriate de-mixing matrix, a (pseudo)inverse of the estimate of the mixing matrix: $\mathrm{W} = \mathrm{A}^{-1}$, which allows estimation of the source waveforms by $s = \mathrm{W}x$. Here, non-Gaussianity of the independent components is necessary for the identifiability of the Equation 4.6 [81].

Based on the concept of mutual information, Comon showed how to obtain a more general formulation for ICA that does not need to assume an underlying data model [81]. Here, mutual information, an information-theoretic-measure, is a natural measure of the dependence between random variables which could be employed as the criterion for finding the ICA transform. Actually, the ICA of a random vector $\boldsymbol{x}$ has an invertible transformation $\mathbf{s} = \mathrm{W}\boldsymbol{x}$ where the matrix W is determined so that the mutual information of the transformed components s_i is minimized. It is particularly interesting in practical to express mutual information using negentropy, constraining the variables to be uncorrelated. The definition of negentropy J is given by:

$$J(\mathbf{y}) = H(\mathbf{y}_{\mathbf{gauss}}) - H(\mathbf{y}) \qquad [\mathbf{4.7}]$$

where $\mathbf{y}_{\mathbf{gauss}}$ is a Gaussian random variable of the same covariance matrix as $\mathbf{y}$, and $H(\mathbf{y})$ is

the differential entropy of a random vector $\mathbf{y} = (y_1, \dots, y_n)^T$:

$$H(\mathbf{y}) = -\int f(\mathbf{y}) \log f(\mathbf{y}) d\mathbf{y} \qquad [\mathbf{4.8}]$$

where $f(\cdot)$ is the density of $\mathbf{y}$ [85]. Using the concept of differential entropy, one can define the mutual information I between the n (scalar) random variables $y_i, i = 1, \dots, n$:

$$I(y_1, y_2, \dots, y_n) = J(\mathbf{y}) - \sum J(y_i) \qquad [\mathbf{4.9}]$$

In practice, ICA algorithm can be derived based on different theoretic techniques, among which, FastICA is the most popular and referenced ICA techniques (for a review, see [86]). The idea is to use the fast fixed-point iterative algorithm to find the local extreme of the kurtosis of the linear observed variables.

The use of this fairly new technique in biomedical signal analysis is growing [87], e.g., in noise removal from electrocardiogram (ECG) [88], electroencephalogram (EEG) [89], PPG recordings [57], separation of foetal and maternal ECGs recorded simultaneously [90], as well as detection of event related regions of activity in functional magnetic resonance imaging (fMRI) experiments [91]. One recent study reports attempts to attenuate the motion artefacts from iPPG signals via ICA by considering motion as an additive component [47]. Specifically, by recording a video of the facial region with a webcam, the RGB colour sensors pick up a mixture of the reflected plethysmographic signal along with other sources of fluctuations in light due to artefacts such as motion and changes in ambient lighting conditions. Given that haemoglobin absorptivity differs across the visible and near-infrared spectral range, each colour sensor records the sum of the original source signals with slightly different weights. These observed signals from the red, blue, and green colour sensors are the I'_{det} as described in Equation $\mathbf{3.13}$. A schematic diagram of the application is demonstrated in Figure 4.14. The idea proposed in this pioneering research has been employed for noise attenuation prior to the effective physiological assessments performed in this study.

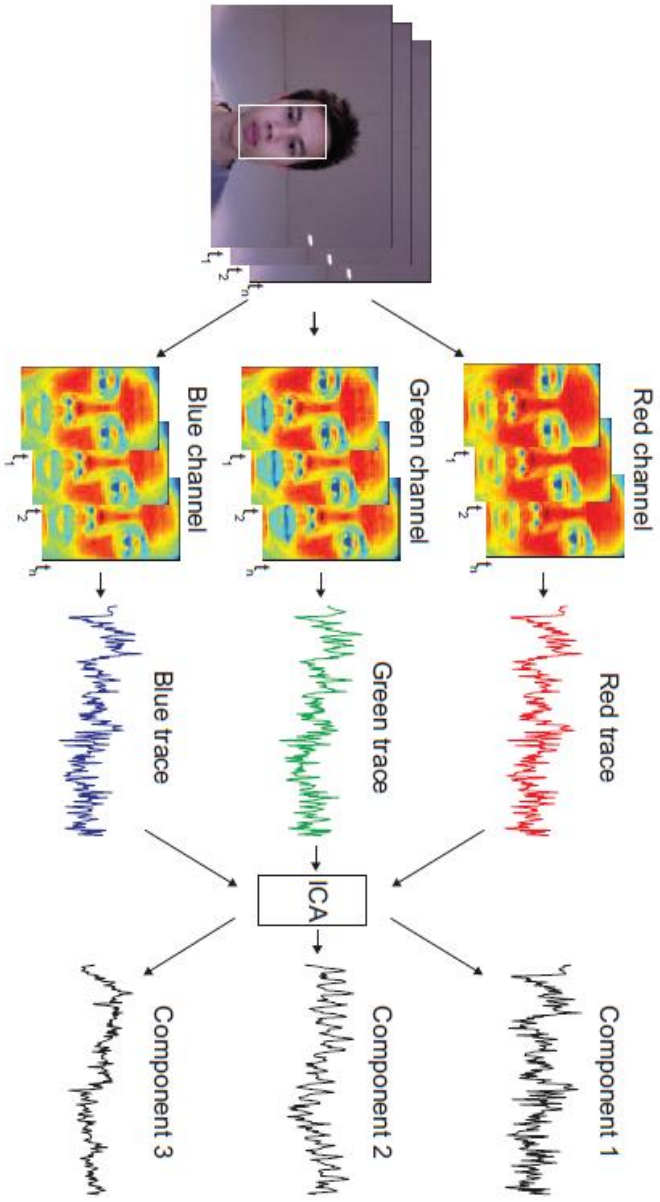

Figure 4.14 – A schematic diagram of cardiac pulse recovery methodology in iPPG signal processing (image courtesy of [47]).

4.3.3.2 Single channel ICA (SCICA)

In many ICA based bio-signal analysis problems, it is commonly assumed that the conventional ICA algorithm could only be applied to spatial or multichannel information. However, when the signal of interest is only present in one or very few channels of a multi-channel recording, or when only a single channel of recording is available (in the present study, imaging PPG videos were recorded via a monochrome digital camera), the difficulty of isolating signals of interest is dramatically increased. Many methods attempt to isolate such activity, using mimetic methods

or broadband filtering methods to remove (or at least attenuate) those undesired components in the recordings. However, the results were barely satisfied. Recent research has been published to propose a new technique in breaking down single channel recordings of the electromagnetic brain signals into their underlying components, irrespective of the components' origin (physiological or otherwise) [58, 82, 83]. The method relies on a combination of a non-linear dynamical systems framework and a standard implementation of independent component analysis, which stimulates us to extract the physiological parameters from the signal channel iPPG channels.

Specifically, given a sampled time series (e.g., I'_{det} (Equation $\mathbf{3.13}$)), within a dynamical systems viewpoint, SCICA attempt to uncover as much information as possible about the underlying generators based only on the measured data. This could be accomplished through a technique known as dynamical embedding (DE). The assumption that the measured signal is due to the non-linear interaction of just a few degrees of freedom, with additive noise, suggests the existence of an unobserved deterministic generator of the observed data [83]. If the number of degrees of freedom of the underlying system is given by D, then D can be used as a coarse measure of the system complexity. Takens' theorem [92] allows the reconstruction of the unknown dynamical system that generated the measured time series by reconstructing a new state space based on successive observations of the time series. One common approach to constructing a DE matrix is from a series of delay vectors taken from the observed data $x(t)$, say, where the state of the unobservable system at time t, $X(t)$, is given by:

$$X(t) = \{x(t-\tau), x(t-2\tau), \dots, x(t-(m-1)\tau)\} \in \Re \qquad [\mathbf{4.10}]$$

where τ is the lag and m is the number of lags or the embedding dimension. This delay vector describes observations of the underlying system states, assuming that the data, $x(t)$, $t = 1,2,\dots,N$, are generated by a finite dimensional, non-linear system of the form:

$$x(t) = f[X(t-1), X(t-2), \dots, X(t-D)] + e_t \qquad [\mathbf{4.11}]$$

where $x(t)$ is real valued, and e_t is independently and identically distributed, and zero-mean with unit variance. As mentioned above, SCICA is a method to isolate multiple components using only the temporal information inherent in a single channel recording. Therefore, we need to obtain a 'multi-channel' data representation of the single data channel. This can be achieved through generating a series of consecutive delay vectors as described in Equation 4.10 to form a matrix of delays (also known as embedding matrix):

$$\boldsymbol{X} = \begin{bmatrix} x_t & x_{t+\tau} & \cdots & x_{t+N\tau} \\ \vdots & \ddots & & \vdots \\ x_{t+(m-1)\tau} & x_{t+m\tau} & \cdots & x_{t+(m+N-1)\tau} \end{bmatrix} \quad [\mathbf{4.12}]$$

where τ is the lag term, m is the dimension of the constructed matrix and N is the length of the matrix [55, 79, 80]. Here, the delay dimension should be large enough to capture the necessary information content. Takens showed that the Euclidean embedding dimension $\hat{m}$ must be at least as large as D (degrees of freedom), but in practice must be such that: $\hat{m} > 2D + 1$. When applied to real world data the delay vector size m actually used needs to be significantly larger than the Euclidean embedding dimension ($\hat{m}$) because of dependencies in the time series data and inherent noise in the system. According to [83], the practical minimum size for m could be determined based on the sample frequency (f_s), lowest frequency of interest (f_L) and the lag τ, i.e., $m \geq f_s/f_L$, for $\tau = 1$. The length of delay vectors N, is determined by the length of the signal to be analyzed but in practice must be at least as large as m. If N is set such that the embedding matrix covers a quasi-stationary signal, it becomes possible to extract an estimate for the unobserved degrees of freedom D. Moreover, if the choice of lag term τ, delay vector size m and number of lag vectors N is adequate, the embedding matrix is now rich in information about the temporal structure of the measured data. Figure 4.4 gives a diagrammatical representation of the embedding process and what it represents in terms of the recorded signals.

Upon the construction of the delay matrix, the conventional ICA is applied to decompose the delay matrix into a series of independent components (ICs). Once a subset of ICs (assuming dimension is p, where $p \leq m$) has been chosen, the resulting embedding matrix B^i in the measurement space can be calculated as $B^i = a_i s_i^T$, where s_i is the i^{th} IC ($i = 1,2, \dots, p$) and a_i is the corresponding column of the mixing matrix A. The projected time series $b_i(t)$ can then be obtained by averaging the rows of B^i [58, 83]:

$$b_i(t) = \frac{1}{m}\sum_{k=1}^{m} B^i_{k,t+k-1} \qquad (t = 1,2, \dots, N) \quad [\mathbf{4.13}]$$

Here, $B^i_{k,t+k-1}$ is the element of the matrix B^i.

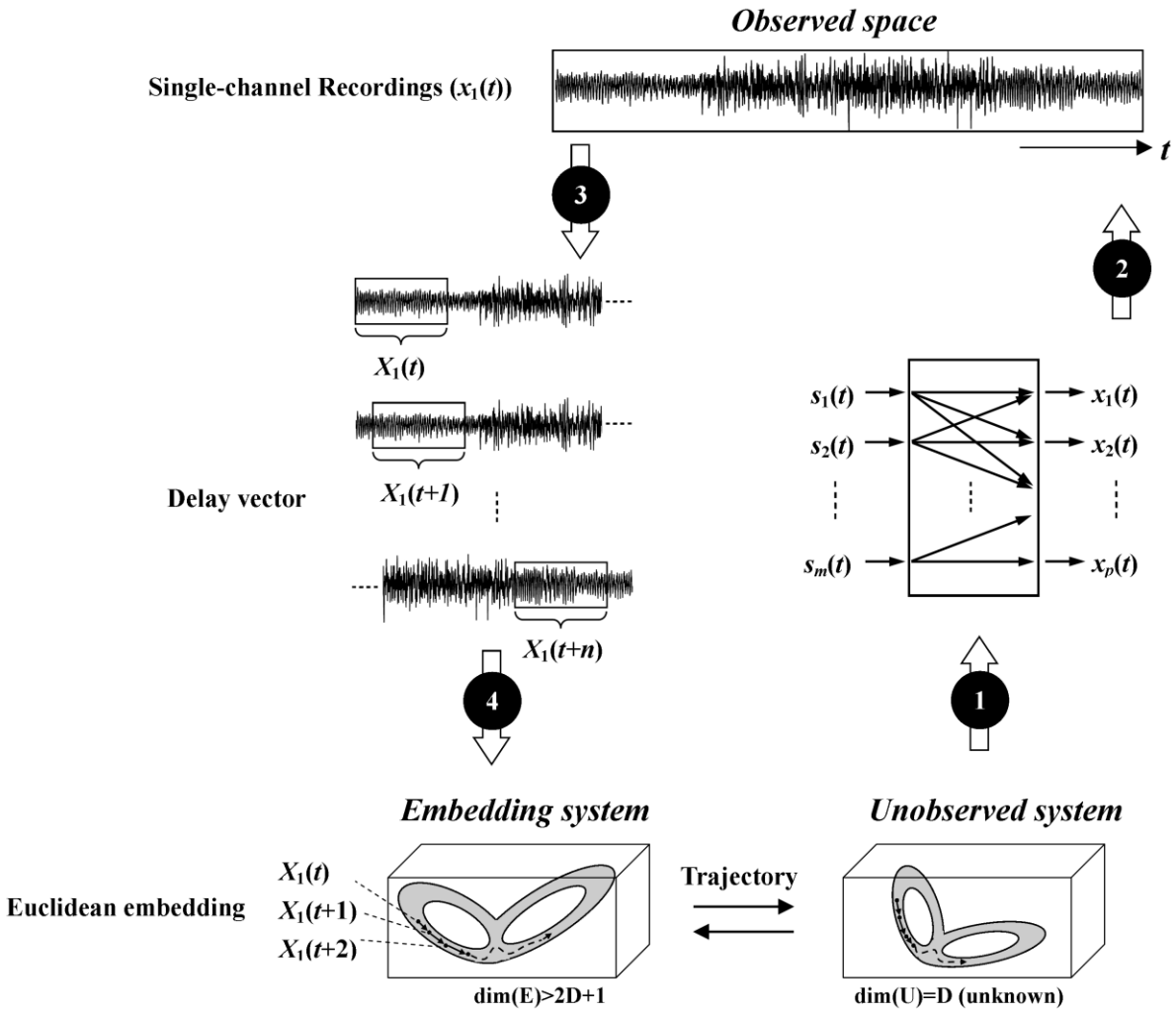

Figure 4.15 – A theoretical schematic diagram of single channel independent component analysis (SCICA) and its underlying principle. (1) Sources generate data that lies on an unobservable system manifold U of dimension D which is unknown; (2) the recorded signals are assumed to be generated by a mixing system with a few degrees of freedom; (3) data from a single measurement channel constitutes the measurement space from which consecutive delay vectors are extracted; (4) delay vectors form an embedding matrix that traces a trajectory on the manifold generated by the Euclidean embedding.

4.3.4 Time-Frequency Representation

Fourier Transform (FT) which offers a passage from the time domain to the frequency domain is widely applied in conventional PPG signal processing as it can provide the fundamental information such as heart rate and respiration rate (the peak frequency at certain region) [52, 53, 56]. However, it assumes that signals are steady-state when physiological signals are transient in nature. Actually, Hulsbusch and colleagues have already shown that the uncritical use of the FT could lead to misinterpretation of perfusion PPG signals [46]. To obtain a potentially more revealing picture of the temporal localization of a signal's spectral components, one has to

resort to the joint time-frequency analysis, e.g., time-frequency representation (TFR). The TFR approach converts a one-dimensional time signal into a two dimensional function of time and frequency so that frequency components can be localized with a temporal resolution [20].

4.3.4.1 Purpose of TFR analysis in PPG signals processing

As mentioned above, Fourier transform (FT) does not allow a combination of time and frequency domain while, in practice, most time information is not easily assessable in frequency domain. The spectrum $X(f)$ obtained from FT only shows the overall strength with which any frequency f is contained in the signal $x(t)$, it does not generally provide easy-to-interpret information about the time localization of spectral components (strictly speaking, this information is contained in the phase spectrum $\arg[X(f)]$ but often comes in a form that is not easily interpreted). Therefore, conventional FT analysis could lead to ambiguous results since it is only specified for stationary data.

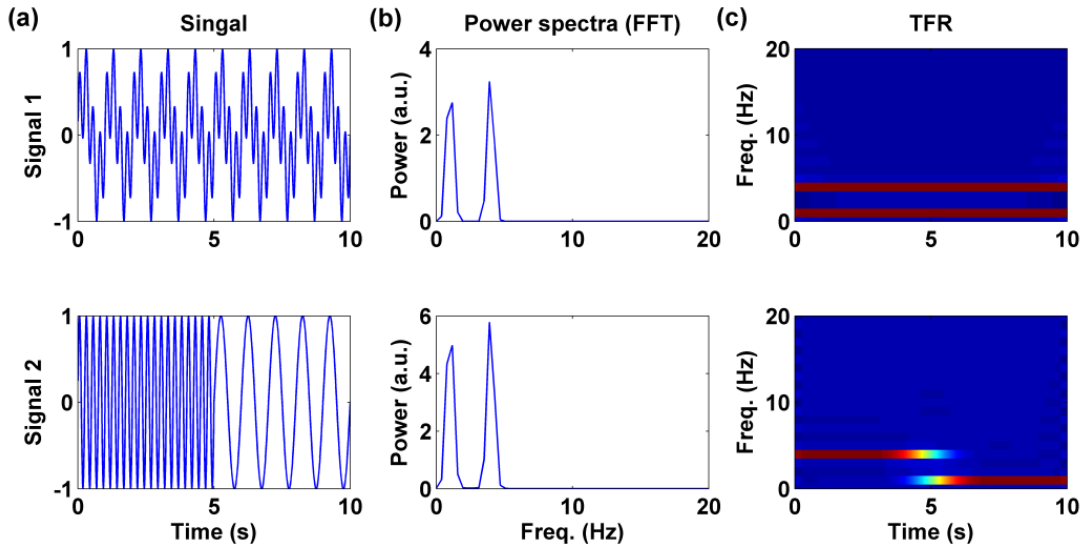

Figure 4.16 – Two model signals with their Fourier Transform power spectra and TFRs. (a) *Signal 1* contains two frequency signals (1 Hz & 4 Hz) while the first 5 seconds of *Signal 2* is the same 4 Hz signal and the last 5 seconds is 1 Hz signal. As it can be seen from the power spectra density map (b), the FT does not reflect the fundamental differences of the two signals. Without the additional phase spectrum it is impossible to determine if and when the switching process occurred in *Signal 2*. The transient variation in *Signal 2* at about 5 s is clearly demonstrated in the TFR spectra (c).

Figure 4.5(b) demonstrates a typical example of two different signals which results in nearly identical power spectra obtained by FT. Therefore, a joint time-frequency analysis technique is needed. Actually, the principle of TFR is to extract the energy distribution on a time versus

frequency plane and the values of the TFR surface give an indication as to which spectral components are present at which time and how they change in time. It can be observed that the TFR disclose the different characteristics of the two test signals (Figure 4.5(c)).

4.3.4.2 Principles of TFR

One fundamental property of each TFR, $Tx(t,f)$, corresponds to the manner in which it depends upon the signal $x(t)$. This dependence could be linear, quadratic, or otherwise nonlinear, with the first two cases being by far the most widely used and would be detailed in this thesis.

a) Linear TFRs

All linear TFRs satisfy the superposition or linearly principle which states that if $x(t)$ is a linear combination of some signal components, then the TFR of $x(t)$ is the same linear combination of the TFRs of each of the signal components. Two linear TFRs of basic importance are the short-time Fourier transform (STFT) and wavelet transform (WT).

Short-time Fourier transform (STFT): Although the FT (spectrum) does not explicitly show the time localization of frequency components, such the time localization can be obtained by suitable pre-windowing the signal. Hence, instead of processing the entire signal at once, STFT takes the FT on a block by block basis. Therefore, the resulting FT can then be thought of as a signal's frequency behaviour during the time period covered by the data block:

$$STFT(t,f) = \int x(t')\gamma^*(t'-t)e^{-j\omega t}dt' \qquad [\mathbf{4.13}]$$

when the analysis window function $\gamma(t)$ balances the time and frequency resolution. Obviously, the smaller the time duration of $\gamma(t)$, the better the time resolution. The blocks could be overlapped or disjointed and the percentage of overlap between each block is determined by the time sampling step and the length of the analysis window function $\gamma(t)$ (for a review, see [20, 93]). A schematic representation of STFT is presented in Figure 4.6.

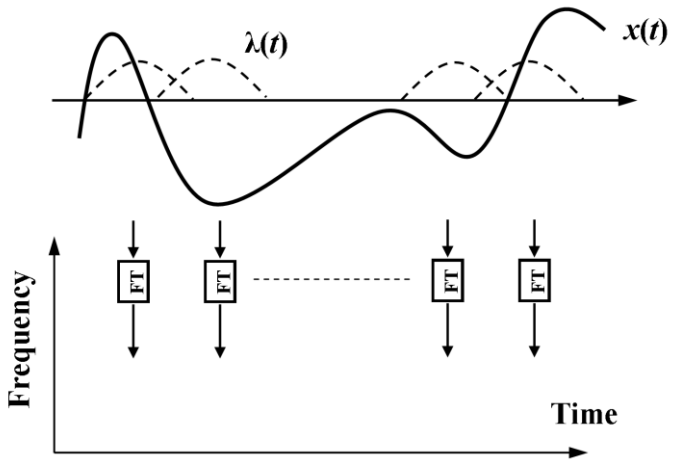

Figure 4.17 – Schematic representation of STFT (image courtesy of [93]).

Unfortunately, the uncertainty principle prohibits the existence of windows with arbitrarily small duration and arbitrarily small bandwidth [20]. Hence, the joint time-frequency resolution of the STFT is inherently limited. Specifically, there exists a fundamental resolution trade-off: improving the time resolution (by using a short window) results in a loss of frequency resolution, and vice versa. For its simplicity and ease of implementation, STFT has already been employed in iPPG signal processing. For instance, Verkruysse and colleagues have utilized STFT to extract the time-varying heart/respiration rate [48]. The plethysmographic information is better present in the joint time-frequency diagrams.

Wavelet transform (WT): As another important linear TFR, WT defined as:

$$WT_x^{(\gamma)}(t,f) = \int_{t'} x(t') \sqrt{\left|\frac{f}{f_0}\right|} \gamma^*\left(\frac{f}{f_0}(t'-t)\right) dt' \qquad [\mathbf{4.14}]$$

where $\gamma(t)$ (the 'analyzing wavelet') is a real or a complex bandpass function cantered around $t = 0$ in the time domain. The parameter f_0 used in the Equation 4.14 equals the centre frequency of $\gamma(t)$. We note that the WT was originally introduced as a time-scale representation; this classical formulation of the WT can be re-obtained from the above time-frequency formulation by introducing the analysis scale a as f_0/f. For the time-frequency version, we have to assume that the FT of $\gamma(t)$ is essentially concentrated around the centre frequency f_0. Since its conception, various uses of the WT analysis in medicine and biology has been introduced (for a review, see [94]). With the help of WT, Hulsbusch and colleagues have shown a potentially more revealing picture of the temporal

localization of the iPPG signal's spectral components [46]. More importantly, based on this finding, they have indicated that the uncritical use of the FT could lead to misinterpretation of the perfusion PPG signals [46].

b) Quadratic TFRs

Although the linear TFR has some desirable properties, the quadratic structure of the TFR is an intuitively reasonable assumption when a TFR is interpreted as a time-frequency energy distribution, since energy is a quadratic signal representation. Differ from the linear TFRs, the spectrogram of the sum of two signals, i.e., $x_1(t) + x_2(t)$, is not simply the sum of the individual spectrograms. Hence, the linearity structure of the STFT is violated in the quadratic spectrogram. In fact, any quadratic TFR satisfies the quadratic superposition principle, i.e., for signal $x(t) = c_1 x_1(t) + c_2 x_2(t)$, its TFR follows:

$$T_x(t,f) = |c_1|^2 T_{x_1}(t,f) + |c_2|^2 T_{x_2}(t,f) + c_1 c_2^* T_{x_1,x_2}(t,f) + c_2 c_1^* T_{x_2,x_1}(t,f) \qquad [\mathbf{4.15}]$$

where $T_x(t,f)$ is the auto-TFR of the signal $x(t)$ and $T_{x_1,x_2}(t,f)$ is the cross-TFR of the two signals $x_1(t)$ and $x_2(t)$ with $T_{x,x}(t,f) = T_x(t,f)$.

Among all the quadratic TFRs with energetic interpretation, the Wigner distribution (also called Wigner-Ville distribution) gains a lot of interest due to its exceptionally large number of desirable mathematical properties [20]. For example, the auto-Wigner distribution (WD) is always real-valued, and the WD preserves time shifts and frequency shifts of the signal. Besides, the WD satisfies the marginal properties what is the frequency or time integrals of the WD correspond to the signal's instantaneous power and its spectral energy density [20]. Hence, the WD could be loosely interpreted as a two-dimensional distribution of signal energy over the time-frequency plane. The WD is defined as:

$$W_{x,y}(t,f) = \int_{\tau} x\left(t + \frac{\tau}{2}\right) y^*\left(t - \frac{\tau}{2}\right) e^{-j2\pi f\tau} d\tau = \int_{\nu} X\left(f + \frac{\nu}{2}\right) Y\left(f - \frac{\nu}{2}\right) e^{j2\pi t\nu} d\nu \quad [\mathbf{4.16}]$$

Even though the WD is theoretically attractive due to its mathematical properties, practical application of the WD is often restricted by the occurrence of interference terms. When there is more than one component in the input signal, an interference/cross term occurs which reflects the correlation of the two signal components [93]. Because interference terms are oscillatory, they may be attenuated by means of a smoothing operation. Among the smoothing operations, smoothed pseudo-WD (SPWD) has been proven to be superior for its individual time &

frequency domain resolution. Basically, SPWD allows the smoothing spreads, Δt and Δf, to be adjusted freely and independently of each other, via a separable smoothing kernel $\Psi_{SPWD}(t,f) = g(t)H(f)$:

$$SPWD_x^{(g,H)}(t,f) = \int_{t'} \int_{f'} g(t-t')H(f-f')W_x(t',f')dt'df' \qquad [\mathbf{4.17}]$$

Where $W_x(t,f) = \int_\tau x\left(t+\frac{\tau}{2}\right)x^*\left(t-\frac{\tau}{2}\right)e^{-j2\pi f\tau}d\tau$, $x(t)$ and $x^*(t)$ are the signal and its complex conjugate respectively, $g(t)$ and $H(f)$ are two smoothing windows whose effective lengths independently determine the time smoothing spread Δt and the frequency smoothing spread Δf. The separable structure $\Psi_{SPWD}(t,f)$ (i.e., $\Psi_{SPWD}(t,f)$ is the product of two separate one-dimensional windows) yields significant practical advantages for the SPWD. Specifically, the fact that time smoothing and frequency smoothing are decoupled results in great flexibility in the choice of the time smoothing and frequency smoothing, ease of application, and efficient computation [93]. An example of the SPWD is demonstrated in Figure 4.5(c).

Based upon our experience in PPG signal processing, Kaiser-Bessel function is adopted as both the time and frequency smoothing window. The N-sample discrete Kaiser-Bessel function $w(k)$ is nonzero only in the interval $[-(N-1)/2, (N-1)/2]$:

$$w(k) = J_0\left(j3\pi\sqrt{1-\frac{k}{N}}/real\big(J_0(j3\pi)\big)\right) \qquad [\mathbf{4.18}]$$

where $J_0(Z)$ is the 0-order Bessel function of the first kind:

$$J_0(x) = \sum_{m=0}^{\infty}\frac{(-1)^m}{m!\,\Gamma(m+1)}\left(\frac{1}{2}x\right)^{2m} \qquad [\mathbf{4.19}]$$

where $\Gamma(z)$ is the Gamma function, a generalization of the factorial function to non-integer values.

Originating from the Wigner-Ville distribution (WVD), SPWVD has advantage of good time and frequency resolution yet minimizes the main drawback of WVD, i.e., crossterm interference (for a review, see [20, 93]); making it a suitable technique in the present application. In this study, the TFR of the PPG signals was obtained through the Matlab (MathWorks, Inc., CA) time-frequency toolbox (TFTB) [95], which provides the majority of

approaches and programs for TFR estimation, including the basic SFTF and quadratic Cohen class TFR.

4.3.5 Analysis of HRV/PRV

As mentioned in Chapter 2, heart rate variability is a mirror of the cardiorespiratory control system and a valuable tool to investigate the sympathetic and parasympathetic function of the autonomic nervous system. Since there are indications in the literature that pulse rate variability (PRV) could be a potential surrogate of HRV, it is reasonable to adopt the existing HRV estimation and evaluation techniques. This section details the main HRV analysis methods which could be further employed for analysis of PRV. In contrast to heart rate and respiration rate calculations, after the recording of the images, a sequence of approaches have been employed to process the iPPG signals for PRV analysis. Specifically, some signal processing techniques have been adopted, e.g., interpolation and re-sampling. Actually according to the guild-lines established by the Task Force of the European Society of Cardiology (ESC) and the North American Society of Pacing and Electrophysiology (NASPE) for HRV analysis [31], the following strategy has been introduced for the PRV analysis (Figure 4.7) in the present study.

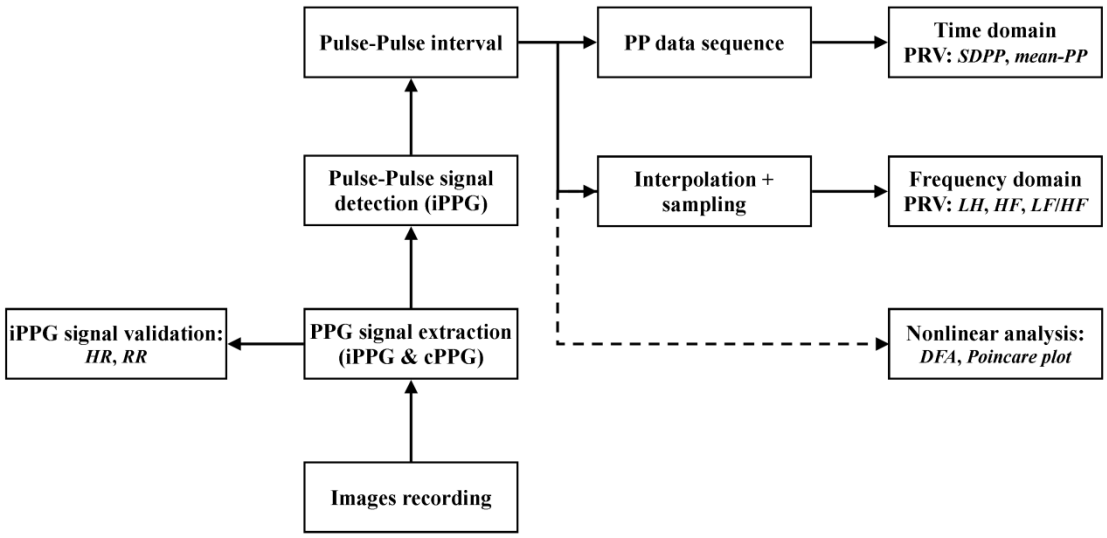

Figure 4.18 – Flow chart summarizing individual steps used when recording and processing the iPPG signal in order to obtain data for PRV analysis in the present study.

Specifically, after a series of images have been recorded, a spatial averaging technique has been employed to extract the iPPG and cPPG signals (which are obtained from the reference LED (Fig. 4.11)). A statistical analysis has been adopted to validate the iPPG signals, where only those without significant differences compared to the reference cPPG signals could be used for

the PRV analysis. A custom-built trough detection algorithm was then employed to calculate the pulse-pulse interval series, which could be further analyzed via time, frequency domain and nonlinear processing techniques.

4.3.5.1 Trough detection

In order to analyze pulse rate variability signals, the first step is to detect the pulse-pulse intervals (PPI). Compared to the various techniques for QRS detection in HRV analysis (for a review, see [96]), e.g., nonlinear filtering with thresholding, artificial intelligence using hidden Markov models, time-recursive prediction techniques, and wavelet based transforms, there are fewer techniques regarding the characterization of PRV signals. Therefore, in the present study, a revised wavelet-transform based technique has been introduced for trough detection in PPG signal processing. Differing from ECG waveforms (P, Q, R, S, & T wave), PPG signals have clear troughs (corresponding to the end-systolic) and peaks (corresponding to end-diastolic). In the present study, PPI was calculated using the time interval between the two successive PPG troughs, where the PPG signal was flat and contained little disturbance leading to erroneous determination. The PPI extraction approaches were presented in Figure 4.8.

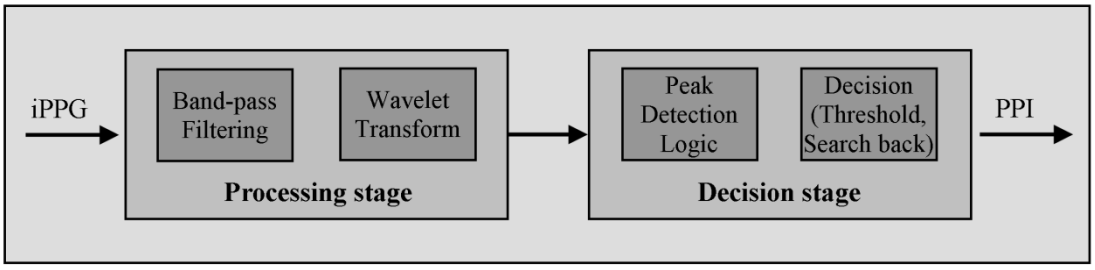

Figure 4.19 – A schematic structure of the PPI extraction technique.

After the spatial averaging of the original images, PPG signals within each sub-window were first bandpass filtered with the cut-off frequencies set at [0.5, 4] Hz to reduce the low-frequency variations in baseline and to enable reliable detection of the pulse feet and peaks. A Wavelet Transform was then performed on the obtained PPG signals. Each peak and trough pair in the PPG signals corresponds to a positive maximum and negative minimum pair, with the two zero-crossing points indicating the peak and trough positions. The locations of the zero-crossing points (n_0), where the minimum values were revealed, were saved as the raw/uncertified trough positions. To further eliminate false positive/negative trough detection and to improve the accuracy, a semi-automated precaution was employed in the present study. Specifically, a manual validation was initially conducted to verify n_{0_1} as the first trough

position. HR was then calculated within a moving window $W_{t1,t2}$ ($t2 - t1 = 10\ s$ in the present study), then [0.9, 1.1] of the HR^{-1} was adopted as the PPI threshold. If $0.9HR^{-1} < |n_{0\_i1} - n_{0\_i2}| < 1.1HR^{-1}$, where $t1 \leq n_{0\_i1}, n_{0\_i2} \leq t2$, the algorithm considers n_{0_i2} as a valid trough position, otherwise, if no valid trough position is found, a search back approach is performed to find the minimum value within the threshold range and a warning index is saved for post validation. Once the trough positions have been obtained, the PPI sequences could be calculated accordingly. Figure 4.9 presents a result of the present trough detection technique.

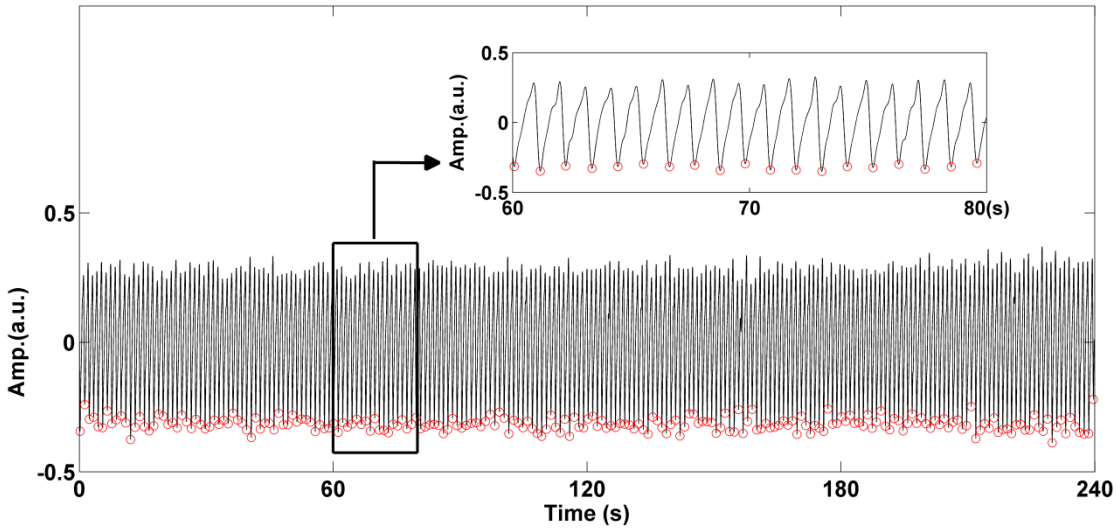

Figure 4.20 – A demonstration of the custom-built trough detection algorithm. The black signal is the band-passed (0.5 – 4 Hz) iPPG signal randomly picked from one of the eight recordings while red circles indicate the troughs. A (60 – 80 s) window gives a close up view of the processed data.

4.3.5.2 PRV analysis

Time Domain: Amongst the HRV evaluation methods, time domain measurements are typically the simplest to perform. With these methods, the instantaneous heart rate or the intervals between successive normal complexes can be determined for any point in time. In a continuous ECG recording, each QRS heart beat is detected, and the so-called normal-to-normal (NN) intervals (i.e., all intervals between adjacent QRS complexes resulting from sinus node depolarisations) and the mean NN interval. Through statistical analysis, the measurements, e.g., SDNN (standard deviation of the NN interval), RMSSD (the square root of the mean squared differences of successive NN intervals), NN50 (the number of interval differences of successive NN intervals greater than 50ms) and pNN50 (the proportion derived by dividing NN50 by the total number of NN intervals) can be calculated. The series of NN intervals can also be converted into a geometric pattern from which the measurement can be

obtained (for a review, see [31, 97-99]).

Frequency Domain: The time domain methods are computationally simple, but lack the ability to discriminate between sympathetic and parasympathetic contributions of HRV. Various spectral methods for the analysis of the tachogram overcome this issue and have been applied since the late 1960s. Power spectral density (PSD) analysis provides the basic information of how power (i.e., variance) distributes as a function of frequency. The power spectrum of HRV signals for healthy subjects consists of three major frequency bands: VLF (very low frequency), LF (low frequency), and HF (high frequency). The distribution of the power and the central frequency of these components are not fixed but may vary in relation to changes in autonomic modulations of the heart period (for a review, see [31, 97-99]).

a) High Frequency

Due to inspiratory inhibition of the vagal tone, the heart rate shows fluctuations with a frequency equal to the respiratory rate [100]. The inspiratory inhibition is evoked primarily by central irradiation of impulses from the medullary respiratory to the cardiovascular centre. In addition, peripheral reflexes due to hemodynamic changes and thoracic stretch receptors contribute to respiratory sinus arrhythmia [101]. Fluctuations with the same frequency occur in blood pressure are known as Traube-Hering-Mayer waves. Respiratory sinus arrhythmia can be abolished by atropine or vagotomy [101, 102] and is parasympathetically mediated. The respiratory frequency band is considered to range (nominally) from about 0.15 to 0.4 Hz in humans but may extend below 0.15 Hz and up to 1 Hz or more for infants and for adults during exercise.

b) Low Frequency

The heart period oscillations also occur at low frequencies (about 0.05-0.15 Hz), including a 0.1 Hz component that is sometimes referred to as the 10-second rhythm/Traube-Hering-Mayer wave [103]. This frequency range has been suggested to originate from self-oscillation in the vasomotor part of the baroreflex loop. These intrinsic oscillations result from the negative feedback in the baroreflex [104] and are accompanied by synchronous fluctuations in blood pressure. The frequency of the fluctuations is determined by the time delay of the system. They are augmented when sympathetic tone is increased [105] and they decrease with sympathetic or parasympathetic blockade [101, 105].

c) Very/Ultra Low Frequency

These very low frequency (<0.05 Hz) heart period oscillations have been studied much less than higher frequency rhythms. Peripheral vascular resistance exhibits intrinsic oscillations with a low frequency [106, 107], where these oscillations can be influenced by thermal skin stimulation [108] and are thought to arise from thermoregulatory peripheral blood flow adjustments. The fluctuations in peripheral vascular resistance are accompanied by fluctuations with the same frequency in blood pressure and heart rate [108] and are mediated by the sympathetic nervous system.

Nonlinear: Conventional spectral methods of HRV analysis based on the Fourier transform technique are not suitable for analyzing non-stationary signals. Recent developments in the theory of nonlinear dynamics have paved the way for analyzing signals generated from nonlinear living systems [109]. It is now generally recognized that these nonlinear techniques are able to describe the processes generated by biological systems in a more effective way. The commonly employed estimations include correlation dimension (CD), largest Lyapunov exponent (LLE), SD1/SD2 of Poincare plot, ApEn (approximate entropy), Hurst exponent, fractal dimension, α-slope of DFA and recurrence plots.

In the present work, time domain analysis, e.g., mean pulse-to-pulse intervals and standard deviation of pulse-to-pulse intervals, and frequency domain measurements, e.g., low frequency components, high frequency components and the corresponding normalization, were employed to quantify the pulse rate variability. PPI sequence is an unevenly sampled time series which could not be directly adopted for the frequency domain analysis. Hence, we first interpolated PPI sequence with cubic splines and then regularly re-sampled it at 4 Hz. The power spectral density analysis could be employed on the obtained constructed even sampled PPI sequence.

This chapter has provided a thorough introduction of the novel image photoplethysmography setup which consists of a hardware platform and a software platform. The hardware platform, including a sensing system and a reference system, is developed to record the images according to different requirements and situations and simultaneously provide a reference PPG signal for further validation. The recorded images were further categorized and analyzed with our novel software platform to reliably extract the embedded physiological parameters via motion attenuation technique and blind source separation.

5 EXPERIMENT 1 – EXERCISE STUDY

Having the well developed iPPG platform, this chapter moves on to detailing the remote physiological assessments. Specifically, this chapter begins by designing an exercise experiment protocol for the remote heart rate and respiration rate measurements. The post-exercise iPPG performances are then statistically validated with the contact results. To facilitate the appraisal of the effects of exercise on the cardiovascular system and evaluate the tolerance of our novel motion cancellation technique, an additional experiment is presented to remotely assess the pulsatile and respiratory variations during exercise. The outcome from this chapter thereby leads to a new avenue for non-contact sensing of vital signs with potential applications in triage and sports training.

5.1 BACKGROUND

Exercise is normally recommended by clinical professionals for the benefits of human healthcare. Having an appropriate physical activity not only maintains fitness but also boosts the immune system, and prevents diseases like cardiovascular illness, asthma, obesity and the side effects followed [110]. Besides, numerous epidemiologic studies provide strong evidence that occupational or recreational exercise reduces mortality from cardiovascular disease. However, the "dose" of exercise, i.e., the intensity, duration, and frequency of training required to achieve and optimize this response, has yet to be fully understood [111]. For instance, many investigators argued that moderate-intensity exercise training is sufficient to produce substantial benefits [112]. While others claimed that high-intensity training produces proportionally greater responses [113]. Yet, overwhelming exercise can be hazardous to the human body and can result in sudden death [114]. PPG is an optical technique that non-invasively measures arterial pulsations in-vivo, and its ease of use, low cost and convenience make it an attractive area of research in the biomedical and clinical community. The characteristics of the original PPG technique, however, prevent its application in appraising the physiological parameters in sports training. Specifically, conventional contact PPG sensor often comes with a soft cable which constrains the free movements during the measurement and the feature of susceptible to motion-induced signal corruption make it even impossible to obtain reliable results. A remote technique could offer reliable and comfortable assessment of the cardiovascular system during and after exercise, and is therefore worth developing. Recently, Wieringa and colleagues have introduced a multiple wavelength imaging PPG device that provides a potential route toward contactless blood oxygen saturation assessment [52], and Verkruysse and co-workers have reported a remote PPG signal acquisition technique based on a digital camera using ambient light illumination [48]. Furthermore, we have previously presented an integrated imaging PPG setup for the detection of tissue opto-physiological properties [73]. These recent progresses in iPPG research activities have stimulated our interest in the remote assessment of the cardiovascular system for evaluation of the influence of exercise.

5.2 EXPERIMENTAL STUDIES

In this chapter, two experiments were performed, the purposes of which were (1) to assess the practicability of the iPPG setup in providing relevant physiological parameters during various

exercise situations, and (2) to assess the performance of the motion artifact reduction technique. The recording of the first experiment was taken with the subject at rest to minimize motion, and those of the second experiment were taken with the subject performing various intensities of exercise. Hence, individual image processing procedures for each experiment were adopted. Specifically, a spatial averaging approach was first conducted to generate the reduced frames for experiment 1. Then the joint time-frequency analysis (time-frequency representation (TFR)) was employed to trace the physiological parameters. In experiment 2, a motion artifact reduction technique was applied before the spatial averaging step common to both experiments. Once the reduced frames were obtained, a blind source separation technique (single channel independent component analysis, SCICA) was performed on the iPPG signal to extract the pulsatile and respiratory waveforms. The time-varying heart and respiration rate was then accessed via the TFR.

5.2.1 Study 1: Approach

None of the subjects involved in this study had any known cardiovascular disease and none were diabetic. The detailed information of these subjects is summarized in Table 5.1. Informed consent was obtained from all of the subjects in accordance with the university ethical committee and in compliance with the Declaration of Helsinki. All subjects were asked to refrain from consuming caffeine or alcohol, and were asked not to smoke or undertake strenuous exercise for the two hours preceding the study. Details of the participant information and anonymous laboratory trial form are listed in Appendix I.

Table 5.1 – Subject characteristics

Variable	Mean ± S.D.
n, male/female	12 (10/2)
Caucasian/non-Caucasian	8/4
Smoker[†]/non-smoker	4/8
Age (years)	31.3±12.7
Height (cm)	177±7.3
Weight (kg)	73.8±13.0
BMI (kg/m^2)	23.5±3.5
Rest HR (bpm)	68.3±12.1
SBP (mmHg)	110.7±13.0
DBP (mmHg)	67.6±7.5

BMI indicates body mass index; HR, heart rate; SBP, systolic blood pressure; DBP, diastolic blood pressure.

[†] Four participants are habitual smokers with over 6 years smoking history.

5.2.1.1 Experimental protocol

The experimental procedures are depicted in Figure 5.1. All measurements were taken in a darkroom with a stable temperature (27±1℃) by a trained operator. For this experiment, twelve healthy subjects aged 20-55 years were enrolled from Loughborough University. Upon arrival, each subject was required to sit on an adjustable chair and rest for at least 10 minutes before blood pressure measurements were taken from their left arm using a clinically validated blood pressure monitor (Model: Omron M6, Omron, Japan). Each subject was then asked to sit at ease and rest their right hand, maintaining it as motionless as possible during the image recording. A soft cushion was placed under the hand to further minimize the motion. The right palm of each subject was exposed to the infrared ring light and the distance between camera lens and skin was approximately 350 mm. A commercial contact pulse oximetry sensor (Model: P871RA, Viamed, U.K.) was placed on the index finger of the right hand to measure the participants' pulse signal for subsequent validation of remotely acquired physiological signals. The obtained analog signal outputs from the contact sensor were digitized using a DISCO4 (Dialog Devices, U.K.) data acquisition system comprising a 12-bit A/D converter running at a sample frequency of 128 Hz. The images captured from the camera were synchronized to the physiological signals acquired from the contact sensor via an additional signal from the camera to the A/D converter.

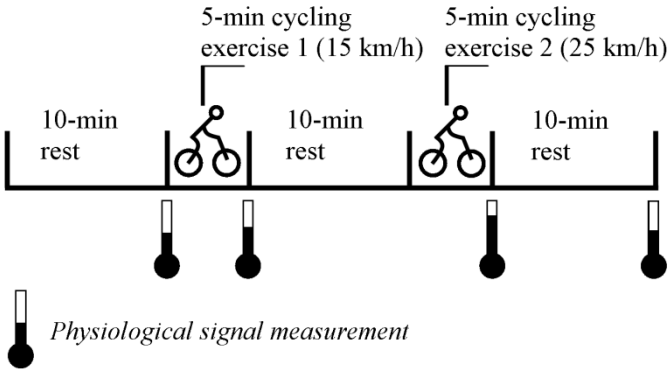

Figure 5.1 – The schematic diagram of the experimental protocol.

The images were capture for 34 seconds at a sample rate of 50 fps and an exposure time of 15 ms, yielding raw images with 640×480 pixels resolution. Contact PPG signals were captured from the finger probe for about 3 minutes to verify that the heart rate was stable. The acquisition of frames was initiated 60 seconds later, at which time a synchronization signal

triggered simultaneous recording of signals from the finger probe. The subject was then asked to ride a gym cycle (Model: XR-580, PowerTrek, U.K.) at a speed of 15 km/h (*exercise 1*) for 5 minutes. Immediately after the exercise, the subject's blood pressure and second set of images was acquired, again for 34 seconds. After 10 minutes rest, the subject performed another 5 minutes of exercise at 25 km/h (*exercise 2*) and the post-exercise data acquisition procedures were repeated. A final set of measurements were taken after a further 10 minutes rest period.

5.2.1.2 Image processing

PPG is susceptible to motion-induced signal corruption, making motion artifact attenuation one of the most challenging issues in iPPG signal processing and physiological assessments. Once a set of recordings was acquired, the raw image frames were divided into discrete sub-windows to produce a new set of reduced frames, where the value of each pixel in the reduced frame was set as the average of all the pixel values within each sub-window. Though compromising the spatial resolution, such a procedure has been shown to significantly improve the signal to noise ratio [48]. This approach could be explained with the novel opto-physiological model. As detailed in Chapter 3, the 2-D motion modulated function is defined as: $f_{QE_{2-\mathrm{D}}} = e^{-(x^2+y^2)/2\sigma^2}$, where $x = 0$ & $y = 0$ means no motion and $f_{QE_{2-\mathrm{D}}}$ peaks at 1. Hence, under the condition with small motion corruptions where the shift x and y is minor, the averaging approach calculates the mean value within the average-window, which could attenuate the relative small motion artefacts. A demonstration figure has been presented to illuminate such effect (Figure 5.2). As it can be seen, even within a small region of interest (ROI) (Blue: 2×2 pixels) the fundamental respiration and heart rate waveform could still be detected. With the increase of the ROI (Green), the waveform is clearly identified and the 2nd and 3rd harmonic components are better illustrated. With further increase of the ROI (red), though the fundamental heart rate and respiratory waveform could still be visible, there is no significant improvement of the signal quality compared to the medium (Green) window. The findings thereby demonstrate the practicability of the novel opto-physiological model in attenuating the motion corruptions and obtaining reliable physiological measurements.

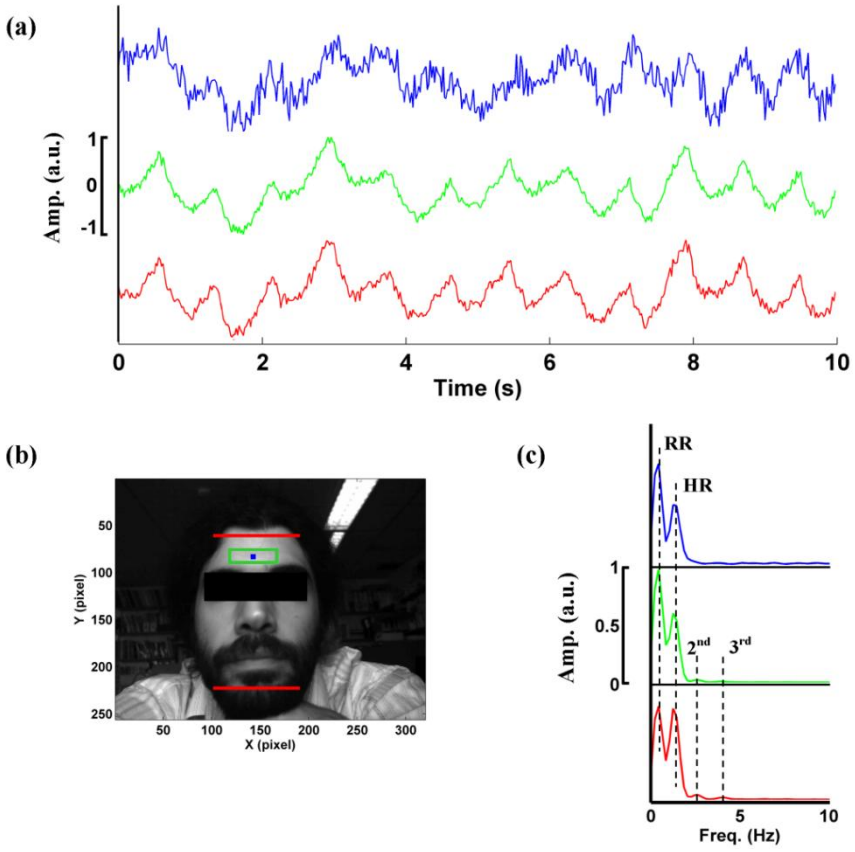

Figure 5.2 – The normalized PPG signal (a) obtained as the average value of three region of interest (highlight in red, green, and blue box) as indicated in (b). The corresponding normalized power spectral density maps of the obtained signals are also presented.

In this exercise study, the sub-window size of 10×10 pixels yielded low distortion and consistent peak-to-peak intensity with respect to signals from larger window sizes. Hence, it is safe to employ a window size of 10×10 pixels for the image preprocessing which maintains the key features of PPG waveform and also increasing the SNR. Such an approach resulted in a reduced frame size of 64×48 pixels, yielding PPG signals at each pixel position across a sequence of frames. The PPG signals were then band-passed filtered using a 5^{th} order Butterworth filter. Cut-off frequencies were set at [0.5, 4.0] Hz to allow a wide range of heart rate measurements (30 to 240 bpm).

5.2.1.3 Perfusion mapping

As it has been detailed in Chapter 3, the light intensity in tissue can be briefly described by the Beer-Lambert law:

$$I_0 = I_i \cdot \exp(-\mu_{a,s} L_s) \cdot \exp(-\mu_{a,a} L_a) \quad [\mathbf{5.1}]$$

where I_0 is the transmitted light intensity, I_i is the incident light intensity; $\mu_{a,s}$ is the wavelength-dependent absorption coefficient of the static component of tissue, in units of cm^{-1}; and $\mu_{a,a}$ is the absorption coefficient of the arterial blood; and L_s and L_a, represent, respectively, the optical path length of static and arterial components. The latter, pulsatile (ac) component, attributed to changes in blood volume synchronous with the heartbeat, can be expressed as:

$$\Delta I_0 = -I_i \mu_{a,a} \cdot \exp(-\mu_{a,s} L_s) \cdot \exp(-\mu_{a,a} L_a) \cdot \Delta L_a \quad [\mathbf{5.2}]$$

Then the ac/dc ratio is acquired through normalization: $(\Delta I_0)/I_0 = -\mu_{a,a} \Delta L_a$, which depends upon the relative changes in the arterial optical path length ΔL_a. We have previously presented a Monte Carlo (MC) simulation based opto-physiological model of multi-layered skin tissue [115]. With unique tissue optical properties and specified geometries, each layer contributes differently to the changes of arterial optical path length. In this study, a six-layer skin tissue model [15] was employed in a MC simulation to obtain the contribution of each layer to ΔL_a. The arterial pulsation was simulated by adding pulsatile blood into non-pulsatile tissue, consequently changing the volume fraction. Hence, the blood perfusion map of each specific layer could be calculated. Detailed procedures could be found in [116].

5.2.1.4 Statistical analysis

Statistical analysis was performed with SPSS 15 for MS-Windows. Significant difference between the physiological measurements after different conditions was tested with ANOVA to demonstrate the influence of exercise on the cardiovascular system. Post hoc analysis with Duncan's test was also employed to test the group difference. Moreover, to test the performance of the iPPG system, Bland-Altman analysis [117] was performed for comparison between iPPG and the cPPG. The difference between iPPG and the cPPG was plotted against the averages of both systems, as was the mean and standard deviation (S.D.) of the differences, the mean of the absolute differences, and 95% limits of agreements (±1.96 S.D.). In addition, the Pearson's correlation coefficients and the corresponding *p*-value were calculated to estimate HR from iPPG and contact-PPG system.

5.2.2 Study 1: Results

The post-exercise measurements make it possible to validate the performance of the iPPG system with the gold standard cPPG system. Hence in this section, the results obtained from two platforms were statistically appraised. Furthermore, the physiological parameters, e.g., systolic/diastolic blood pressure, provided added information for reliable and accurate evaluation of the exercise on the cardiovascular system.

5.2.2.1 Physiological variables

As mentioned previously, physiological measurements were performed at four phases, i.e., rest, post-ex1, post-ex2, and recovery. Figure 5.3 summarizes the results of the measured variables: heart rate (HR), systolic blood pressure (SBP), and diastolic blood pressure (DBP).

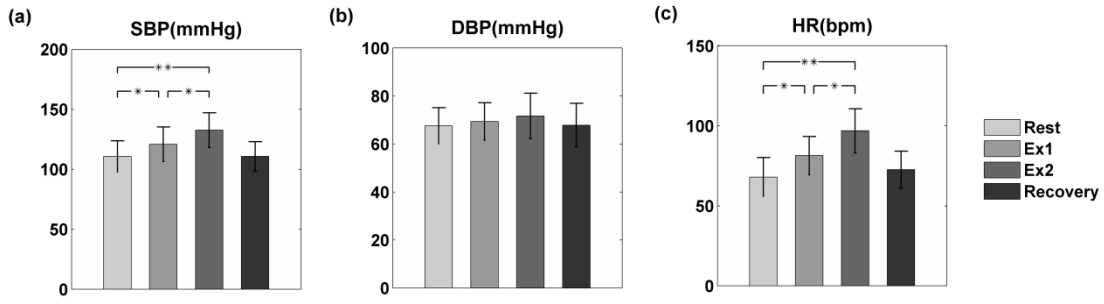

Figure 5.3 – Effects of exercise on blood pressure and heart rate. Each bar represents the average value of 12 subjects for (a) SBP, (b) DBP, and (c) HR for each state (rest, post-ex1, post-ex2, recovery). Error bars represent standard deviations. Significant statistical differences are indicated with * for $p<0.05$ and ** for $p<0.01$.

ANOVA showed a significant influence of exercise on SBP and HR ($F=7.61$, $p=0.001$ & $F=12.67$, $p<0.001$). Post hoc tests revealed that compared to the rest condition, the HR and SBP were significantly higher than baseline after both exercise levels (ex1 v.s. rest, $p<0.05$, ex2 v.s. rest, $p<0.01$). A significant difference in HR and SBP was also observed between exercise levels. Higher HR ($p=0.004$) and SBP ($p=0.039$) were revealed after exercise 2 (25km/h) compared to the moderate exercise level (15 km/h). After 10 minutes rest, the hemodynamic parameters all returned to the rest level. No significant effect of exercise on DBP was observed.

5.2.2.2 iPPG results

Figure 5.4 shows an example of the PPG signals obtained from a single subject and the TFR traces, with HR frequency and 2nd harmonic components. As it can be seen in the TFR plots that the HR derived from iPPG signals was in excellent agreement with the HR obtained from the commercial pulse oximeter sensor readings. A slowly varying HR is also detected from the TFR trace indicating the potential use of TFR in revealing the time-varying HR after exercise.

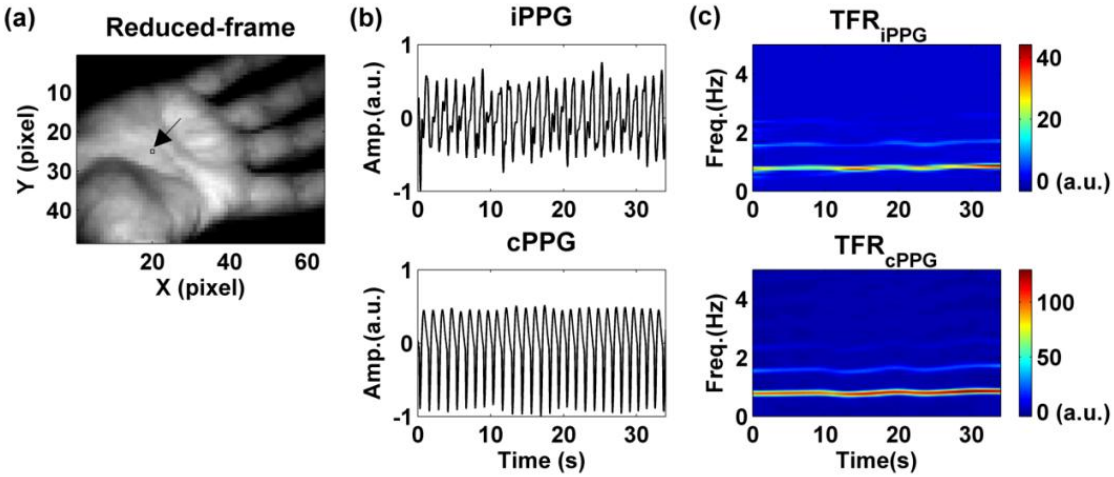

Figure 5.4 – A representative figure showing (a) a reduced frame (frame 49, t=1s), (b) contact and image PPG signals, and (c) the corresponding TFR results. The upper TFR trace is from the non-contact iPPG and the lower is from the contact PPG with the colour bar indicating the absolute power intensity. The signal is from Subject #7 (Male, age=55 years) under rest condition. The position from which the iPPG signal was obtained is highlighted with a black box (1×1 pixel) and an arrow.

To statistically evaluate the performance of the iPPG system, Bland-Altman plots were employed to determine the limits of agreement in HR between iPPG (HR_{iPPG}) and cPPG (HR_{cPPG}) measurements. The HR_{iPPG} was obtained through averaging the HR within all sub-windows (64×48 pixels). Here, the historical HR estimations were used to define a maximum threshold for deviation among different regions. Firstly, the HR was calculated in the middle of the processed frames (x=32, y=24), then the HR within this region was treated as a reference. Successive calculations were then performed where, if the difference between the current HR estimation and the reference value exceed the threshold (9 bmp in this study), the algorithm isolated these regions as non-tissue or corrupt and rejected the invalid HR. The comparison of HR_{cPPG} and HR_{iPPG} is shown in Figure 5.5. Compared to the physiological

measurements, a similar HR trend is detected. Specifically, the mean bias is 0.3 bpm with 95% limits of agreement -1.3 to 2.0 bpm in the rest state. While the mean bias obtained after the first and second exercise are -0.8 and -0.6 bpm respectively. The correspond 95% limits of agreement are from -2.3 to 0.7 bpm and -2.4 to 1.3 bpm. After 10 minutes rest, the mean bias is 0.2 bpm with 95% confidence interval -2.4 to 2.9 bpm. Moreover, significant correlation coefficients between both measurements are revealed in all states (Pearson's correlation, $r^2>0.9$, $p<0.01$).

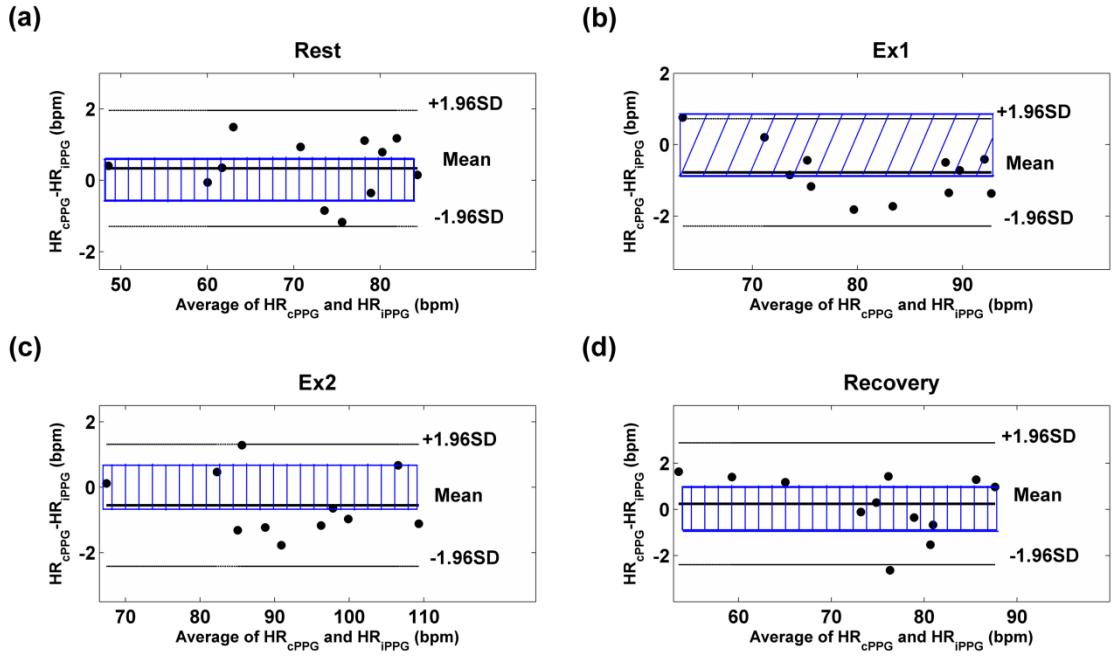

Figure 5.5 – Bland Altman plots showing the average of the HR measured by the cPPG and iPPG, plotted against the difference between them for each subject at (a) rest, (b) post-ex1, (c) post-ex2, and (d) recovery states, with the blue box showing the confidence intervals for the bias (vertical, $p < 0.05$, oblique, $p < 0.005$).

As mentioned above, a six-layer tissue model was employed in a Monte Carlo simulation to obtain the contribution of each layer to the output signals by accounting for the absorption (i.e., photon packet intensity) and scattering (i.e., optical path length) properties of tissue. The minima and maxima of the iPPG signals were identified using a custom algorithm in Matlab. The amplitude of the PPG signal ($|ac_i|$) was then determined for each pulse and the mean peak-to-peak amplitude served as the ac part. The slowly varying baseline was obtained by low pass filtering the iPPG signal (<0.5 Hz), and the mean value of the baseline was taken as the dc component. Accordingly, the ac/dc ratio for each sub-window could be calculated.

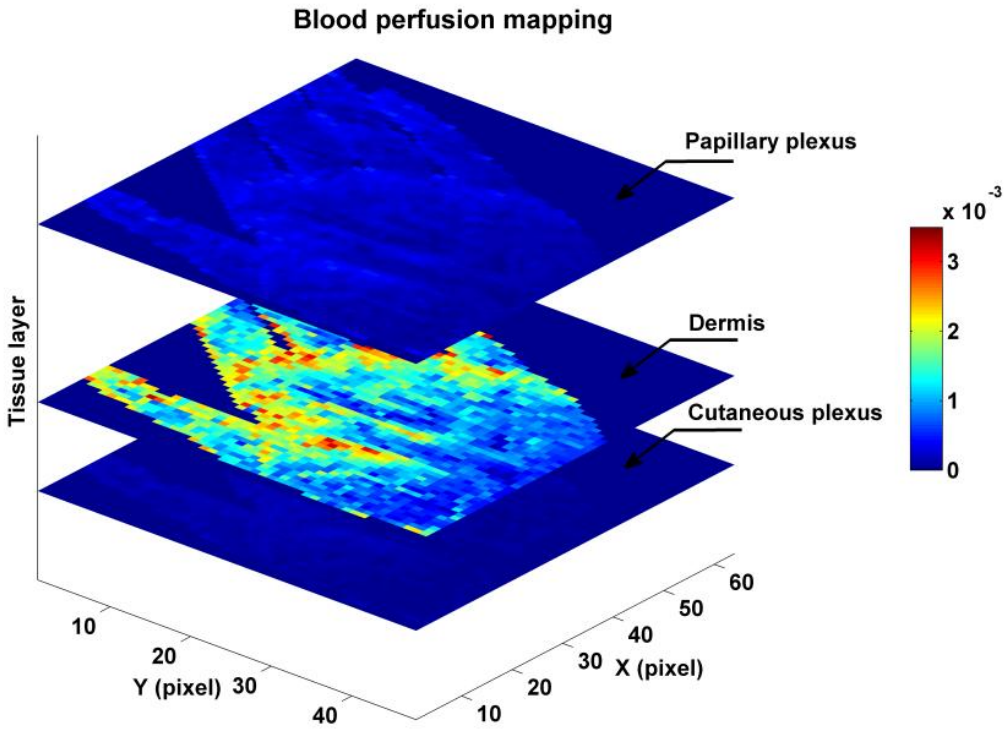

Figure 5.6 – Layered blood perfusion map with colour bar indicating the intensity (a.u.). The signal is from Sub #7 (Male, age = 27 years) at rest condition.

Figure 5.6 shows a layered blood perfusion map from a subject (Sub #7) at rest. Within the six-layer tissue model [15], the blood fraction was set to zero within the outermost layer, i.e., epidermis and dermis, which served as a wavelength-dependent attenuator. The contribution of the blood fraction to the three inner layers, i.e., papillary plexus, dermis, and cutaneous plexus was demonstrated. It can be seen in Figure 5.6 that the dermal layer contributes the most of the output signals and a stronger perfusion in the fingers is also revealed.

5.2.3 Study 2: Approach

The performance of the iPPG system was evaluated by comparing it with a commercial pulse oximeter sensor. The strong correlation and good agreement between these two methods for PPG capturing signals indicate that the iPPG system can successfully obtain information about cardiovascular variables. To appraise our novel motion attenuation technique and more importantly to investigate the continuous pulsatile and respiratory variations under various exercise levels, an additional experiment was conducted.

5.2.3.1 Experimental protocol

Differed from the experiment 1, the video was taken from the face of one male volunteer (age = 27 years, height = 178 cm, BMI = 20.5 kg/m^2). The face is a convenient target for remote monitoring as it is uncovered during the cycling exercise, and it has been shown in the literature that the facial PPG signal is typically stronger than that from other anatomical locations [48]. A continuous set of data was recorded whilst the subject performed four routines, each lasting 3 minutes. In the first routine, the subject sat still for recording of baseline signals (rest); in the second and third routines the subject performed cycling exercise at 15 km/h and 25 km/h respectively; while in the fourth routine, the subject sat still for recording of his recovery from exercise. For the video recording, the participant was asked to move naturally with his face pointing directly towards the camera, only taking care to remain seated and to maintain planar alignment of his face with the camera during the exercise. Images of 512×512 pixels were taken from the face at a lower frame rate (20 fps, $T_{exposure}$ = 40 ms) to allow image capture over an increased duration of exercise (approximately 12 minutes). The distance between the camera lens and the face was about 400 mm, and all other factors were maintained as in experiment 1. The experimental procedures are depicted in Figure 5.7.

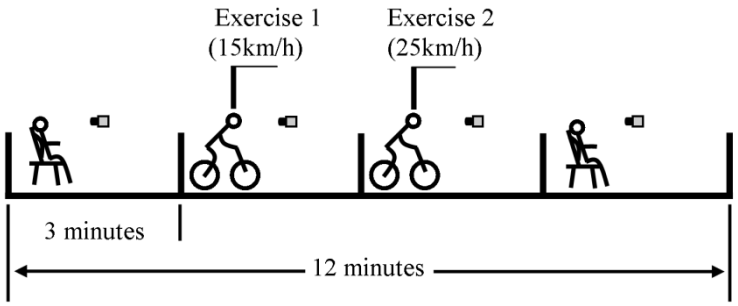

Figure 5.7 – The schematic diagram of the experimental protocol.

5.2.3.2 Image processing

An overview of the image processing procedure for the face recordings is schematically presented in Figure 5.8. Raw frames were submitted to the image registration algorithm to detect planar shifts within the sequence of frames and to shift these into alignment. Specifically, a reference region (50×50 pixels) of high contrast (around the nose) was manually chosen on the first frame of the set. The planar shift was determined via 2-D cross correlation of the reference region and regions on all subsequent frames. As mentioned in

Chapter 4, 2-D cross correlation is a basic statistical approach which measures the degree of similarity between an image and a template. The cross correlation peaks at position where the template most closely matches the image, where the motion modulated function reaches the local maximum. Therefore, it is possible to reveal the shift by computing the correlation over template-sized regions in the image. Alignment of the raw set of frames resulted in a set of smaller frames (300×400 pixels). These stabilized frames were then divided into discrete sub-windows, as described above to further increase the signal to noise ratio and a new set of reduced frames were obtained.

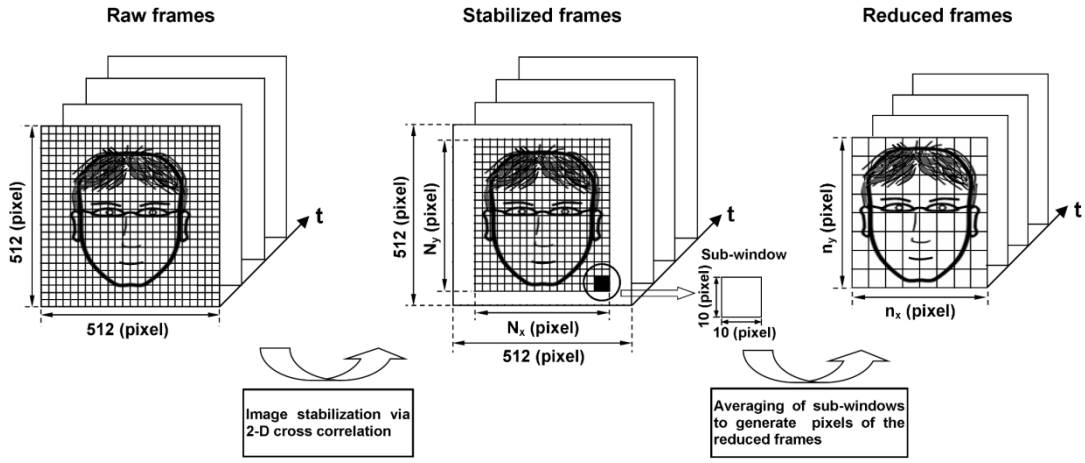

Figure 5.8 – A schematic diagram of image pre-processing approach in experiment 2.

Figure 5.9 shows the coordinates shift detected by the image registration technique. It can be seen that even in the motion-less rest/recovery state, small motion artifacts still exist. Large and significant motion artifacts were uncovered in Ex1 and Ex2 states. Besides, the swaying (Left-Right) movements seem to dominate the motion artifacts.

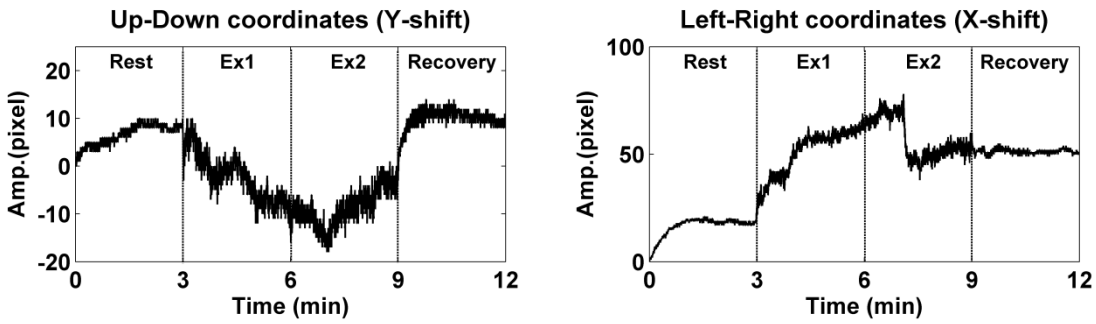

Figure 5.9 – The coordinates shift detected by the novel image registration technique.

The achievements of the image registration technique have been demonstrated in Figure 5.10, which presents the influence of motion artifacts on (a) the original images and (b) the significant improvement on the stabilized images. In the original unstabilized image, a blurred pattern is clearly visible after averaging all the original frames, suggesting a significant misalignment of images in the full sequence, which would result in an offset from the maximum point in the motion modulated function. While in the average of the stabilized frame sequence, significant improvements has been revealed, indicating the practicability and effectiveness of the novel motion attenuation method. In the present study, the template (50×50 pixels) was chosen around the nose part. It can be seen that the stabilized image has a clear presentation around the nose area. Such a template was employed for two main reasons: a) the template was almost in the middle of the face which helps the alignment of the whole face; b) the unique characteristic of the nose area guarantees the effectiveness of the image registration.

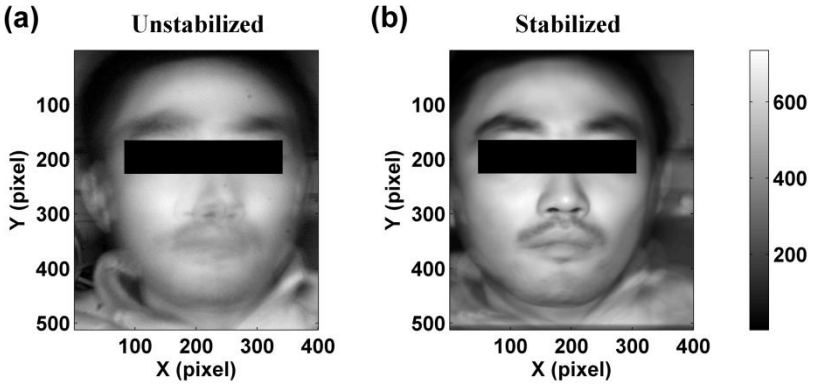

Figure 5.10 – A demonstration of the motion attenuation method. The unstabilized (a) and stabilized (b) images were obtained from averaging all frames in the sequence, with grayscale bar indicating the intensity of the pixel value.

5.2.4 Study 2: Results

Figure 5.11 depicts a 12 minutes iPPG signals (Figure 5.11 (a)) extracted from the motion compensated face images of one male subject who was asked to perform two sets of cycling exercise continuously. The dashed vertical lines indicate different states, i.e., rest, ex1, ex2, and recovery. The region where the iPPG signal is obtained is shown as rectangular areas (10×5 pixels) on the forehead (Figure 5.11 (a)). For qualification of the effectiveness of SCICA, three iPPG signals (duration = 15 s) were selected at random from data

corresponding to the low, medium and high motion conditions, i.e., rest, ex1, and ex2 respectively. SCICA was then used to extract physiological components from these signals. As it can be seen in Figure 5.11 (c), the physiological information, i.e., respiration and heart rate, is clearly exhibited in the iPPG signals from the motionless rest condition. Both HR and RR are more clearly visible in the extracted components obtained through SCICA. Compared to the rest condition, the oscillations of RR and HR in both ex1 and ex2 states are poorly represented due to the motion artefacts introduced by strenuous exercise even after motion attenuation approach. However, the two target components can be clearly identified after the extraction in both exercise conditions (Figure 5.11 (c)). The selected segments in Figure 5.11 (c) are representative of the SCICA for the whole data set in each state.

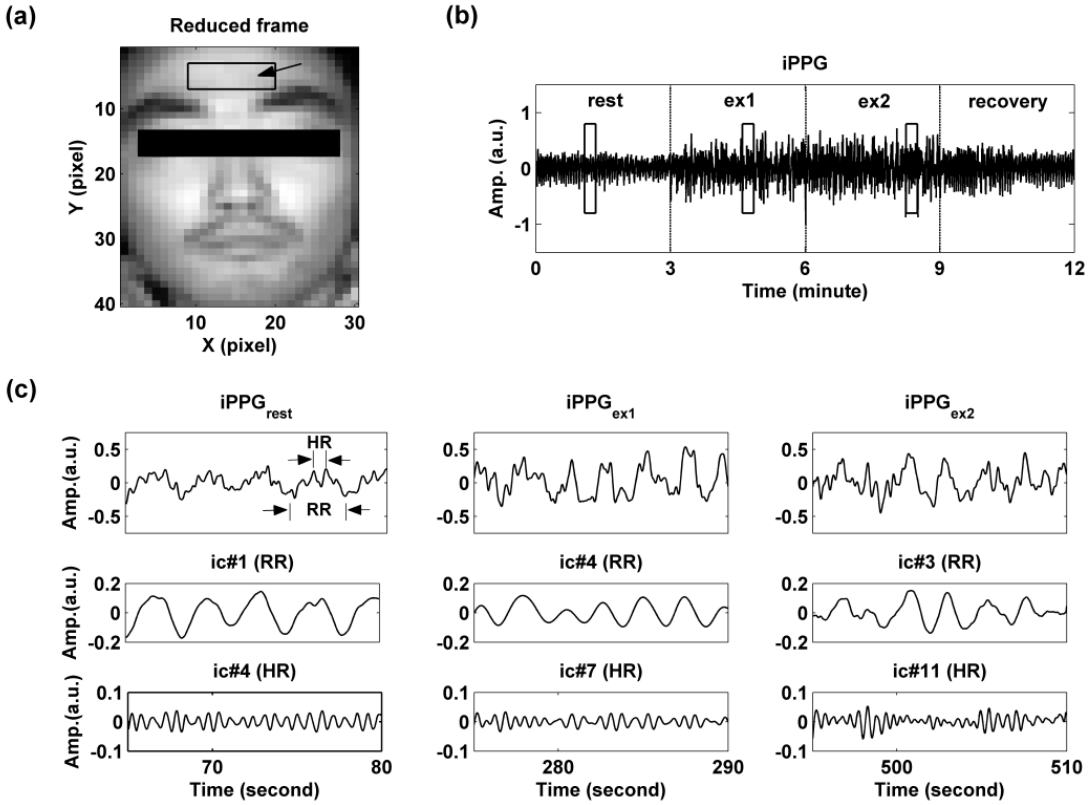

Figure 5.11 – A representative figure showing (a) a reduced frame (frame 239, t=12s) under rest condition from experiment 2, (b) iPPG signals, and (c) the extracted physiological components for three randomly selected sets of 15 s iPPG signal under resting conditions (t = 65-80 s), exercise 1 (t = 275-290 s), and exercise 2 (t = 495-510 s). The region from which the iPPG signal is obtained is indicated with a black box (10×5 pixels) and an arrow. The position where the three sets of iPPG signal were selected is highlighted with three boxes.

The continuous nature of the extracted respiratory and pulsatile variation under different exercise conditions is depicted in Figure 5.12. Here, the characteristics of the HR trend are very similar to the steady post-exercise results in experiment 1, thereby supporting that the extracted components in Figure 5.11 are true HR and RR. Compared to the rest condition, the RR and HR increase in both ex1 and ex2 states. Specifically, at t = 3 minutes the subject was asked to perform a moderate cycling exercise at 15 km/h, the RR in the ex1 state is found to increase from 0.3 to 0.4 Hz (Figure 5.12 (a)). Simultaneously, the HR gradually increases from 1.45 to around 1.75 Hz after about 15 seconds of cycling (Figure 5.12 (b)). The high intensity exercise (25 km/h) performed three minutes later resulted in a higher RR and HR. HR peaks at 2 Hz at the end of ex2 while the RR increases to 0.5 Hz. At t = 9 minutes, the subject stopped cycling and was asked to inhale and exhale deeply at a slow pace until t = 10.5 minutes, whereupon the subject was asked to breathe normally. During the subject's deep-breathing period, the TFR diagram reveals higher amplitude of RR as well as a gradually decreasing HR. At the end of monitoring, the subject appeared to recuperate from the physical exercise as both RR and HR returned to the rest level.

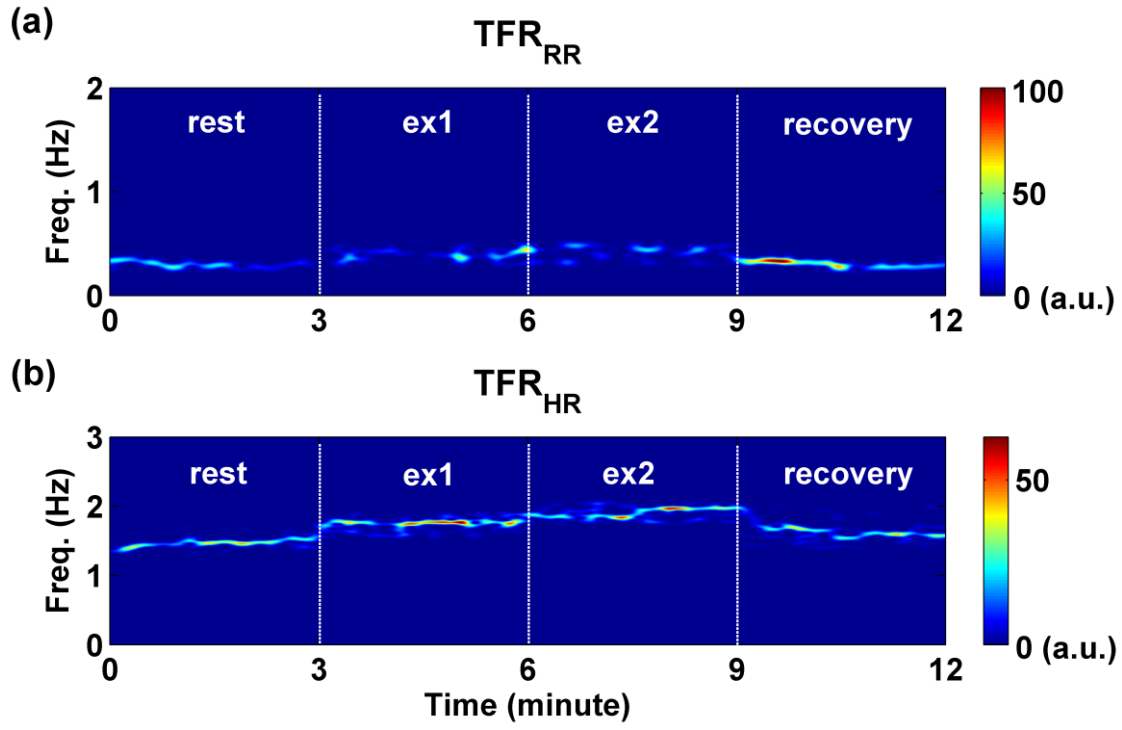

Figure 5.12 – The continuous nature of the extracted respiratory (a) and pulsatile (b) variation under different exercise conditions. Colour bar indicates the absolute power intensity.

5.3 DISCUSSION

The performance of the iPPG system has been evaluated in ten healthy subjects by comparing it with the PPG signals from a commercial pulse oximeter sensor. The strong correlation and good agreement between these two methods for PPG capturing signals indicate that the iPPG system can successfully obtain physiological information about cardiovascular variables such as respiration and heart rate. Besides, the method applied in this exercise feasibility study is well suited for motion-tolerant RR and HR measurement during exercise. The results of the second experiment verify the effectiveness of the proposed software platform for removing motion-associated noise even under physical exercise of high-intensity.

5.3.1 iPPG *v.s.* cPPG

A clear PPG signal has been uncovered from a small ROI (1×1 pixel in the reduced frame) of the recorded images. Besides, a close agreement of HR traces has been revealed indicating the practicability of the novel iPPG system in remote detection of the cardiovascular parameters. Moreover, as it can be seen in Figure 5.5, Bland-Altman analysis showed that the physiological parameters obtained from the iPPG system were comparable with the commercial contact-sensor, e.g., the maximum heart rate difference was less than 3 bpm in all states. Here, the word ‘comparable’ in clinical applications means that measurements by the two instruments or techniques should be sufficiently close, thereby not changing the actions and decisions regarding the patients [49]. The clinically acceptable error of such measurements depends upon the application. For instance, in the Emergency Severity Index triage an adult patient with a heart rate over 100 bpm is considered to be tachycardic [18]. In this case, a difference of less than 3 bpm (<3% error) obtained by our experimental remote iPPG system would be acceptable. Especially given that the measurement can be performed remotely.

5.3.2 Exercise

Few physicians, if any, would dispute that physical activity enhances health. Among other benefits, increased activity is associated with decreased incidence of coronary heart disease, hypertension, non-insulin-dependent diabetes mellitus, and colon cancer, and increased longevity [118]. What is uncertain, however, are the kinds and intensity of physical activity that should be prescribed for health. For instance, Morris et. al., found that to reduce coronary

heart disease risk, moderately vigorous exercise is necessary [119], similar results have been reported in [120]. Yet others maintain that as long as total energy output – even if amassed from light or moderate exercise – is increased, risks of coronary heart disease and premature mortality from any cause are decreased [121, 122]. The Centers for Disease Control and Prevention and the American College of Sports Medicine issued a new, less stringent recommendation: 'Every US adult should accumulate 30 minutes or more of moderate-intensity physical activity on most, preferably all, days of the week' [123]. This recommendation was meant to encourage more exercise among the almost 60% of US adults who engage in little or no leisure-time activity. However, overwhelming exercise can be hazardous to the human body and can result in sudden death [114]. Therefore, it is worth developing a technique which is capable of remote monitoring the physiological parameters during exercise, thereby providing valuable information for the evaluation of the influence of different exercise intensities on cardiovascular system. The outcome from this study leads to a new avenue for non-contact sensing of vital signs in sports training. One potential area which deserves attention is the non-contact blood oxygen saturation (SaO_2) monitoring during the exercise. Further development of a dual-wavelength iPPG system that is motion-tolerant and capable of providing SaO_2 mapping information is the subject of future study.

5.3.3 Image registration

Compared to the contact PPG sensor, the iPPG technique is still not extensively accepted in clinical applications mainly due to the problem of motion artifacts. One recent study [47] reports attempts to remove/attenuate the motion artifacts from iPPG signals. The method was based upon automatic face tracking and blind source separation of multiple signals, i.e., R, G, & B color signals, into independent components. The motion artifacts evaluated, however, were typically slow and relatively small movements such as tilting the head sideways, nodding the head or looking up/down. Although such an approach is not suitable for the present study (monochrome camera), the pioneering research in [47], attempts an alternative approach to compensate for motion for a more effective extraction of physiological parameters. Specifically, in the present study, after a sequence of images has been recorded, image registration technique (2-D cross correlation) are first employed to bring successive images into spatial alignment. From Figure 5.9 we can see that this approach removes most of the motion artifacts and results in accurate and reliable images. However, no approach is perfectly immune to all motion artifacts; thus, it is important to recognize the limitations of the method in the present study. This study addresses the planar motion artifact in pulse

waveforms acquired from iPPG. Though the participant was free to move his body during exercise, actually he was still requested to remain seated to minimize the swaying of body and maintain the direction of his face towards the camera to attenuate the nonplanar motion. Typical movements included lateral tilting the head (where the amplitude increased with exercise intensity), and mild leaning of the body (and hence the head) towards/away from the camera due to deep breathing. Involuntary motion artifacts are inherently complex and cannot completely removed through 2-D cross correlation technique. However, the primary application introduced in this paper is to extract useful physiological variables from the images recorded during exercise. Furthermore, frame numbers in the long term monitoring could be huge, e.g., 14400 frames for 12-min recording at 20 fps. In this study, therefore, the motion artifact reduction technique should be simple as well as accurate. The image registration of the full set of recordings only takes about an hour which seems reasonable for such a huge amount of data (about 10 GB) compared to the conventional contact PPG recordings.

5.3.4 Blind source separation

It is possible that linearity assumed by ICA is not representative of the true underlying mixture in the signals given that the physiological changes in blood volume due to motion are not well understood and could be nonlinear [47]. However, according to Davies & James [82], when the sources do not have substantially overlapping spectral, it is still possible to separate the different components via SCICA. In the present study, separate SCICA was conducted in each state. Though efficient, such approach triggered another limitation of the present study, e.g., the absence of the automated detection of the physiological parameters. As it can be seen in Figure 5.11, the physiological waveforms are not constant in the extracted independent components under different conditions, i.e., the pulsatile signals were recovered in IC #4 in the rest state while in IC #7 and IC #11 in ex1 and ex2 conditions respectively. A further study is needed to develop a fully automated physiological parameters extraction technique.

The emerging field of imaging PPG technologies offers some nascent opportunities in effective and comprehensive interpretation of the physiological parameters, e.g., heart/respiratory rate, tissue blood perfusion and arterial oxygen saturation distributions, indicating a promising alternative to conventional contact PPG. This chapter detailed the practicability and reliability of the novel iPPG system for the recovery of physiological parameters from different anatomical locations under various conditions. The relevant results to the exercise experiment have been distilled and presented, with emphasis on comparative results between iPPG and cPPG as well as the motion tolerant remote physiological monitoring and assessment.

6 EXPERIMENT 2 – PULSE RATE VARIABILITY ANALYSIS

Heart rate variability (HRV) – the irregular time intervals between consecutive heart beats – is a result of rhythmic oscillation of the regulatory components of cardiac activity and regarded to be a valuable parameter for investigating the autonomic nervous system (ANS). In this chapter, pulse rate variability (PRV) which obtained from the remote imaging PPG system was used to be a surrogate of HRV. Two separate studies have been conducted to evaluate the feasibility of the imaging PPG system in appraising the (ANS). The results of this chapter intend to provide some potential route towards remote and noncontact ANS assessment.

6.1 BACKGROUND

In healthy subjects, cardiac function is characterized by irregular time intervals between consecutive heart beats. This heart rate variability (HRV) is a result of rhythmic oscillation of the regulatory components of cardiac activity that function to maintain cardiovascular homeostasis within a defined range and to orchestrate responses to challenges. It is a mirror of the cardiorespiratory control system and a valuable tool to investigate the sympathetic and parasympathetic function of the autonomic nervous system (ANS) [99]. Long before the invention of the electrocardiograph (ECG) and the more recent emergence of modern constructs of HRV, physicians recognized the potential importance of cardiac rhythms. Techniques for studying HRV were limited prior to this century, but for several hundred years physicians have monitored heart sounds and rhythmic shifts associated with aging, illness, and psychological states. The study of these rhythms became a central component of medical diagnostic systems developed in China [98]. The scientific investigation of beat-to-beat heart rate rhythms, however, awaited technological advances that enabled accurate and reliable quantification of the electrical activity of the heart. It could be argued that the origins of the scientific study of HRV predate the development of the ECG. The first documented observation of HRV is often credited to Hales, who observed a respiratory pattern in the blood pressure and pulse of a horse [124]. Since then, several historical studies have highlighted the emergence of HRV as a physiologically meaningful measure (for a review, see [98]) and proven its superiority in appraising the activity of the ANS.

6.1.1 Physiology of Heart rate variability (HRV)

Because of continuous changes in the sympathetic-parasympathetic balance, the sinus rhythm exhibits fluctuations around the mean heart rate. Small adjustments in heart rate are made by cardiovascular control mechanisms (Figure 6.1), resulting in periodic fluctuations in heart rate. HRV primarily emerges through the non-additive activity originating from the individual branches of the ANS, which in turn is influenced by neuronal, humoral and other physiological control and feedback mechanisms. The main periodic fluctuations found are respiratory sinus arrhythmia and baroreflex-related and thermoregulation-related heart rate variability [125, 126]. In a normal heart with an integer ANS, there will be continuous physiological variations of the sinus cycles reflecting a balanced symptho-vagal state and normal HRV.

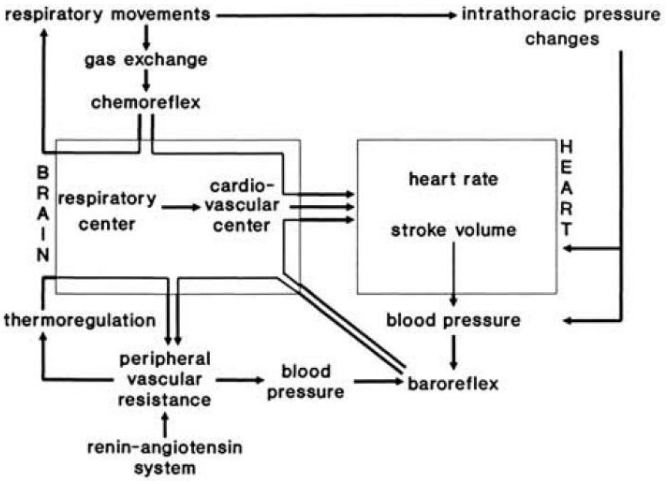

Figure 6.1 – Scheme of the cardiovascular control mechanisms responsible for the main periodic fluctuations in heart rate. The exact pathways through the brainstem are not visualised (image courtesy of [99]).

6.1.2 Pulse rate variability (PRV)

As detailed in Chapter 2, PPG provides a qualitative measure of the tissue blood volume during the cardiac cycle by measuring the light transmission/backscattering through the tissue as a function of time. The AC component of the PPG pulse is synchronous with the beating heart and thereby can be a source of HR information, where the pulse rate can be estimated from the time between systolic peaks of a PPG pulse wave. This enables the simple acquisition of pulse rate variability (PRV), which is the pulse-to-pulse alteration in pulse rate and a potential surrogate of HRV. There are a few studies on the practicability and reliability of PRV analysis, with conflicting results. For instance, Constant and colleagues reported an overestimation of HR respiratory fluctuation resulting from PRV estimation, especially in standing healthy subjects and in patients with low HR variability [127]; while Nitzan and colleagues demonstrated the variability of the PPG parameters in assessment of the function of ANS both in healthy subjects and diabetic patients [128]. The reliability and applicability of PRV therefore requires further investigation. In Chapters 4 & 5, we have introduced and validated a novel iPPG system for the remote monitoring of physiological parameters. Moreover, recent progresses in iPPG research activities [46, 48, 49, 52, 53, 74, 75] have stimulated our interest in the non-contact assessment of PRV.

6.2 EXPERIMENTAL STUDIES

In this study, two experiments were performed for non-contact PRV assessment, the aims of which are (1) to assess the practicability and the viability of the iPPG setup and (2) to assess the stability of the PRV analysis. To accomplish the first aim, ten sets of recordings were taken from one participant in four successive days while in the second experiment the iPPG signals were obtained from ten healthy subjects enrolled at the Blizard Institute of Cell and Molecular Science (BICMS) Pathology Group. The recordings of both experiments were taken with the subject at rest state to minimize motion artefacts. During the image recording, a reference cPPG signal was obtained simultaneously from the reference LED-PPG circuit (Fig. 4.11) as a clean reference signal for comparison. As detailed in Chapter 2 & 4, the maximum sample rate of the iPPG system is around/below 50 fps, which is far from the requirement for effective measurement of HRV (in any case $\geq$ 100 Hz) [31], thereby constraining the remote pulse rate variability (PRV) analysis. Dramatic advances in imaging technology over the past decade, namely the increased speed and performance of digital cameras have led to the development of numerous imaging techniques, thereby making possible the remote assessment of PRV. In the present study, a monochrome CMOS camera (Model: Eo*Sens* MC 1363-63, Mikrotron GmbH, Unterschleissheim, German) with a maximum resolution of 1280×1024 pixels and a 100 fps frame rate in a full resolution has been employed (an even faster speed could be achieved via a region of interest mode). The results in Chapter 5 show comparable abilities between standard contact PPG and iPPG techniques in detecting physiological parameters, thereby promoting this research into remote PRV assessment for evaluation of the ANS.

6.2.1 Approach

In the first comparative study, a total of ten sets of recordings were made from one male subject participant (age = 28, height = 178 cm, weight = 65 kg, BMI = 20.5 kg/m^2). It has been indicated in the literature that neural activities of the ANS, which govern the PRV, have furnished clear examples of circadian rhythms. Specifically, the spectral results of the HRV signals revealed a pronounced and consistent reduction in the markers of sympathetic activity (low-frequency of the spectral component) and an increase in those of vegal activity during the night [129]. Hence, the recordings of the present study was obtained within [9:30, 18:30] (median = 11:00) to avoid such effect. A similar approach has been adopted in *Study* 2 where a total of 10 subjects (Caucasian/non-Caucasian = 7/3), enrolled from the BICMS Pathology

Group, Barts & The London School of Medicine and Dentistry, participated. Detailed information of these subjects is summarised in Table 6.1. None of the subjects involved in this study had any known cardiovascular disease and none were diabetic. The investigation conformed to the principles outlined in the Declaration of Helsinki (1989) of the World Medical Association, and was approved by the local Ethical Committee. The nature of the research was explained to the subjects prior the recordings, and informed consent was obtained.

Table 6.1 – Subject characteristics

Sub No.	Gender	Age (years)	Height (m)	Weight (kg)	BMI (kg/m^2)
#1	M	28	1.78	65.0	20.5
#2	M	65	1.83	73.0	21.8
#3	M	29	1.70	92.0	31.8
#4	F	31	1.60	76.2	29.8
#5	M	30	1.75	69.9	22.8
#6[*]	M	21	1.72	65.0	22.0
#7	M	23	1.72	70.0	23.7
#8	F	44	1.63	56.0	21.1
#9	F	59	1.80	63.5	19.6
#10	M	48	1.84	82.6	24.4
Mean ± S.D.	M/F=7/3	37.8±15.3	1.74±0.08	71.3±10.3	23.8±4.0

[*] The subject could not maintain motionless during the monitoring due to poor health condition and was excluded in the following analysis.

As mentioned above, the neural activities of the autonomic nervous system have furnished circadian rhythms. Hence, the recordings of the present study were obtained within [10:30, 14:00] (median = 12:50) to avoid such effect. The signals were found to be corrupted in Sub #6 and no meaningful results could be obtained. In total, nine sets of image sequences were obtained and further processed in *Study* 2.

6.2.1.1 Experimental protocol

The images were taken from the palm of the participant's left hand with the contact commercial PPG sensor (Model: Model: SA30014C, Shanghai Berry Electronic Tech. Co. Ltd., Shanghai, China) attached onto the index finger of the same hand to measure the participant's pulse signal for subsequent comparison with remotely acquired physiological signals. All measurements were taken in a temperature-controlled darkroom by a trained operator. Upon arrival, the subject was required to sit on an adjustable chair and rest for at

least 10 minutes before the measurements. For this study, ten sets of recording were taken from the healthy subject who was asked to sit at ease and rest his monitoring hand, maintaining it as motionless as possible during the recording. A soft cushion was placed under the hand to further minimize motion. The palm was exposed to the infrared light source and the distance between the camera lens and skin was approximately 450 mm. The original images were captured for 4 minutes at a rate of 200 fps with an exposure time of 4 ms, yielding raw images with 256×384 pixels. The pixels were encoded in 10 bit grayscale, allowing the camera to detect the weak pulsations of the microvascular tissue bed.

6.2.1.2 Image processing

PPG is known to be susceptible to motion-induced signal corruption. The motion modulated function introduced in Chapter 3 models the corruption of signals within raw image data due to 2D motion that is parallel to the image plane, which by its nature can be attenuated during image registration, i.e., as a pre-process. Under conditions of minor motion, the signal to noise ratio could be significantly improved via a process of spatial averaging [48]. Hence, once a set of recordings was successfully acquired, the raw image frames were divided into discrete sub-windows to produce a new set of reduced frames, where the value of each pixel in the reduced frame was set as the average of all the pixel values within each sub-window. In the present study, sub-window size was set at 8×8 pixels, which resulted in a reduced frame size of 36×48 pixels and yielded PPG signals at each pixel position across a sequence of frames. The PPG signals were then band-pass filtered using a 5^{th} order Butterworth filter. Cut-off frequencies were set at [0.5, 4] Hz to allow a wide range of heart rate measurements and to provide a relatively clear waveform for trough detection. The joint time-frequency analysis, e.g., time-frequency representation (TFR), was then performed on the iPPG signals to assess the time-varying heart rate (HR) which was obtained through averaging the HR within all the sub-windows (36×48 pixels). Historical HR estimations were used to define a maximum threshold for deviation amongst different regions. Firstly the HR was calculated from the cPPG reference signals. Successive calculations were then performed on the reduced frames where, if the difference between the current HR estimation and the reference value exceeded the threshold (6 bpm in this study which is equivalent to 0.1Hz for the HR estimation), the algorithm isolated these image regions as non-tissue or corrupt and rejected the invalid HR. For each subject, a 1 min (12000 frames) moving window was employed for the calculation with 0.5 min (6000 frames) overlap.

6.2.1.3 PRV Processing

As mentioned above (Chapter 4), time domain PRV measurements are mainly based on the statistical or geometric analysis of the lengths of intervals between successive normal pulses. For instance, the mean pulse-to-pulse (PP) intervals and the standard deviation of all PP intervals (SDPP) have been adopted for the PRV analysis in the present study. However simple these analyses are, the sympathetic and parasympathetic contributions to the HRV are not straightforward in time domain parameters. To address this problem, Akselrod and colleagues have introduced a power spectral density (PSD) analysis which provides the basic information of how power (i.e., variance) distributes as a function of frequency, and also leads to new insights in ANS evaluation [125]. There is indication in the literature that frequency domain methods should be preferred when working with short-term recordings [31], i.e., 4 minutes in the present study. Nevertheless, as a discrete event series, PPI is an unevenly sampled time series which could not be directly adopted for PSD analysis. Hence, we first interpolated PPI with cubic splines and regularly re-sampled it at 4 Hz. The power spectrum of the re-sampled PPI was then estimated using Welch's method. In practical terms, it is recommended that the duration of the recording should be about 10 times the wavelength of lowest frequency bound of the spectral component investigated [31]. Therefore, only the low frequency (LF, i.e., 0.04-0.15 Hz), high frequency (HF, i.e., 0.15-0.4 Hz), and the LF/HF ratios were calculated for analysis of the autonomic regulation. LF and HF were also expressed in normalized units, denoted as LF_{nu} = LF/(total power-VLF power) and HF_{nu} = HF/(total power-VLF power), respectively. Generally, LF is considered to be a quantitative marker for both sympathetic and vagal activities, and HF reflects vagal activity. Thus, LF/HF ratio could be regarded as an indicator of the sympathovagal balance or sympathetic modulations. The interpretation of VLF (0.003-0.04 Hz) components was not addressed in the present study because of the short duration of the recordings. In this work, post processing and analysis of both PPG and PPI signals were performed with custom software in Matlab 2010 (MathWorks, Nantik, Massachusetts, USA).

6.2.1.4 Statistical analysis

To evaluate the reliability of the iPPG system, Bland-Altman analysis [117] was performed for comparison between iPPG and the cPPG. The difference between iPPG and the cPPG was plotted against the average of both systems, as was the mean and the standard deviation (S.D.) of the differences, the mean of the absolute differences, and 95% limits of agreements (±1.96

S.D.). The Pearson's correlation coefficients and the corresponding *p*-value were also calculated to assess the HR from both systems. All analyses were performed with α (Type I error) set at 0.05 using the statistical software program SPSS for Windows, version 17.0.

6.2.2 Study 1: Results

Figure 6.2 shows an example of the PPG signals and the corresponding TFR traces, with RR, HR frequencies, and 2nd harmonic components. The region where iPPG signal was extracted is highlighted with an arrow. And the reference cPPG signal is obtained from calculating the mean value within the region of the reference LED (rectangular black box).

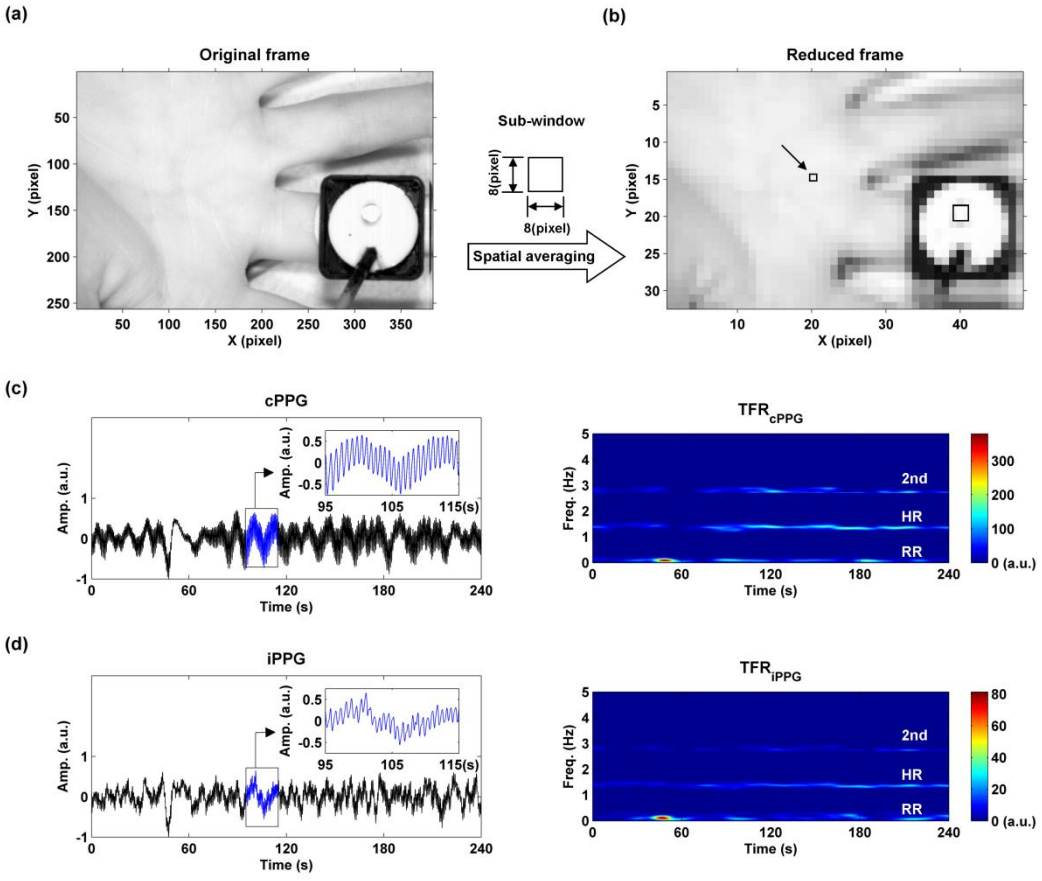

Figure 6.2 – A representative figure showing (a) original frame, (b) a reduced frame (frame 11999, t = 60 s), (c) cPPG signals and the corresponding TFR result and (d) iPPG signal and the TFR results with colour bar indicating the absolute power intensity. In the inserts in (c), plethysmographic waveform, heartbeat-related photoplethysmograms can be observed in both signals. The position from which the iPPG signal was extracted is highlighted with a black box (1×1 pixel) and an arrow while the region where the cPPG signal was obtained is indicated with a black box (3×3 pixels) in (b).

The plethysmographic information, e.g., heart & respiration rate, is clearly visible for both PPG signals (iPPG & cPPG) in the Figure 6.2 (a) inserts. Moreover, as it can be seen in the TFR plots that the oscillations of RR, HR, and 2nd harmonic component derived from iPPG signals were in excellent agreement with those obtained from the commercial pulse oximeter sensor readings. Detection of the harmonic indicates that not only the HR but also the shape of the plethysmogram were determined [48] thereby proving the practicability of remote PRV assessment.

To statistically evaluate the performance of the iPPG system and the obtained physiological parameters, Bland-Altman plots were employed in the present study to compare the agreement of plethysmographic oscillations, i.e., RR & HR, between iPPG and cPPG measurements. The comparisons of cPPG and iPPG are shown in Figure 6.3. A close agreement between the two techniques was revealed. Specifically, the mean bias ($\hat{b}$) of the respiration rate is 0.0 breaths/min with 95% limits of agreement -1.2 to 1.2 breaths/min (a) while the mean bias for the heart rate measurements is 0.1 bpm with a 95% confidence interval of -2.9 to 3.0 bpm. Significant correlation coefficients of the two physiological parameters between both measurements are revealed (Pearson's correlation for RR & HR, $r^2 > 0.95$, $p<0.005$).

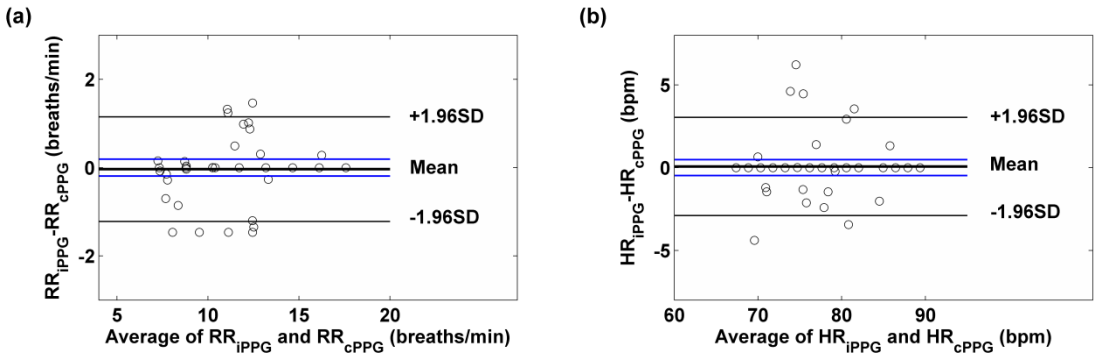

Figure 6.3 – Bland-Altman plots showing the average of the (a) RR and (b) HR measured by the iPPG and cPPG, plotted against the difference between them, with the blue line showing the confidence interval for the bias ($p < 0.01$).

As detailed before in Chapter 4 (*PRV processing* section), the PPI signal is actually not an evenly sampled signal. Hence, an interpolation technique has been employed prior to a resampling approach. An example of the PPI sequence obtained via the custom trough detection algorithm is demonstrated in Figure 6.4.

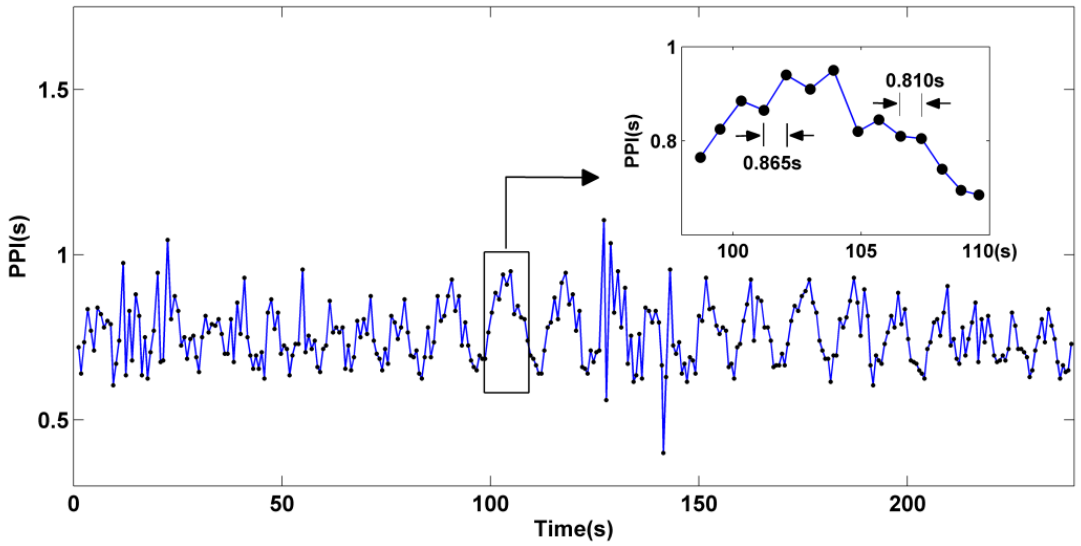

Figure 6.4 – A representative figure showing the obtained PPI signal which is formed by extracting the peaks from the troughs of the PPG waveform. In the insert the unevenly sampled characteristic is better demonstrated.

As it can be seen from the PPI sequence, a clear respiration dependent waveform is identified. Further analysis reveals that the RR calculated from the PPI agrees well with that obtained from original PPG signals (not presented). To further statistically evaluate the feasibility of the imaging PPG system in accessing the PRV, Bland-Altman plots were employed to compare the agreement of the time/frequency-domain PRV measurements between iPPG and cPPG (Figure 6.5). Table 6.1 summarises the overall results.

Table 6.2 – Overall results[†] of the PRV analysis.

	PP	SDPP	LF_{nu}	HF_{nu}	LF/HF
iPPG	0.763±0.023	0.093±0.011	0.574±0.018	0.236±0.017	2.619±0.306
cPPG	0.759±0.022	0.111±0.016	0.590±0.015	0.240±0.018	2.661±0.325
Correlation	F=0.994; p<0.001	F=0.795; p=0.006	F=0.991; p<0.001	F=0.859; p=0.0014	F=0.971; p<0.001

[†] Numbers are group average values (Mean) and standard error of the mean (SEM).

The comparison of iPPG and cPPG in PRV assessments is summarized in Table 6.1 & Figure 6.5. For instance, a significant agreement between the time and frequency domain measurements has been uncovered.

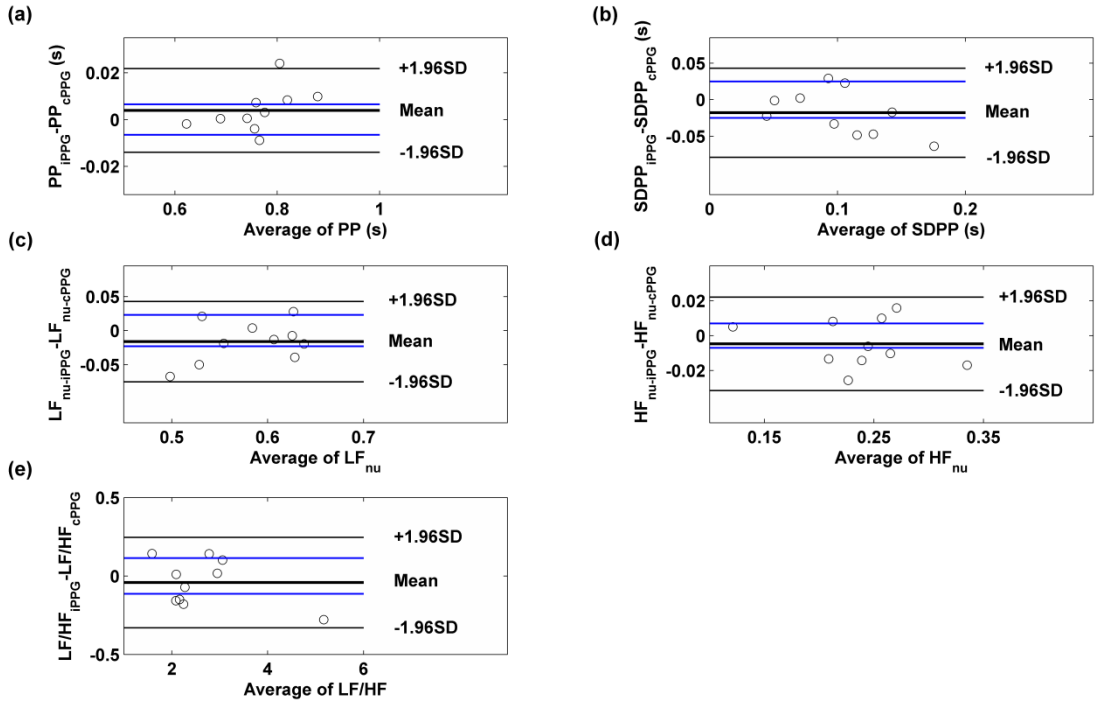

Figure 6.5 – Bland Altman plots showing the agreement of the time/frequency-domain measurements between iPPG and cPPG for (a) PP, (b) SDPP, (c) LF_{nu}, (d) HF_{nu}, and (e) LF/HF. PP: mean pulse-to-pulse intervals, SDPP: the standard deviation of all PP intervals, LF_{nu}: normalized power in low frequency range (0.04-0.15 Hz), HF_{nu}: normalized power in high frequency range (0.15-0.4 Hz). The blue lines show the confidence interval for the bias ($p < 0.05$).

The mean bias for the PP and SDPP are 0.0039 s and -0.0179 s with 95% limits of agreement -0.0140 to 0.0218 s and -0.0789 to 0.0432 s respectively. For the spectral parameters, the mean bias for the normalized LF and HF components are -0.0161 and -0.0047; the correspond 95% limits of agreement are from -0.0749 to 0.0427 and -0.0315 to 0.0220. The mean bias of their ratio is -0.0421 with 95% confidence interval -0.3308 to 0.2466. Moreover, significant correlation coefficients between both techniques are revealed in all parameters (Pearson's correlation, $p<0.01$).

6.2.3 Study 2: Results

The cardiorespiratory parameters, i.e., RR & HR were firstly statistically compared between the iPPG and cPPG measurements as shown in Figure 6.6. A great agreement between two techniques was revealed, where the mean bias of the respiration rate is 0.0 breaths/min with 95% limits of agreement -1.3 to 1.4 breaths/min while the mean bias for the heart rate is 0.0 bpm with 95% confidence interval -3.0 to 2.9 bpm. Moreover, significant correlation

coefficients of the two physiological parameters between both measurements were revealed (Pearson's correlation for RR & HR, $r^2 > 0.95$, $p < 0.001$).

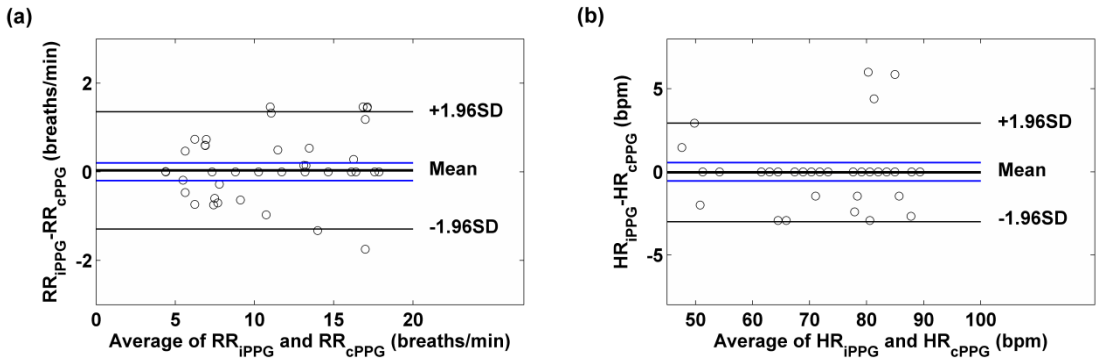

Figure 6.6 – Bland Altman plots showing the average of the (a) RR and (b) HR measured by the iPPG and cPPG, plotted against the difference between them, with the blue lines showing the confidence interval for the bias ($p < 0.01$).

The overall time and frequency domain PRV measurement results are summarized in Table 6.3. Significant correlation has been revealed between the results from these two techniques. Further statistical results were evaluated via Bland-Altman plots and demonstrated in Figure 6.7.

Table 6.3 – Overall results[†] of the PRV analysis for 10 volunteers.

	PP	SDPP	LF_{nu}	HF_{nu}	LF/HF
iPPG	0.902±0.057	0.079±0.013	0.477±0.033	0.288±0.017	1.694±0.152
cPPG	0.889±0.054	0.077±0.014	0.488±0.032	0.285±0.020	1.754±0.155
Correlation	F=0.987; p<0.001	F=0.723; p=0.028	F=0.954; p<0.001	F=0.973; P<0.001	F=0.859; P=0.003

[†] Numbers are group average values (Mean) and standard error of the mean (SEM).

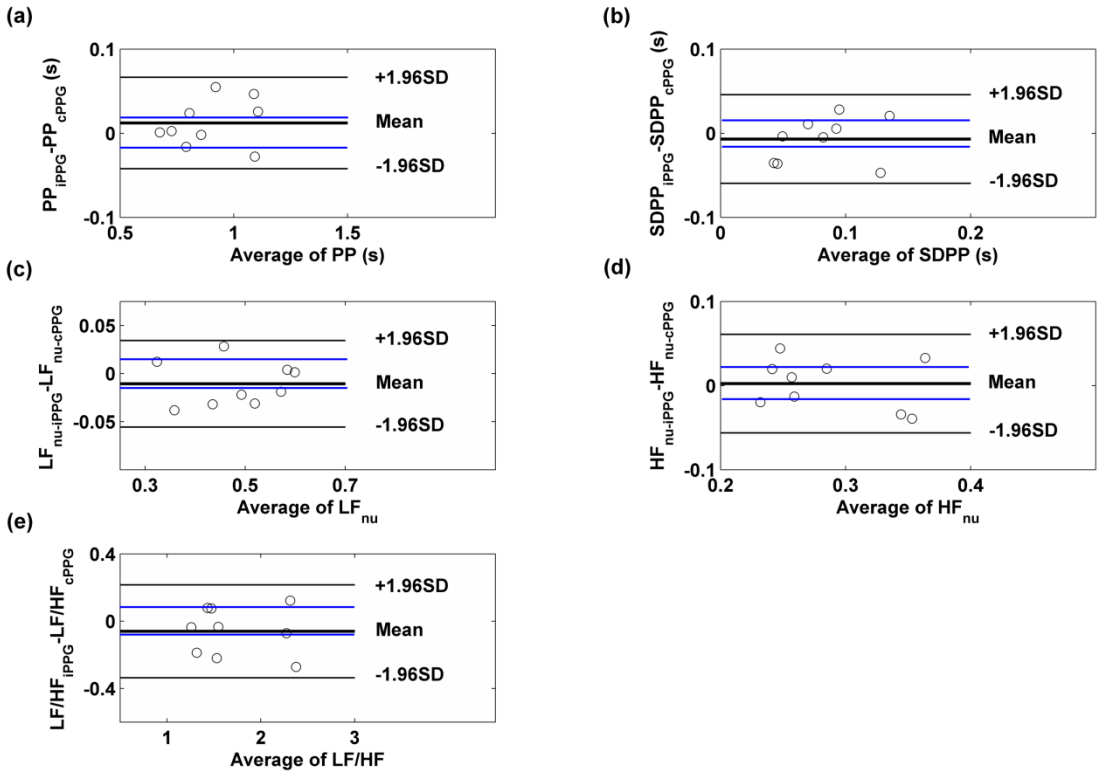

Figure 6.7 – Bland Altman plots of *Study* 2 showing the agreement of the time/frequency-domain measurements between iPPG and cPPG for (a) PP, (b) SDPP, (c) LF_{nu}, (d) HF_{nu}, and (e) LF/HF, with the blue lines showing the 99% confidence interval of the bias.

The mean bias for the PP and SDPP are 0.0121 s and -0.0069 s with 95% limits of agreement -0.0422 to 0.0664 s and -0.0595 to 0.0457 s respectively. The mean bias for the normalized LF (LF_{nu}) and HF (HF_{nu}) components are -0.0106 and 0.0023; the correspond 95% limits of agreement are from -0.0557 to 0.0344 and -0.0563 to 0.0609. The mean bias of their ratio is -0.0607 with 95% confidence interval -0.3371 to 0.2156.

6.3 DISCUSSION

Recent published work has demonstrated the feasibility of the remote autonomic nervous system assessment technique via accessing the pulse rate variability information using a webcam [53]. However, several techniques and practical issues have not been fully evaluated. For instance, the frame rate of the webcam was only 15 fps which is much lower than the standard for the accurate measurements (> 100 Hz in any case) [31]. Besides, the duration for the PRV calculation is not long enough for the spectral analysis, i.e., as recommended at least 10 times the wavelength of lowest frequency bound of the spectral component investigated.

Hence, if the LF (0.04-0.15 Hz) is the band of interest, a duration of original signal should be around 4 min. Therefore, the results in [53] are far from conclusive and some additional research is still needed. In the present study, we have adopted an imaging PPG platform which is capable of monitoring the PPG signals with a fast sample frequency and high sensitivity. The performance of the iPPG system in accessing PRV information has been evaluated by comparing it with the readings from a contact PPG sensor. Strong correlation and good agreement between these two techniques for PRV measurements show confidence of iPPG system in the remote monitoring of physiological information from the autonomic nervous system.

Ten sets of recordings were obtained from one subject in successive four working days (*Study* 1) to evaluate the feasibility of the iPPG system in high speed. As it can be seen in Figure 6.2, a clear PPG signal has been revealed from a small region (1×1 pixel in the reduced frame which is equivalent to 8×8 pixels in the original frame). The novel reference PPG system has also shown its feasibility in PPG signal monitoring. Further time frequency analysis shows an excellent agreement of respiration rate, heart rate, and 2^{nd} harmonic components, proving the practicability of the iPPG system in detection of the cardiovascular parameters. Detection of the harmonics indicates that both the HR and the shape of the plethysmogram were determined and well preserved, thus facilitating and securing the following PRV measurements. Further statistical analysis (Bland-Altman plot) showed that the physiological parameters obtained from the iPPG system agreed well with the contact-sensor, i.e., maximum difference was about 3 bpm for heart rate and 1.2 breath/min for respiration rate. As mentioned in Chapter 5, the clinically acceptable error depends on the application, i.e., for an adult patient with a HR over 100 bpm to be considered as tachycardia, the iPPG system offers a difference of less than 3% error. The initial evaluation trial has proven the feasibility of the iPPG system in monitoring the plethysmographic information in a fast mode, thereby facilitating and supporting the following pulse rate variability investigations.

In contrast to various well established QRS detection techniques in HRV analysis (for a review, see [96]), there are fewer publications pertaining to the characterization of PRV signals. Hence, to obtain the pulse-to-pulse interval (PPI) sequences, a custom built wavelet transform based semi-automated trough detection algorithm has been developed and employed prior the PRV analysis. Through adopting the short-window moving HR as the threshold, the present trough detection technique could achieve an accuracy of >95% before

the manual verification approach, which resulted in 100% accuracy. Once the PPI signals were obtained, both the time and frequency domain parameters have been calculated and evaluated for both measurements, e.g., iPPG & cPPG. Statistical results presented strong correlation (p<0.01 for all measurements) and good agreement between these two methods for PRV assessments, indicating that the iPPG system can obtain information about the autonomic nervous system.

The evidence obtained from *Study* 1 prompted further evaluation of the stability and reproducibility of the iPPG system in PRV assessments. Hence, 10 subjects (aged 21-65 years) participated in an additional experiment (*Study* 2). One subject was in the condition of illness and the recorded images present a poor signal to noise ratio; hence, a total of nine sets of meaningful recordings were obtained and analyzed in this study. The cardiovascular variables such as respiration and heart rate were also calculated prior the PRV analysis to appraise the signal quality and the stability of the iPPG system. As it can be seen in Figure 6.6, a high agreement was identified between the iPPG and cPPG measurements, i.e. $\hat{b}_{RR}$= 0.0 ± 0.07 breaths/min and $\hat{b}_{HR}$= 0.0 ± 1.5 bpm. More importantly, the strong correlation and good agreement were also obtained for the PRV parameters, thereby providing further support for the reliability and reproducibility of the iPPG technique in remotely assessing the autonomic nervous system.

No approach is immune to all artefacts, thus, it is important to recognize the limitations of the present study. One main source of artefacts arises from the motion artefact which might easily occur since the sensor has no contact with the skin. Consequently leading to corrupted signals and costing problems for the following processing. Based on our experience in iPPG signal recording and the findings of previous iPPG studies, facial PPG signals are typically stronger than those from other anatomical locations [47, 48, 53, 76]. However, without support, involuntary movements of the head are inherently complex which would require additional effort in motion compensation/attenuation. The primary application introduced in this study is to validate the feasibility, reliability and reproducibility of the iPPG technique in assessing the physiological information about the ANS, e.g., PRV. Therefore, in the present study, images were recorded from the palm as an easily verified approach that has widely been adopted for iPPG studies. The spatial averaging approach was used as the motion attenuation technique in the present work. Nevertheless, the use of sophisticated and reliable motion compensation

techniques [76] is encouraged for further attempts to replicate these findings in different anatomical locations, e.g., face.

Respiration causes variation in the peripheral circulation, making it possible to monitor breathing using a PPG technique. The low frequency respiratory induced intensity variations in the PPG signal are well documented [4, 130, 131]. Typically, it is considered that such variations includes contributions from the venous return to the heart caused by alterations in intra-thoracic pressure and also changes in the sympathetic tone control of cutaneous blood vessels [4]. In a study by Johansson and Oberg [130] the respiratory induced signal was digitally extracted from forearm PPG measurements. In the present study, the low frequency components extracted from both PPG signals exhibit comparative functional characteristics, suggesting the feasibility of the iPPG system in detecting the important respiration information. One recent study [132] demonstrated that the respiratory induced variations in the finger PPG waveform could be uncovered even when an arm blood pressure cuff was pressurized to well above the systolic blood pressure, providing further evidence for the usefulness of PPG technique in physiological monitoring of breathing interval.

Originating from the pulse wave and governed by the cardiac cycle, PRV might be a surrogate of HRV. Compared to the ECG acquisition which normally requires several sensors attaching on the body, PPG signal recording is easy, simple, and convenient. However, there are few studies pertaining to the practicability and reliability of PRV analysis, with conflicting results. Particularly, Constant and colleagues reported an overestimation of HR respiratory fluctuation from PRV estimation, especially in standing healthy subjects [127]. In contrast, Nitzan and co-workers demonstrated the variability of the PPG parameters in assessment of the function of autonomic nervous system both in healthy subjects and diabetic patients [128], as well as one recent iPPG study that has provided further support of PRV as potential surrogate of HRV [53]. The results presented in this study have therefore showed promise of iPPG technique in assessing multiple physiological measurements with a fast sample frequency, enabling autonomic control of the heart to be studied. The last two decades have witnessed the recognition of a significant relationship between the ANS and cardiovascular mortality, including sudden cardiac death. One recent study has demonstrated the time- and frequency-domain measures of HRV in 763 elderly subjects, and the relationship of these HRV measures to all-cause mortality during 4 years of follow-up [133]. However, the normal HRV standards for various age and gender subsets are still missing. Hence, larger prospective population

studies with longitudinal follow-up are needed [134]. Such studies might be facilitated via employing imaging PPG technology. The emerging field of imaging PPG technologies offers some nascent opportunities in effective investigation and interpretation of the autonomic nervous system. Further studies are needed to assess the performance and to appraise the accuracy of the iPPG based PRV using the gold standard (ECG based HRV) with a larger number of subjects and in selected patients.

Healthy cardiac function is characterized by irregular time intervals between consecutive heart beats. This variability, namely heart rate variability (HRV), has proved its usefulness in assessing the cardiorespiratory control system and the sympathetic and parasympathetic function of the autonomic nervous system (ANS). Pulse rate variability (PRV), a potential surrogate of HRV, has been remotely obtained via a fast imaging PPG platform. This chapter verified the feasibility and reproducibility of the iPPG system for the recovery of clinically important PRV information. The outcome of this study thereby leads to a new avenue for noncontact and convenient monitoring for the ANS.

7 CONCLUSIONS & FUTURE WORK

Imaging photoplethysmography (iPPG) – a remote, noninvasive and noncontact optical technique – has been developed and utilized in this study to effectively assess the physiological parameters which might provide valuable information for appraising the human cardiovascular regulation. The output of this study provides further support for the iPPG technique in remote physiological assessments. Future work is also required in: further development of motion artifacts attenuation technique, remote blood oxygen saturation measurements, nonlinear analysis of PRV, and remote pulse transit time assessments.

7.1 CONCLUSIONS

The main purpose of this thesis is to elucidate effective approaches to physiological assessment using imaging photoplethysmography (iPPG) in order to assess the practicability of this technology in the remote monitoring of specific physiological parameters. To achieve this purpose, the designated experimental protocols were implemented to validate key physiological parameters, i.e., heart rate, respiration rate, pulse rate variability, and blood perfusion. Statistical analyses show a strong correlation and close agreement between the results from the iPPG system and the gold standard cPPG, suggesting the reliability of the iPPG system in providing physiological assessments. The main contributions of this thesis can be summarized as follows:

(1) Revised opto-physiological engineering model to interpret physiological phenomena;
(2) A motion compensation based image registration methodology to improve the signal to noise ratio and reliability of extracted signals;
(3) Verification of iPPG as an effective method for non-contact physiological assessment of heart rate, pulse rate variability and respiration rate containing meaningful data for clinical assessment;
(4) Improvement of iPPG system methodology to reach a higher performance standard.

7.1.1 Revised opto-physiological engineering model

As detailed in Chapter 3, a revised opto-physiological engineering model has been introduced for the reflectance iPPG technique based on the behavior of light propagation through the skin, which is governed by a number of fundamental optical phenomena. A model for signal quality in an iPPG system has been introduced and discussed. Here, motion artifact was considered as a function (f_m) modulating the obtained signals. Under this assumption, the motion artifacts cancellation/attenuation can be found as the inverse function of the motion corruption (f_m^{-1}). After motion compensation of the obtained iPPG recordings, the opto-physiological model provides a step towards the theoretical estimation of physiological parameters, e.g., pulse rate, pulse rate variability, perfusion map, and pulse transit time, which has potential applications in future simulation studies.

7.1.2 A novel motion-compensation methodology

As detailed in Chapter 2 and echoed in Chapter 5, PPG signal is susceptible to motion-induced signal corruption, making motion artifact removal or attenuation one of the most challenging issues in iPPG signal processing and constraining the physiological monitoring capabilities of the technique in real application environments. In recent pioneering iPPG studies, major attention has been paid to the acquisition of the PPG signals in order to validate the practicability of iPPG technologies. Motion artifacts were not carefully dealt with and the associated PPG setups were usually operated under conditions that required the subjects to be motionless. One recent study reports attempts to attenuate the motion artifacts via automatic face tracking and blind source separation [47]. However, the motion artifacts evaluated in such study were typically slow and originated from relatively small movements. A methodology, which is capable of attenuating the artifacts in conditions of significant motion, however, is still lacking. In the present study, a motion compensation based image registration technique has been introduced and has led to new insights for reliable physiological assessments. Specifically, motion artifacts occurring in the recording are mainly attributed to the movements between the camera and the tissue manifesting as distortion and shift in the images, where such an effect can be attenuated via motion compensation techniques. The results in Chapter 5 demonstrated that the employed 2-D cross correlation based image registration technique can compensate most motion artifacts, thereby increasing the signal to noise ratio and leading to new avenues for the non-contact sensing of vital signs, with clear applications in triage and sports training.

7.1.3 Remote assessment of pulse rate variability

As detailed in Chapter 6, with the help of the fast digital camera technologies, our iPPG system is capable of monitoring some physiological parameters which to a level that has not been previously achieved in the most pioneering systems, e.g., pulse rate variability (PRV) and pulse transit time (PTT). The technical similarity between these two parameters is the requirement of a relatively high time-domain resolution. For instance, according to the guideline of the heart rate variability measurements that are typically obtained from ECG signals, the sample frequency should be above 100 Hz in any condition to guarantee the accuracy of the analysis. It has been detailed in Chapter 2 that the AC component of the PPG pulse is synchronous with the beating heart, which provides the biological endorsement to surrogate HRV with PRV – the pulse-to-pulse alteration in pulse rate. However, there are few

studies on the practicability and reliability of the PRV analysis and they show conflicting results. This research comprises an in-depth assessment of PRV information acquired via the iPPG technique. The results in Chapter 6 indicate the practicability for measurement of PRV via iPPG, extending and showing the feasibility of the novel iPPG system in the remote assessment of clinically meaningful physiological parameters.

7.1.4 Reference synchronisation system

Nowadays, the contact PPG sensor is still the gold standard for measurements of pulse rate, heart rate, and blood oxygen saturation. To evaluate the performance of the novel iPPG technique, it is necessary to employ a cPPG based validation signal. This approach has been widely accepted in pioneering iPPG studies. Normally, the commercial experimental digital camera could not provide an output trigger signal. Hence, it was difficult to synchronize the recorded images with the cPPG signals. In the present study, a cPPG signal driven reference synchronization system has been developed to overcome this problem (Chapter 4). Specifically, the cPPG signal was obtained from the original PPG sensor; the signal was then transferred into a custom-built LabVIEW function (see appendix C) that utilizes the cPPG signal as an input, filtering, shifting, and adopting it as a driven output signal for a red LED placed within the iPPG system's field of view. In this case, the light intensity of the LED was synchronized with the ac component of the cPPG signal. Hence, during the video recording, the iPPG signals were obtained along with a standard cPPG signal as a reference. However successful, one drawback of the existing reference system is the lack of time domain information between the obtained signals (cPPG & iPPG) as the iPPG signal and the reference signal contained a time-delay due to the time taken for the cPPG signal to be processed and output. This posed a limitation to the calculation of PTT, i.e., the time difference between the iPPG and cPPG signal could not be considered as a valid PTT estimation.

7.1.5 System improvement of iPPG

As a recent introduced technique, a standard for the imaging PPG system design has not been established. Among those existing imaging PPG systems, some adopt ambient light as the light source. Though convenient and successful in physiological assessments, the ambient light is arguably not recommended for clinical applications. For instance, the wide wavelength band would make the blood oxygen saturation information almost impossible to

obtain and the relatively unstable light intensity during the recording would pose a significant engineering issue. In the present study, two different iPPG designs have been evaluated (Chapter 4), e.g., a custom-built ring-light integrated iPPG and commercial NIR light source iPPG system. Briefly stated, the ring light design yielded integral and stable iPPG signal detection while the commercial NIR light source demonstrated superior of power and uniformity. These two designs lead to new insights into the standardization of iPPG system design. Several aspects deserve attention:

1) The wavelength of the light source should be suited to the camera QE and according to the tissue optical properties, e.g., optical water window, penetration depth, and isobestic effect;
2) The light intensity of the light source should be as uniform as possible to provide accurate information of blood perfusion mapping;
3) A minimum of two wavelengths together with an additional light source control circuit are necessary for acquisition of the blood oxygen saturation information.
4) To achieve faster sampling frequencies or longer datasets, monochrome cameras are recommended.

7.2 FUTURE WORK

The present iPPG system which couples of an infrared light source and a fast CMOS experimental digital camera shows significant achievements in the remote monitoring of a variety of physiological parameters, e.g., heart rate, respiration rate, blood perfusion, and pulse rate variability. The system facilitates non-contact physiological assessment and can enable front-line-clinicians to comfortably and confidently cope with a range of situations. More importantly, an iPPG based opto-physiological engineering model has been introduced in the present study, which not only demonstrates its practicability in improving the signal quality, but also suggests future mathematical/theoretical directions of research towards increasingly reliable measurements. Thus, the correlation between the empirical measurements and the corresponding results from the simulation engineering model is an aspect that warrants further investigation. Though successful, the novel imaging PPG platform would benefit from the following improvements: Firstly, through modifying the light-source and control circuit, the blood oxygen saturation information could be easily obtained via the existing iPPG system. Meanwhile the existing engineering model could be extended to account for SaO2. Secondly, different image registration techniques should be carefully considered for motion attenuation according to the source of inaccurate registration and the practicability for long-term monitoring. Thirdly, instead of performing simple tasks, e.g., motion attenuation, time-frequency analysis, and data segmentation, the existing software platform should be capable of providing an intuitive graphical user interface for clinical applications. Besides, though proving its ability and reliability in accessing the pulse rate variability signals, some sophisticated nonlinear approaches should be employed in the present iPPG platform for comprehensive investigation of the autonomic nervous system. Finally, the present iPPG system is also capable of recording the physiological images at a relatively fast speed, e.g., 500 frame per second, which provides accurate time-domain resolution. This significant advantage against the existing iPPG setups makes the novel iPPG system a good candidate in the remote assessment of physiological parameters, e.g., pulse transit time (PTT) & pulse wave velocity (PWV). Though obstacles to develop a clinically useful device remain, the allure of a noncontact imaging PPG and the ability to measure cardiovascular function by non-contact means are strong.

7.2.1 Blood oxygen saturation mapping

The human body can survive without water or food intake for days or weeks, but it cannot

survive for more than a few minutes without oxygen. The capacity to provide real-time knowledge of arterial oxygen saturation makes pulse oximetry effective and attractive at giving an early warning for hypoxia. Nowadays, the contact PPG sensor has become a standard SaO_2 monitoring technique in various clinical applications. Technically, SaO_2 can be determined through shining red and then near infrared light into vascular tissue with rapid switching between both wavelengths. Due to the difference in the absorption coefficients of HbO_2 and Hb at these two wavelengths, SaO_2 could be estimated from the amplitude ratio of AC signals and their corresponding DC components.

Light-source control circuit: The iPPG system could be extended to SaO_2 assessments by introducing a suitable dual-wavelength light source. Together with the light source, a light-source control circuit should also be carefully designed. The ring-light control circuit (Figure 4.5) described in Chapter 4, could be modified for the SaO_2 assessment. Figure 7.1 presents a schematic diagram of the control circuit (a) and a presentation of the driven/trigger signal (b).

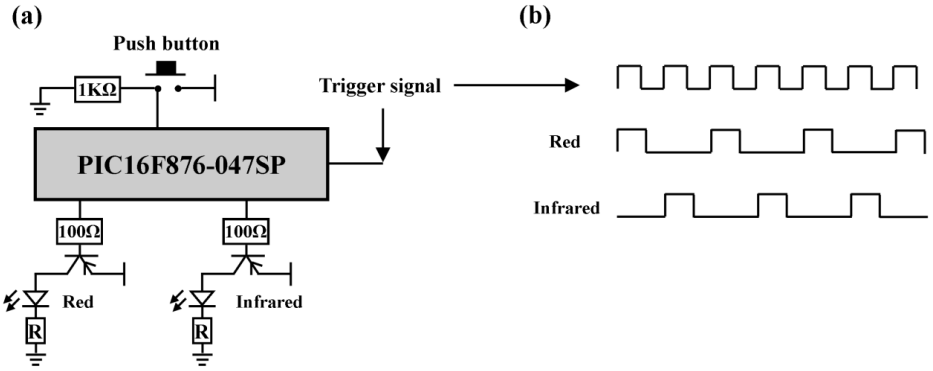

Figure 7.1 –Schematic diagram of the control circuit for a two-wavelength light source (a) and timings of the driven signals (b). The camera capture clock could be employed as the trigger signal. Ideally, the 'on' period should be slightly longer than the camera exposure time.

SaO_2 Engineering model: Oxygen saturation can be theoretically understood as the percentage of the total haemoglobin in the blood that is oxy-haemoglobin: $SaO_2 = (HbO_2)/(Hb + HbO_2) \times 100\%$. Pulse oximetry is the use of PPG for *in-vivo* monitoring of oxygen saturation in haemoglobin. It uses PPG signals at two different wavelengths to deduce the ratio of oxygenated to reduced haemoglobin in the blood. A coefficient that is commonly used in pulse oximetry is the ratio of ratios R, which is defined as the ratio of the normalised absorbances of blood at two illuminating wavelengths:

$$R = \frac{\mu_{a,b}(\lambda_1)}{\mu_{a,b}(\lambda_1)} = \frac{S\mu_{HbO_2}(\lambda_1) + (1-S)\mu_{Hb}(\lambda_1)}{S\mu_{HbO_2}(\lambda_2) + (1-S)\mu_{Hb}(\lambda_2)} \quad [7.1]$$

Thus the clinically significant oxygen saturation S can be determined from R and the effective absorbance of oxyhemoglobin and deoxyhemoglobin at the two wavelengths:

$$S = \frac{R\mu_{Hb}(\lambda_2) - \mu_{Hb}(\lambda_1)}{R\big(\mu_{Hb}(\lambda_2) - \mu_{HbO_2}(\lambda_2)\big) - \big(\mu_{Hb}(\lambda_1) - \mu_{\mathrm{HbO_2}}(\lambda_1)\big)} \quad [7.2]$$

It is common practice to assume that the intensity variation in a PPG signal is solely due to the pulsation of arterial blood. Under this assumption, the empirical definition of the clinically significant ratio of ratios R for wavelength λ_1 and λ_2 is:

$$R(\lambda_1, \lambda_2) = \frac{I_{ac,peak}(\lambda_1)/I_{dc}(\lambda_1)}{I_{ac,peak}(\lambda_2)/I_{dc}(\lambda_2)} \quad [7.3]$$

Equation 3.12 is then decomposed into analogous static and peak dynamic attenuations OD_{dc} and OD_{ac}:

$$OD_{dc} = -\big(\mu_{a,t}d\big(\mu_{s,t}^{'}\big) + \mu_{a,b}d(\mu_{s,b}^{'})\big) \quad [7.4]$$

$$OD_{ac,peak} = \varepsilon\mu_{a,b}d(\mu_{s,b}^{'}) \quad [7.5]$$

After converting the optical density into static and peak dynamic intensities I_{dc} and $I_{ac,peak}$, the ratio of one wavelength could be obtained:

$$\frac{I_{ac,peak}(\lambda_1)}{I_{dc}(\lambda_1)} = exp\left(\mu_{a,b}d\big(\mu_{s,b}^{'}\big)(1+\varepsilon) + \mu_{a,t}d\big(\mu_{s,t}^{'}\big)\right) \quad [7.6]$$

which is independent of the detected source light intensity. Therefore a new equation for R could now be derived:

$$R(\lambda_1, \lambda_2) = \frac{exp\left(\mu_{a,b}(\lambda_1)d\left(\mu_{s,b}^{'}(\lambda_1)\right)(1+\varepsilon) + \mu_{a,t}(\lambda_1)d\left(\mu_{s,t}^{'}(\lambda_1)\right)\right)}{exp\left(\mu_{a,b}(\lambda_2)d\left(\mu_{s,b}^{'}(\lambda_2)\right)(1+\varepsilon) + \mu_{a,t}(\lambda_2)d\left(\mu_{s,t}^{'}(\lambda_2)\right)\right)} \quad [7.8]$$

Together with the knowledge of the effective absorbance at the two wavelengths, it is possible to determine oxygen saturation S through Equation 7.2.

7.2.2 iPPG Image registration

The image registration approach within the software platform for the iPPG system has been closely studied in this thesis. However, as discussed in Chapter 5, the 2-D cross-correlation based method could only attenuate or cancel the planar motion while in a real environment the motion could be more complex, e.g., in the exercise experiment the typical motion included lateral tilting of the head and mild leaning of the body and head towards or away from the camera due to deep breathing. These involuntary motion artifacts would trigger different levels of distortion in the recording images and would not be completely removed through 2-D cross correlation technique. With the development of the computer science and image processing technologies, more sophisticated and accurate image registration techniques are encouraged for future attempt to further increase the signal quality. For instance, the automated face recognition techniques have been widely employed in various areas, e.g., security. Such a method could be adopted to account for the closer/further movement (Z-axis scaling compensation), thereby facilitating the attenuation of the 3-D motion artifacts.

7.2.3 iPPG system improvement

The further development of the existing software platform also deserves attention. For instance, the core of the present software platform is the motion attenuation, image segmentation, image reduction via averaging, PPG signals filtering and acquisition of fundamental physiological parameters (e.g., heart rate, respiration rate, & pulse rate variability). Moreover, the semi-automated software platform requires the feedback from the operator to increase the accuracy, thereby limiting its applicability and reproducibility. For instance, the 2-D cross-correlation based motion attenuation technique requires a template to function. As detailed in Chapter 2, this template should contain small local features which are invariant to shape and scale. Hence, an edge detection algorithm is a subject of future studies. Besides, as shown in Chapter 5, the obtained physiological waveforms are not constant in the extracted independent components under different conditions. Automatic access and analyze of these plethysmograms requires careful consideration. Finally, for broad applications of the iPPG techniques, a software platform with a graphical user interface *(GUI)* is necessary, both for research and for exploring the user needs in the context of a functional and fully developed end-product.

7.2.4 Nonlinear PRV analysis – Detrended Fluctuation Analysis (DFA)

Detrended Fluctuation Analysis (DFA), as first introduced in the 1990s for investigating the correlations in nucleotide sequences [135], is an algorithm widely used to determine fractal long-range correlations in physiological signals. Its application to heart rate variability (HRV) has proven useful in distinguishing healthy subjects from patients with cardiovascular disease [136, 137]. The detail of the DFA can be found in [136]. Briefly stated, signals exhibiting fluctuations whose distribution obeys a power law over a broad range of frequencies are scale invariant and usually referred to as fractal. Fluctuation (F) in these signals could be expressed as a function of the time interval (n) over which they are observed according to the formula:

$$F(n) = pn^{\alpha} \qquad [7.9]$$

where p is a constant of proportionality and α is scaling exponent that depends on the signal correlation properties. The spatial case of $\alpha = 1$ is frequently observed in nature and is often called $1/f$ noise. Signals exhibiting $1/f$ noise are characteristic of complex dynamical systems, composed of multiple interconnected elements and functioning in far from equilibrium conditions [135]. These systems demonstrated optimal stability, information transmission, informational storage and computational power [136]. Hence, $1/f$ fluctuations are commonly considered as an indicator of the efficacy and adaptability of the system that produces them. In other cases, an uncorrelated time series yield $\alpha = 0.5$; a scaling exponent $\alpha > 0.5$ indicates the presence of correlations in the original series such that a large interval (as in HRV analysis) is more likely to be followed by another large interval, while $0 < \alpha < 0.5$ indicates anti-correlations such that large and small intervals are more likely to alternate. The special case of $\alpha = 1.5$ is obtained by the integration of highly correlated Brown noise [135]. Figure 6.1 demonstrates a representative plot of the DFA results from two subjects (normal *vs.* congestive heart failure).

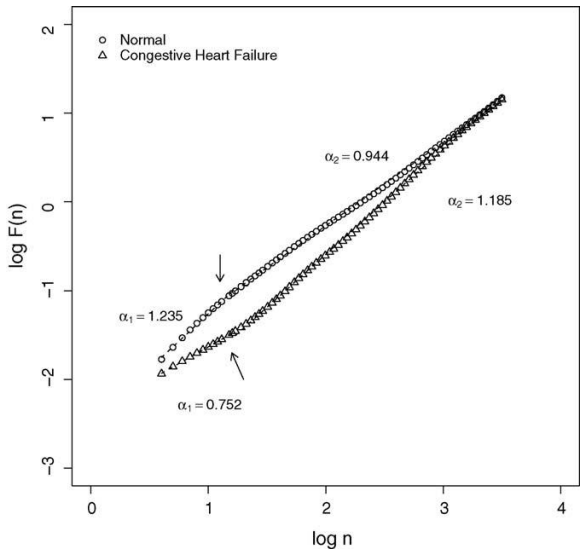

Figure 7.2 – A representative plot of the DFA analysis, showing the difference of log $F(n)$ $vs.$ log n from a healthy subject (circles) and from a subject with congestive heart failure (triangles). Arrows indicate crossovers that divide the DFA plot into two distinct scaling regions [140].

Technical details for the application of DFA in analyzing the HRV signals can be found in [135]. Briefly:

1) N-sample HRV series $\{X_k\}$ (k=1, 2, …, N) is cumulated first: $Y(i) = \sum_{k=1}^{i}(X_k - X, i=1, 2, ..., N$ where X denotes the mean value of the Xk.
2) The cumulated integration series $\{Y(i)\}$ is then divided into $N_s = [N/n]$ ($[N/n]$ denotes the integer part of the quotient N/n) non-overlapping bins of equal size n (also called time scale). Then, the detrended time series $\{Y(i)\}$ is obtained by subtracting the local trend, e.g., the least-squares fit in the bin, from $\{Y(i)\}$ to remove the non-stationary artifacts.
3) The average fluctuations $F(n)$ at scale s is then obtained:

$$F(n) = \frac{1}{N_n}\sum_{i=1}^{N_n} Y_n^2(i) \qquad [\mathbf{7.10}]$$

If a long-range correlation exists in an HRV series, as discussed before, a power-law relation will be found between the fluctuation function $F(n)$ and time scale n: $F(n) = pn^{\alpha}$. The algorithm is then repeated over a range of bin size to provide a relationship between the mean fluctuation $F(n)$ as a function of bin size n. Normally, $F(n)$ will increase as box size n becomes larger. And according to Equation $\mathbf{7.10}$, a linear relationship on a log-log graph indicates the presence of scaling characterized by the scaling exponent α. Since previous

studies have shown that this method provides a powerful approach to PRV analysis and is therefore a topic of future study.

7.2.5 Pulse transit time and pulse wave velocity

The assessment of arterial stiffness is clinically important due to its strong connection with cardiovascular morbidity and mortality. Moreover, objective assessment of vascular aging could provide valuable information about hypertension, a risk factor for stroke and heart disease. However, the study of large artery dynamics is inherently difficult because of the pulsatile nature of blood flow, the complex structure of the vessel walls, and the continually changing tone of the smooth muscle component. From the available methods to assess arterial stiffness, pulse wave velocity (PWV) has emerged as the gold standard method because of its relative ease in determination, its perceived reliability, and most importantly because of the large body of evidence demonstrating its association with incident cardiovascular disease, independently of traditional risk factors and in various populations (for a review, see [141]). As detailed in Chapter 2, the relationship between the arterial stiffness and PWV could be obtained via Bramwell-Hill formula [72, 142]:

$$\mathrm{PWV} = (\rho D)^{-1/2} \qquad [\mathbf{7.11}]$$

where ρ is the blood density and D is the arterial stiffness/distensiblity. Increasingly, arterial stiffness measures are included both in the routine clinical assessment of patients and within the framework of large-scale clinical studies. The PTT – the time it takes a pulse wave to travel between arterial sites – is inversely related to the PWV [143]. Typically, the time difference between the R-wave of the electrocardiograph (ECG) and the onset time of the corresponding PPG pulse is employed in PTT estimation. As a time domain estimation, PTT measurements need a relatively fast sample frequency for accurate time-domain resolution (>200Hz). This specific requirement constrains the development of remote PTT assessment since the experimental cameras employed in pioneering iPPG studies have a sample rate below 50 fps.

For better understanding the background of the PTT assessment, it is worth reviewing the existing PPG-based PTT estimation. There are only a few studies that have been conducted to monitor the transit time via contact PPG sensors. For instance, Nitzan and colleagues have revealed a decreased PTT as a function of the subject's age and systolic blood pressure [28]. Similar results of an age-dominated effect on PTT have also been revealed by Allen and

Murray [29]. However, the transit time within these two studies were estimated via identifying the time difference between the ECG R wave and foot of pulse at finger/toe/ear. In this definition, the PTT actually covers the transit time for the pulse to travel from heart to capillaries, thereby indirectly linking the PWV information. To address this problem and to appraise the distensiblity of the main arteries, a novel experimental protocol has been introduced. In the arterial tree, the posterior intercostal arteries are a potentially ideal measuring site by merit of their direct connection with the aorta (Figure 7.3). As mentioned above in the revised engineering model (Chapter 3), with two carefully chosen ROIs (assisted via other imaging techniques, i.e., X-ray), the PTT along the intercostal arteries could be obtained, consequently triggering the calculation of the PWV within the aorta under the simple assumption that the transit time for the pulse wave travel from the aorta to the microvascular bed is equal for both windows.

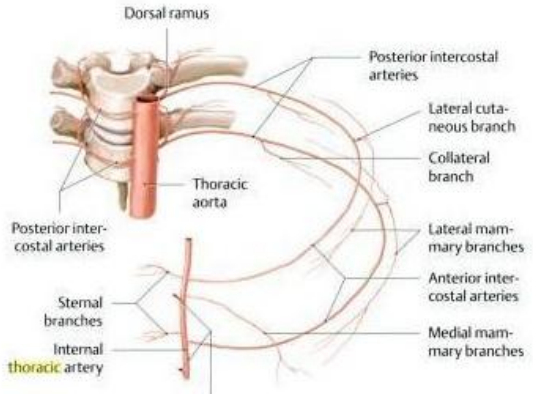

Figure 7.3 – The anatomic structure of the thorax arteries (image courtesy of http://anatomytopics.wordpress.com).

The iPPG system in the present study adopts a fast CMOS monochrome digital camera capable of capturing images at a fast speed, i.e., 500 fps at an image size of 512×512 pixels, thereby offering a nascent opportunity in remote PTT measurement. More importantly, the imaging PTT technique could not only evaluate the arterial stiffness but could also provide information regarding PTT propagation. Therefore, a further study is needed to assess the feasibility and practicability of the present iPPG system in accessing the PWV and appraising the arterial stiffness.

REFERENCES

[1] A. Hertzman, and C. Spealman, "Observations on the finger volume pulse recorded photoelectrically," *Am. J. Physiol.*, vol. 119, pp. 334-335, 1937.

[2] X. F. Teng, and Y. T. Zhang, "The effect of contacting force on photoplethysmographic signals," *Physiol. Meas.*, vol. 25, no. 5, pp. 1323-1335, 2004.

[3] X. F. Teng, and Y. T. Zhang, "The effect of applied sensor contact force on pulse transit time," *Physiol. Meas.*, vol. 27, no. 8, pp. 675-684, 2006.

[4] J. Allen, "Photoplethysmography and its application in clinical physiological measurement," *Physiol. Meas.*, vol. 28, no. 3, pp. R1-39, 2007.

[5] A. A. R. Kamal, J. B. Harness, G. Irving, and A. J. Mearns, "Skin Photoplethysmography – a Review," *Comput. Meth. Programs in Biomed.*, vol. 28, no. 4, pp. 257-269, 1989.

[6] L. Douven, and G. Lucassen, "Retrieval of optical properties of skin from measurement and modelling the diffuse reflectance," *Proc. of SPIE*, vol. 3914, pp. 312, 2000.

[7] D. Jones, "Medical electro-optics: measurements in the human microcirculation," *Phys. Technol.*, vol. 18, pp. 79, 1987.

[8] E. Benfeldt, "In vivo microdialysis for the investigation of drug levels in the dermis and the effect of barrier perturbation on cutaneous drug penetration, Studies in hairless rates and human subjects," *Acta Derm. – Venereol.*, vol. 206, pp. 1-59, 1999.

[9] W. Cheong, S. Prahl, and A. Welch, "A review of the optical properties of biological tissues," *IEEE J. Quantum Electron.*, vol. 26, no. 12, pp. 2166-2185, 1990.

[10] R. R. Anderson, and J. A. Parrish, "The optics of human skin," *J. Invest. Dermatol.*, vol. 77, no. 1, pp. 13-19, 1981.

[11] P. D. Mannheimer, J. R. Casciani, M. E. Fein, and S. L. Nierlich, "Wavelength selection for low-saturation pulse oximetry," *IEEE Trans. Biomed. Eng.*, vol. 44, no. 3, pp. 148-158, 1997.

[12] R. Brinkman, and W. G. Zylstra, "Determination and continuous registration of the percentage oxygen saturation in clinical conditions," *Arch. Chir. Neerl.*, vol. 1, no. 3, pp. 177-183, 1949.

[13] I. Yoshiya, Y. Shimada, and K. Tanaka, "Spectrophotometric monitoring of arterial oxygen saturation in the fingertip," *Med. Biol. Eng. Comput.*, vol. 18, no. 1, pp. 27-32, 1980.

[14] I. V. Meglinski, and S. J. Matcher, "Computer simulation of the skin reflectance spectra," *Comput. Methods, Programs Biomed.*, vol. 70, no. 2, pp. 179-186, 2003.

[15] J. L. Reuss, "Multilayer modelling of reflectance pulse oximetry," *IEEE Trans. Biomed. Eng.*, vol. 52, no. 2, pp. 153-159, 2005.

[16] W. B. Runciman, R. K. Webb, L. Barker, and M. Currie, "The Australian Incident Monitoring Study. The pulse oximeter: applications and limitations – an analysis of 2000 incident reports," *Anaesth. Intens. Care*, vol. 21, no. 5, pp. 543-550, 1993.

[17] A. Johansson, P. A. Oberg, and G. Sedin, "Monitoring of heart and respiratory rates in newborn infants using a new photoplethysmographic technique," *J. Clin. Monit. Comput.*, vol. 15, no. 7-8, pp. 461-467, 1999.

[18] P. Tanabe, R. Gimbel, P. R. Yarnold, D. N. Kyriacou, and J. G. Adams, "Reliability and validity of scores on the Emergency Severity Index Version 3," *Acad. Emerg. Med.*, vol. 11, no. 1, pp. 59-65, 2004.

[19] Y. S. Yan, C. C. Poon, and Y. T. Zhang, "Reduction of motion artefact in pulse oximetry by smoothed pseudo Wigner-Ville distribution," *J. Neuroeng. Rehabil.*, vol. 2, no. 1, 2005.

[20] F. Hlawatsch, and G. F. Boudreaux-Bartels, "Linear and quadratic time-frequency signal representations," *IEEE Signal Proc. Mag.*, vol. 9, no. 2, pp. 21-67, 1992.

[21] J. Penaz, "Photoelectric measurement of blood pressure, volume and flow in the finger," *Digest of the 10th Int. Conf. Med. Biol. Eng.*, Dresden, pp. 104104. 1973.

[22] B. P. Imholz, W. Wieling, G. A. van Montfrans, and K. H. Wesseling, "Fifteen years experience with finger arterial pressure monitoring: assessment of the technology," *Cardiovasc. Res.*, vol. 38, no. 3, pp. 605-616, 1998.

[23] W. Chen, T. Kobayashi, S. Ichikawa, Y. Takeuchi, and T. Togawa, "Continuous estimation of systolic blood pressure using the pulse arrival time and intermittent calibration," *Med. Biol. Eng. Comp.*, vol. 38, no. 5, pp. 569-574, 2000.

[24] J. Allen, and A. Murray, "Development of a neural network screening aid for diagnosing lower limb peripheral vascular disease from photoelectric plethysmography pulse waveforms," *Physiol. Meas.*, vol. 14, no. 1, pp. 13-22, 1993.

[25] E. D. Cooke, S. A. Bowcock, and A. T. Smith, "Photoplethysmography of the distal pulp in the assessment of the vasospastic hand," *Angiology*, vol. 36, no. 1, pp. 33-40, 1985.

[26] A. P. Avolio, s. G. Chen, R. P. Wang, C. L. Zhang, M. F. Li, and M. F. O'Rourke, "Effects of aging on changing arterial compliance and left ventricular load in a northern Chinese urban community," *Circulation*, vol. 68, no. 1, pp. 50-58, 1983.

[27] P. Gizdulich, "On a non-invasive evaluation of pulse wave velocity in human peripheral arteries," *Clin. Phys. Physiol. Meas.*, vol. 5, no. 1, pp. 33-36, 1984.

[28] M. Nitzan, B. Khanokn, and Y. Slovik, "The difference in pulse transit time to the toe and finger measured by photoplethysmography," *Physiol. Meas.*, vol. 23, no. 1, pp. 85-93, 2002.

[29] J. Allen, and A. Murray, "Age-related changes in peripheral pulse time characteristics at the ears, fingers and toes," *J. Hum. Hypertens.*, vol. 16, no. 10, pp. 711-717, 2002.

[30] J. B. Dillion, and A. B. Hertzman, "The form of the volume pulse in the finger pad in health, atherosclerosis, and hypertension," *Am. Heart J.*, vol. 21, pp. 172-190, 1941.

[31] A. J. Camm, M. Malik, J. Bigger, G. Breithardt, S. Cerutti, R. J. Cohen, P. Coumel, E. L. Fallen, et. al., "Heart rate variability: standards of measurement, physiological interpretation, and clinical use," *Circulation*, vol. 93, no. 5, 1996.

[32] H. M. Stauss, "Heart rate variability," *Am. J. Physiol. Regul. Integr. Comp. Physiol.*, vol. 285, no. 5, pp. R927-931, 2003.

[33] E. H. Hon, and S. T. Lee, "Electronic evaluation of the fatal heart rate patterns preceding fatal death, further observations," *Am. J. Obstet. Gynecol.*, vol. 87, pp. 814-926, 1965.

[34] N. Charkoudian, "Skin blood flow in adult human thermoregulation: how it works, when it does not, and why," *Mayo. Clin. Proc.*, vol. 78, no. 5, pp. 603-612, 2003.

[35] M. Hahn, C. Hahn, M. Junger, A. Steins, D. Zuder, T. Klyscz, A. Buchtemann, G. Rassner, and V. Blazek, "Local cold exposure test with a new arterial photoplethysmographic sensor in healthy controls and patients with secondary Raynaud's phenomenon," *Microvasc. Res.*, vol. 57, no. 2, pp. 187-198, 1999.

[36] T. Wu, V. Blazek, H. J. Schmitt, "Photoplethysmography imaging: a new non-invasive and non-contact method for mapping of the dermal perfusion changes," *Proc. of SPIPE*, vol. 4163, pp. 62-70, 2000.

[37] J. D. Briers, "Laser Doppler, speckle and related techniques for blood perfusion mapping and imaging," *Physiol. Meas.*, vol. 22, no. 4, pp. R35-66, 2001.

[38] Y. Aizu, and T. Asakura, "Coherent optical techniques for diagnostics of retinal blood flow," *J. Biomed. Opt.*, vol. 4, no. 1, pp. 61-75, 1999.

[39] J. D. Briers, and A. F. Fercher, "Retinal blood-flow visualization by means of laser speckle photography," *Invest. Ophthalmol. Vis. Sci.*, vol. 22, no. 2, pp. 255-259, 1982.

[40] M. Li, P. Miao, J. Yu, Y. Qiu, Y. Zhu, S. Tong, "Influences of hypothermia on the cortical blood supply by laser speckle imaging," *IEEE Trans. Neural Syst. Rehabil. Eng.*, vol. 17, no. 2, pp. 128-134, 2009.

[41] J. D. Briers, G. Richards, and X. W. He, "Capillary blood flow monitoring using laser speckle contrast analysis (LASCA)," *J. Biomed. Opt.*, vol. 4, no. 1, pp. 164-175, 1999.

[42] A. K. Dunn, T. Bolay, M. A. Moskowitz, and D. A. Boas, "Dynamic imaging of cerebral blood flow using laser speckle," *J. Cereb. Blood Flow Metab.*, vol. 21, no. 3, pp. 195-201, 2001.

[43] P. Starukhin, S. Ulyanov, E. Galanzha, and V. Tuchin, "Blood-flow measurements with a small number of scattering events," *Appl. Opt.*, vol. 39, no. 16, pp. 2823-2830, 2000.

[44] C. Konak, J. Jakes, P. Stepanek, F. Petras, M. Karska, J. Krepelka, and J. Perina, "Effect of multiple light scattering on transmitted and scattered light," *Appl. Opt.*, vol. 30, no. 33, pp. 4865-4871, 1991.

[45] C. E. Riva, B. L. Petrig, R. D. Shonat, and C. J. Pournaras, "Scattering process in LDV from retinal vessels," *Appl. Opt.*, vol. 28, no. 6, pp. 1078-1083, 1989.

[46] M. Hulsbusch, and V. Blazek, "Contactless mapping of rhythmical phenomena in tissue perfusion using PPGI," *Proc. of SPIE*, vol. 4683, pp. 110-117, 2002.

[47] M. Z. Poh, D. J. McDuff, and R. W. Picard, "Non-contact, automated cardiac pulse measurements using video imaging and blind source separation," *Opt. Express*, vol. 18, no. 10, pp. 10762-10774, 2010.

[48] W. Verkruysse, L. O. Svaasand, and J. S. Nelson, "Remote plethysmographic imaging using ambient light," *Opt. Express*, vol. 16, no. 26, pp. 21434-21445, 2008.

[49] K. Humphreys, T. Ward, and C. Markham, "Noncontact simultaneous dual wavelength photoplethysmography: a further step toward noncontact pulse oximetry," *Rev. Sci. Instrum.*, vol. 78, no. 4, pp. 044304, 2007.

[50] Y. Sun, S. Hu, V. Zaorin-Peris, S. Greenwald, J. Chambers, Y. Zhu, "Detection of physiological changes after exercise via a remote optophysiological imaging system," *Proc. of SPIE*, vol. 7891, pp. 78910E1-7, 2011.

[51] D. Litwiller, "CMOS vs. CCD: maturing technologies, maturing markets," *Photon. Spect.*, vol. 39, no. 8, pp. 54-59, 2005.

[52] F. P. Wieringa, F. Mastik, and A. F. W. van der Steen, "Contactless multiple wavelength photoplethysmographic imaging, A first step toward 'SpO(2) camera' technology," *Ann. Biomed. Eng.*, vol.33, no. 8, pp. 1034-1041, 2005.

[53] M. Z. Poh, D. J. McDuff, and R. W. Picard, “Advancements in noncontact, multi-parameter physiological measurements using a webcam,” *IEEE Trans. Biomed. Eng.*, vol. 58, no. 1, pp. 7-11, 2011.

[54] Z. B. Niazi, T. J. Essex, R. Papini, D. Scott, N. R. McLean, and M. J. Black, “New laser Doppler scanner, a valuable adjunct in burn depth assessment,” *Burns*, vol. 19, no. 6, pp. 485-489, 1993.

[55] G. Cennini, J. Arguel, K. Aksit, and A. van Leest, “Heart rate monitoring via remote photoplethysmography with motion artefacts reduction,” *Opt. Express*, vol. 18, no. 5, pp. 4867-4875, 2010.

[56] B. S. Kim, and S. K. Yoo, “Motion artefact reduction in photoplethysmography using independent component analysis,” *IEEE Trans. Biomed. Eng.*, vol. 53, no. 3, pp. 566-568, 2006.

[57] C. J. James, O. Gibson, and M. Davies, “On the analysis of single versus multiple channels of electromagnetic brain signals,” *Artif. Intell. Med.*, vo. 37, no. 2, pp. 131-143, 2006.

[58] J. M. Schmitt, G. X. Zhou, E. C. Walker, and R. T. Wall, “Multilayer model of photon diffusion in skin,” *J. Opt. Soc. Am. A*, vol. 7, no. 11, pp. 2141-2153, 1990.

[59] D. Y. Churmakov, I. V. Meglinski, and D. A. Greenhalgh, “Influence of refractive index matching on the photon diffuse reflectance,” *Phys. Med. Biol.*, vol. 47, no. 23, pp. 4271-4285, 2002.

[60] V. V. Tuchin, “Tissue optics: light scattering methods and instruments for medical diagnosis,” *SPIE Press*, 2007.

[61] J. F. de Boer, T. E. Milner, M. J. van Gemert, and J. S. Nelson, “Two-dimensional birefringence imaging in biological tissue by polarization-sensitive optical coherence tomography,” *Opt. Lett.*, vol. 22, no. 12, pp. 934-936, 1997.

[62] A. Ishimaru, “Wave propagation and scattering in random media,” *New York: Academic Press*, 1978.

[63] R. Graaff, A. C. M. Dassel, W. G. Zijlstra, F. F. de Mul, and J. G. Aarnoudse, “How tissue optics influences reflectance pulse oximetry,” *Adv. Exp. Med. Biol.*, vol. 388, pp. 117-132, 1996.

[64] V. V. Tuchin, “Light scattering study of tissues,” *Physics-Uspekhi*, vol. 40, no. 5, pp. 495-515, 1997.

[65] M. Cope, D. T. Delpy, E. O. Reynolds, S. Wray, J. Wyatt, P. van der Zee, “Methods of quantitating cerebral near infrared spectroscopy data,” *Adv. Exp. Med. Biol.*, vol. 222, pp. 183-189, 1988.

[66] D. T. Delpy. M. Cope, P. van der Zee, S. Arridge, S. Wray, and J. Wyatt, "Estimation of optical pathlength through tissue from direct time of flight measurement," *Phys. Med. Biol.*, vol. 33, no. 12, pp. 1433-1442, 1988.

[67] L. Kocsis, P. Herman, and A. Eke, "The modified Beer-Lambert law revisited," *Phys. Med. Biol.*, vol. 51, no. 5, pp. N91-98, 2006.

[68] A. Duncan, J. H. Meek, M. Clemence, C. E. Elwell, L. Tyszczuk, M. Cope, D. T. Delpy, "Optical pathlength measurements on adult head, calf and forearm and the head of the newborn infant using phase resolved optical spectroscopy," *Phys. Med. Biol.*, vol. 40, no. 2, pp. 295-304, 1995.

[69] B. Chen, K. Stamnes, and J. J. Stamnes, "Validity of the diffusion approximation in bio-optical imaging," *Appl. Opt.*, vol. 40, no. 34, pp. 6356-6366, 2001.

[70] P. Shi, Y. Zhu, J. Allen, and S. Hu, "Analysis of pulse rate variability derived from photoplethysmography with the combination of lagged Poincare plots and spectral characteristics," *Med. Eng. Phys.*, vol. 31, no. 7, 2009.

[71] V. Konig, R. Huch, and A. Huch, "Reflectance pulse oximetry – principles and obstetric application in the Zurich system," *J. Clin. Monit. Comput.*, vol. 14, no. 6, pp. 403-412, 1998.

[72] E. D. Lehmann, K. D. Hopkins, and R. G. Gosling, "Aortic compliance measurements using Doppler Ultrasound – in-vivo biochemical correlates," *Ultrasound Med. Biol.*, vol. 19, no. 9, pp. 683-710, 1993.

[73] J. Zheng, S. Hu, V. Azorin-Peris, A. Echiadis, V. Chouliaras, R. Summers, "Remote simultaneous dual wavelength imaging photoplethysmography: a further step towards 3-D mapping of skin blood microcirculation," *Proc. of SPIE*, vol. 6850, pp. S8500, 2008.

[74] K. Humphreys, T. Ward, and C. Markham, "A CMOS camera – based pulse oximetry imaging system," *Proc. 27th IEEE EMBS*, vol. 4, pp. 349403497, 2005.

[75] T. Wu, "PPGI: new development in noninvasive and contactless diagnosis of dermal perfusion using near infrared light," *J. of the GCPD*, vol. 7, no. 1, pp. 17-24, 2003.

[76] Y. Sun, S. Hu, V. Azorin-Peris, S. Greenwald, J. Chambers, and Y. Zhu, "Motion – compensated noncontact imaging photoplethysmography to monitor cardiorespiratory status during exercise," *J. Biomed. Opt.*, vol. 16, no. 7, pp. 077010, 2011.

[77] "Photobiological safety of lamps and lamp systems," *BSI British Standards*, vol. BS EN 62471, 2008.

[78] L. G. Brown, "A survey of image registration techniques," *ACM Comput. Surv.*, vol. 24, no. 4, pp. 325-376, 1992.

[79] A. Rosenfeld, and A. C. Kak, "Digital picture processing, Vol. I and II," *Academic Press, Orlando, Fla.*, 1982.

[80] D. I. Barnea, and H. F. Silverma, "A class of algorithms for fast digital image registration," *IEEE Trans. Comput.*, vol. C-21, no. 2, pp. 179-186, 1972.

[81] P. Comon, "Independent component analysis, a new concept," *Signal Process.*, vol. 36, no. 3, pp. 287-314, 1994.

[82] M. E. Davies, and C. J. James, "Source separation using single channel ICA," *Signal Process.*, vol. 87, no. 8, pp. 1819-1832, 2007.

[83] C. J. James, and D. Lowe, "Extracting multisource brain activity from a single electromagnetic channel," *Artif. Intell. Med.*, vol. 28, no. 1, pp. 89-104, 2003.

[84] A Hyvarinen, "Fast and robust fixed-point algorithms for independent component analysis," *IEEE Trans. Neural Netw.*, vol. 10, no. 3, pp. 626-634, 1999.

[85] A. Papoulis, and S. U. Pillai, "Probability, random variables and stochastic processes, 4th ed.," *New York: McGraw-Hill*, 2002.

[86] A. J. Bell, and T. J. Sejnowski, "An information – maximization approach to blind separation and blind deconvolution," *Neural Comput.*, vol. 7, no. 6, pp. 1129-1159, 1995.

[87] C. J. James, and C. W. Hesse, "Independent component analysis for biomedical signals," *Physiol. Meas.*, vol. 26, no. 1, pp. R15-39, 2005.

[88] M. P. s. Chawla, H. K. Verma, and V. Kumar, "Artefacts and noise removal in electrocardiograms using independent component analysis," *Int. J. Cardiol.*, vol. 129, no. 2, pp. 278-281, 2008.

[89] T. P. Jung, S. Makeig, C. Humphries, T. W. Lee, M. J. MaKeown, V. Iraqui, T. J. Sejnowski, "Removing electroencephalographic artefacts by blind source separation," *Psychophysiology*, vol. 37, no. 2, pp. 163-178, 2000.

[90] L. De Lathauwer, B. De Moor, and J. Vandewalle, "Fatal electrocardiogram extraction by blind source subspace separation," *IEEE Trans. Biomed. Eng.*, vol. 47, no. 5, pp. 567-572, 2000.

[91] M. J. McKeown, S. Makeig, G. G. Brown, T. Jung, S. S. Kindermann, A. J. Bell, and T. J. Sejnowski, "Analysis of fMRI data by blind separation into independent spatial components," *Hum. Brian Mapp.*, vol. 6, no. 3, pp. 160-188, 1998.

[92] F Takens, "Detecting strange attractors in turbulence. In: Rand DA, Young LS, editors, Lecture notes in mathematics (Dynamical systems and turbulence, Warwick, 1980).," *Berlin: Springer*, vol. 898, pp. 366-381, 1981.

[93] S. Qian, and D. Chen, "Joint time-frequency analysis," *IEEE Signal Proc. Mag.*, vol. 16, no. 2, pp. 52-67, 1999.

[94] M. Unser, and A. Aldroubi, "A review of wavelets in biomedical applications," *Proc. IEEE*, vol. 84, no. 4, pp. 626-638, 1996.

[95] W. L. Haskell, I. M. Lee, R. R. Pate, K. E. Powell, N. Steven, B. A. Franklin, C A. Macera, G. W. Heath, P. D. Thompson, A. Bauman, "Physical activity and public health: updated recommendation for adults from the American College of Sports Medicine and the American Heart Association," *Circulation*, vol. 116, no. 9, pp. 1083-1093, 2007.

[96] B. U. Kohler, C. Hennig, and R. Orglmeister, "The principles of software QRS detection," *IEEE Eng. Med. Biol. Mag.*, vol. 21, no. 1, pp. 42-57, 2002.

[97] U. R. Acharya, K. P. Joseph, N. Kammathal, C. M. Lim, and J. S. Suri, "Heart rate variability: a review," *Med. Biol. Eng. Comput.*, vol. 44, no. 12, pp. 1031-1051, 2006.

[98] G. G. Berntson, J. T. Bigger, Jr. D. L. Eckberg, P. Grossman, P. G. Kaufmann, M. Malik, H. N. Nagaraja, S. W. Porges, J. P. Saul, P. H, Stone, and M. W. van der Molen, "Heart rate variability: origins, methods, and interpretive caveats," *Psychophysiology*, vol. 34, no. 6, pp. 623-648, 1997.

[99] C. M. van Ravenswaaij – Arts, L. A. Kollee, J. C., Hopman, G. B. A. Stoelinga, and H. P. van Geijn "Heart rate variability," *Ann. Intern. Med.*, vol. 118, no. 6, pp. 436-447, 1993.

[100] N. S. Davidson, S. Goldner, and D. I. McCloskey, "Respiratory modulation of barareceptor and chemoreceptor reflexes affecting heart rate and cardiac vagal efferent nerve activity," *J. Physiol.*, vol. 259, no. 2, pp. 523-30, 1976.

[101] S. Akselrod, D. Gordon, J. B. Madwed, N. C. Snidman, D. C. Shannon, and R. J. Cohen, "Hemodynamic regulation: investigation by spectral analysis," *Am. J. Physiol.*, vol. 249, no. 4 Pt 2, pp. H867-875, 1985.

[102] P. M. McCabe, B. G., Yongue, P. K. Ackles, and S. W. Porges, "Changes in heart period, heart-period variability, and a spectral analysis estimate of respiratory sinus arrhythmia in response to pharmacological manipulations of the baroreceptor Reflex in cats," *Psychophysiology*, vol. 22, no. 2, pp. 195-203, 1985.

[103] C. Julien, "The enigma of Mayer waves: facts and models," *Cardiovasc. Res.*, vol. 70, no. 1, pp. 12-21, 2006.

[104] J. B. Madwed, P. Albrecht, R. G. Mark, and R. J. Cohen, "Low-frequency oscillations in arterial pressure and heart rate: a simple computer model," *Am. J. Physiol.*, vol. 256, no. 6 Pt 2, pp. H1573-1579, 1989.

[105] B. Pomeranz, R. J. Macaulay, M. A. Caudill, I. Kutz, D. Adam, D. Gordon, K. M. Kilborn, A. C. Barger, D. C. Shannon, R. J. Cohen and et. al., "Assessment of autonomic

function in humans by heart rate spectral analysis," *Am. J. Physiol.*, vol. 248, no. 1 Pt 2, pp. H151-153, 1985.

[106] R. I. Kitney, "An analysis of the nonlinear behaviour of the human thermal vasomotor control system," *J. Theor. Biol.*, vol. 52, no. 1, pp. 231-248, 1975.

[107] M. Rosenbaum, and D. Race, "Frequency-response characteristics of vascular resistance vessles," *Am. J. Physiol.*, vol. 215, no. 6, pp. 1397-1402, 1968.

[108] A. Lindqvist, P. Parviainen, P. Kolari, J. Tuominen, I. Valimaki, K. Antila, and L. A. Laitinen, "A non-invasive method for testing neural circulatory control in man," *Cardiovasc. Res.*, vol. 23, no. 3, pp. 262-272, 1989.

[109] M. Akay, "Nonlinear biomedical signal processing vol. II: dynamic analysis and modelling," *Wiley-IEEE Press*, 2000.

[110] Y. Wang, and Y. Zhang, "The effects of exercises on the relationship between pulse transit time and arterial blood pressure," *Proc. 27th IEEE EMBS*, 2005.

[111] K. Iwasaki, R. Zhang, J. H. Zuckerman, and B. D. Levine, "Dose-response relationship of the cardiovascular adaption to endurance training in healthy adults: how much training for what benefit?" *J. Appl. Physiol.*, vol. 95, no. 4, pp. 1575-1583, 2003.

[112] S. W. Farrell, J. B. Kampert, H. W. Kohl, 3rd, C. E. Barlow, C. A. Macera, R. S. Jr. Paffenbarger, and L. W. Gibbons, "Influences of cardiorespiratory fitness and other precursors on cardiovascular disease and all-cause mortality in men and women," *Med. Sci. Sports. Exerc.*, vol. 30, no. 6, pp. 899-905, 1998.

[113] P. T. Williams, "Relationships of heart disease risk factors to exercise quantity and intensity," *Arch. Intern. Med.*, vol. 158, no. 3, pp. 237-245, 1998.

[114] F. Quigley, "A survey of the causes of sudden death in sport in the Republic of Ireland," *Br. J. Sports. Med.*, vol. 34, no. 4, pp. 258-261, 2000.

[115] S. Hu, J. Zheng, and V. Azorin Peris, "A study of opto-physiological modelling to quantify tissue absorbance in imaging photoplethysmography," *Proc. 32nd IEEE EMBS*, pp. 5776-5779, 2010.

[116] J. Zhang, "Opto-physiological modelling of imaging photoplethysmography," *Loughborough University, Doctoral Dissertation*, 2010.

[117] J. M. Bland, and D. G. Altman, "Statistical methods for assessing agreement between two methods of clinical measurement," *Lancet*, vol. 1, no. 8476, pp. 307-310, 1986.

[118] I. M. Lee, C. C. hsieh, and R. S. Paffenbarger, Jr., "Exercise intensity and longevity in men, The Harvard Alumni Health Study," *JAMA*, vol. 273, no. 15, pp. 1179-1184, 1995.

[119] J. N. Morris, R. Pollard, M. G. Everitt, S. P. W. Chave, and A. M. Semmence, "Vigorous exercise in leisure-time: protection against coronary heart disease," *Lancet*, vol. 316, no. 8206, pp. 1207-1210, 1980.

[120] T. A. Lakka, J. M. Venalainen, R. Rauramaa, R. Salonen, J. Tuomilehto, and J. T. Salonen, "Relation of leisure-time physical activity and cardiorespiratory fitness to the risk of acute myocardial infraction," *N. Engl. J. Med.*, vol. 330, no. 22, pp. 1549-1554, 1994.

[121] A. G. Shaper, G. Wannamethee, and R. Weatherall, "Physical activity and ischaemic heart disease in middle-aged British men," *Br. Heart J.*, vol. 66, no. 5, pp. 384-394, 1991.

[122] J. Pekkanen, A. Nissinen, B. Marti, J. Tuomilehto, S. Punsar, and M. Karvonen, "Reduction of premature mortality by high physical activity: a 20-year follow-up of middle-aged Finnish men," *Lancet*, vol. 1, no. 8548, pp. 1473-1477, 1987.

[123] R. R. Pate, M. Pratt, S. N. Blair, W. L. Haskell, C. A. Macera, C. Bouchard, D. Buchner, W. Ettinger, G. W. Heath, A. C. King, et. al., "Physical activity and public health: A recommendation from the Centres for Disease Control and Prevention and the American College of Sports Medicine," *JAMA*, vol. 273, no. 5, pp. 402-407, 1995.

[124] S. Hales, "Statistical essays: Containing haemastaticke: or. An account of some hydraulic and hydrostatical experiments made on the blood and blood-vessels of animals," *London: W. Innys, R. Manby, and T. Woodward.*, 1733.

[125] S. Akselrod, D. Gordon, J. B. Madwed, N. C. Snidman, D. C. Shannon, and R. J. Cohen, "Hemodynamic regulation: investigation by spectral analysis," *Am. J. Physiol.*, vol. 249, no. 4 Pt 2, pp. H867-875, 1985.

[126] B. M. Sayers, "Analysis of heart rate variability," *Ergonomics*, vol. 16, no. 1, pp. 17-32, 1973.

[127] I. Constant, D. Laude, I. Murat, and J. L. Elghozi, "Pulse rate variability is not a surrogate for heart rate variability," *Clin. Sci. (London)*, vol. 97, no. 4, pp, 391-397, 1999.

[128] M. Nitzan, A. Babchenko, B. Khanokn, and D. Landau, "The variability of photoplethysmographic signal – a potential method for the evaluation of the autonomic nervous system," *Physiol. Meas.*, vol. 19, no. 1, pp. 93-102. 1998.

[129] R. Furlan, S. Guzzetti, W. Crivellaro, S. Dassi, M. Tinelli, G. Baselli, S. Cerutti, F. Lombardi, M. Pagani, and A. Malliani, "Continuous 24-hour assessment of the neural regulation of systemic arterial pressure and RR variabilities in ambulant subjects," *Circulation*, vol. 81, no. 2, pp. 537-547, 1990.

[130] A. Johansson, P. A. Oberg, and G. Sedin, "Monitoring of heart and respiratory rates in newborn infants using a new photoplethysmographic technique," *J. Clin. Monit. Comput.*, vol. 15, pp. 461-467, 1999.

[131] L. Nilsson, A. Johansson, and S. Kalman, "Monitoring of respiratory rate in postoperative care using a new photoplethysmographic technique," *J. Clin. Monit. Comput.*, vol. 16, pp. 309-315, 2000.

[132] M. Nitzan and H. Friedman, "Respiration-induced changes in tissue blood volume distal to occluded artery, measured by photoplethysmography," *J. Biomed. Opt.*, vol. 11, pp, 040506, 2006.

[133] H. Tsuji, F. J. Venditti, Jr., E. S. Manders, J. C. Evans, M. G. Larson, C. L. Feldman, and D. Levy, "Reduced heart rate variability and mortality risk in an elderly cohort. The Framingham Heart Study," *Circulation*, vol. 90, no. 2, pp. 878-883, 1994.

[134] A Algra, J. G. Tijssen, J. R., Roelandt, J. Pool, J. Lubsem, "Heart rate variability from 24-hour electrocardiography and the 2-year risk for sudden death," *Circulation*, vol. 88, no. 1, pp. 180-185, 1993.

[135] C. K. Peng, S. V. Buldyrev, A. L. Goldberger, S. Havlin, F. Sciortino, M. Somons, H. E. Stanley, "Long-range correlations in nucleotide sequences," *Nature*, vol. 356, no. 6365, pp. 168-170, 1992.

[136] C. K. Peng, S. Havlin, H. E. Stanley, and A. L. Goldberger, "Quantification of scaling exponents and crossover phenomena in nonstationary heartbeat time series," *Chaos*, vol. 5, no. 1, pp. 82-87, 1995.

[137] C. K. Peng, J. Mietus, J. M. Hausdorff, S. Havlin, H. E. Stanley, and A. L. Goldberger, "Long-range anticorrelations and non-Gaussian behaviour of the heartbeat," *Phys. Rev. Lett.*, vol. 70, no. 1, pp. 1343-1346, 1993.

[138] P. Bak, C. Tang, and K. Wiesenfeld, "Self-organized criticality: an explanation of the 1/f noise," *Phys. Rev. Lett.*, vol. 59, no. 4, pp. 381-384, 1987.

[139] J. M. Beggs, "The criticality hypothesis: how local cortical networks might optimize information processing," *Philos, Transact. A Math. Phys. Eng. Sci.*, vol. 366, no. 1864, pp. 329-343, 2008.

[140] P. Perakakis, M. Taylor, E. Martinez-Nieto, I. Revithi, and J. Vila, "Breathing frequency bias in fractal analysis of heart rate variability," *Biol. Psychol.*, vol. 82, no. 1 pp. 82-88, 2009.

[141] F. U. Mattace-Raso, A. Hofman, G. C. Verwoert, J. C. M. Witteman, I. Wilkinson, John Cockcroft, C. McEniery, Yasmin, S. Laurent, P. Boutouyrie, E. Bozec, T. W. Hansen, C. Torp-Pedersen, et. al., "Determinants of pulse wave velocity in healthy people and in the presence of cardiovascular risk factors: 'establishing normal and reference values'," *Eur. Heart J.*, vol. 31, no. 19, pp. 2338-2350, 2010.

[142] E. D. Lehmann, K. D. Hopkins, and R. G. Gosling, "Assessment of arterial dispensability by autonomic pulse wave velocity measurement," *Hypertension*, vol. 27, no. 5, pp. 1188-1191, 1996.

[143] S. Laurent, J. Cockcroft, L. van Bortel, P. Boutouyrie, C. Giannattasio. D. Hayoz, B. Pannier, C. Vlachopoulos, I. Wilkinson, and H. Struijer-Boudier, "Expert consensus document on arterial stiffness: methodological issues and clinical applications," *Eur. Heart J.*, vol. 27, no. 21, pp. 2588-2605. 2006.

APPENDICES

The following appendices have been included:

I. Other publications during the joint PhD programme between Loughborough University (LU) and Shanghai Jiao Tong University (SJTU).

II. Volunteer information sheet and anonymous lab trial form.

III. Front panel of the camera configuration software (Mikrotron GmbH, Unterschleissheim, Germany).

IV. Front panel of the image acquisition software (SiliconSoftware GmbH, Mannheim, Germany).

I. OTHER PUBLICATIONS DURING THE JOINT PHD PROGRAMME BETWEEN LU AND SJTU*

[1] **Y. SUN,** S. Hu, J. Chambers, Y. Zhu, S. Tong, "A graph theoretic analysis of cortical functional connectivity of depressed patients on the basis of EEG measurements", ***Proc. of 33rd IEEE EMBS***, (In press).

[2] **Y. SUN**, H. Zhang, T. Feng, Y. Qiu, Y. Zhu, S. Tong, (2009), "Early cortical connective network relating to audiovisual stimulation by partial directed coherence analysis", ***IEEE Trans. Biomed. Eng.***, vol. 56(11pt2), pp: 2721-2724.

[3] **Y. SUN**, Y. Li, Y. Zhu, X. Chen, S. Tong, (2008), "Electroencephalographic difference between depressed and control subjects: an aspect of interdependence analysis", ***Brain Res. Bull.***, vol. 76(6), pp: 559-564.

[4] H. Zhang, **Y. SUN**, J. Yan, J. Wang, Y. Qiu, Y. Zhu, S. Tong, (2009), "Cortical interactive network during mental rotation of Chinese character", ***Neurosci. Lett.***, vol. 461(2), pp: 185-189.

* Before coming to Loughborough University, I was a PhD candidate in Shanghai Jiao Tong University, majoring in computational neuroscience. During the PhD study in SJTU, three peer-reviewed journal papers and one international conference article have been published. In 2009, I came to LU to pursuit another PhD degree according to the Joint PhD program agreed by both universities, majoring in Photonics Engineering and Health Technology Research. Relative academic outputs contribute the context of the thesis.

II. VOLUNTEER INFPRMATION SHEET AND ANONYMOUS LAB TRIAL FORM

Photonics Engineering and Health Technology Research

Loughborough University

Cycling exercise influence on cardiovascular system

Participant Information and anonymous lab trial

You are being invited to take part in a study concerning the influence of short-term exercise on cardiovascular system. Before you decide whether to join, it is important for you to understand why the research is being done and what is involved. Please take your time to read the following information. If there is anything that is still not clear, or if you would like more information, please feel free to ask.

What is the purpose of the study?

Imaging photoplethysmography (IPPG) is a simple and low-cost optical technique that can be widely employed to remotely detect blood volume changes in the micro-vascular bed of tissue. A new IPPG setup is proposed to detect the PPG signals remotely (>20 cm) using infrared light-source and to demonstrate the influence of short-term exercise on cardiovascular system.

Who is doing this research and why?

The present study will be carried out by Mr. Yu SUN, and supervised by Dr. Sijung Hu (Leader of Photonics Engineering and Health Technology Research Group). This study will be carried out in W260, Sir David Davies Building during the period of 10th June – 10th July 2010. This study is also a part of research project funded by the Department of Health, UK.

Can I change my mind after I have already taken part in it?

YES! After you have read this information sheet and asked any question about this study, an anonymous lab trial sheet would be collected from you within which some personal information about you is needed. However, you can cancel your participation at anytime without any reasons.

What will you need to do?

This experiment will take place in the Sir David Davis building at Loughborough University. During the experiment, the following measurements are taken. The procedures to perform each of them are described below (the whole session takes **LESS than 1 hour**).

---- Blood pressure and heart beat measurements

---- Experimental conditions, i.e., ambient temperature, and humidity.

---- Experiment 1, rest condition

---- Experiment 2, exercise level 1

---- Experiment 3, exercise level 2

---- Experiment 4, recovery condition

(1) **Blood pressure and heart beat measurements:** Before measurements taken from the contact PPG (CPPG)/IPPG, the parameters of blood pressure and heart beat are obtained through a clinically approved blood pressure monitor (Omron M6). In total three times, the parameters should be obtained with 0.5 min in-between rest period to minimise the variation.

(2) **Environment parameters monitor:** The measurements of ambient temperature and humidity are taken before the experiments.

(3) **Experiment 1:** The signals from CPPG and IPPG are recorded for 0.5 min simultaneously in a dark room when subject seated in a comfortable condition with their palm/forearm facing the camera.

(4) **Experiment 2:** The signals from CPPG and IPPG are obtained for 0.5 min simultaneous after subject performs a ~10 min cycling (15 km/h) on a cycling machine (Model: PowerTrek XR-580 recumbent exercise bike, PowerTrek, UK) in the lab. Just after the exercise, the blood pressure and heart beat are also collected.

(5) **Experiment 3:** The signals from CPPG and IPPG are obtained for 0.5 min simultaneously in a dark room after subjects fully rest from Experiment 2, then perform another ~10 min cycling (25 km/h).

(6) **Experiment 4**: The signals from CPPG and iPPG are simultaneously obtained for another 0.5 min 10 min after the Experiment 3 to assess the cardiovascular system during the recuperate situation.

Is there anything I need to do or to refrain from doing before the experiment?

Yes, you will need to complete an informed consent form provided by us. Also you are advised to refrain from caffeine, alcohol drinking and strenuous exercise within 2 hours before the test.

What personal information will be required from me?

You will fill out an anonymous personal information sheet at the start of the study.

Are there any risks in participating?

No, the trial is completely safety. The protocol is in direct accordance with the Medicines and Healthcare products Regulatory Agency (MHRA) guideline and the University Health & Safety Regulations as well.

Two exercise levels would be manipulated in the study; the participant will be required to cycle at a speed approximately 15 km/h (level 1) on a cycling machine in the lab with digital display to tell the speed and heart beat. After fully resting from the first exercise, a higher level exercise (level 2) requiring the participant to cycle at approximately 25 km/h, would be carried out.

Who could access the data?

All data will be stored securely on a private computer which could be accessed to limit research members within the Photonics Engineering and Health Technology Research Group.

Will my taking part in this study be kept confidential?

Yes, your privacy and confidentiality are important to us. Loughborough University has sought advice from the Information Commissioner to insure that this research study complies fully with the requirements of the Data Protection Act 1998. The results of this study will be published following independent review but no individually-identifying data will ever be published.

Any questions?

If you have any quarries and need further information, please contact:

Mr. Yu SUN Tel: +44 (0) 1509 227058 E-mail: Y.Sun2@lboro.ac.uk

Dr. Sijung Hu Tel: +44 (0) 1509 227058 E-mail: S.Hu@lboro.ac.uk

What if I am not happy with how the research was conducted?

The Loughborough University has a policy relating to Research Misconduct and Whistle Blowing which is available online at http://www.lboro.ac.uk/admin/committees/ethical/

Photonics Engineering and Health Technology Research

Loughborough University

ANONYMOUS LAB TRIAL

Trial Number:_____

Title:

Objective:

Participant Name: **ANONYMOUS**

Gender: M/F, Age:_____*yrs* Weight:_____*kg* Height:_____*cm*

Blood Pressure: SYS:_____*mmHg* DIA:_____*mmHg* Pulse:_____*bpm*

Special interests:

Cardiovascular disease: Yes/No.

Diabetics: Yes/No. Smoking: Yes/No, If yes, _____yrs.

Note: *Refrain from caffeine, smoking, alcohol drinking and strenuous exercise within 2 hours before this test.*

Trial conditions:

Ambient temperature: _____°C. Relative humidity:_____%

Duration of the trial: Start : _____ Finish : _____ Duration: _____

Additional Comments

I give my consent for Loughborough University to record, process and validate clinical trial information and sensitive clinical data in line with the Data Protection Act 1998 and all other legislative provisions. My consent is conditional upon Loughborough University complying with its legal duties and obligations relating to the recording and use of this information.

Signature_____ Date_____

III. FRONT PANEL OF CAMERA CONFIGURATION SOFTWARE (1)

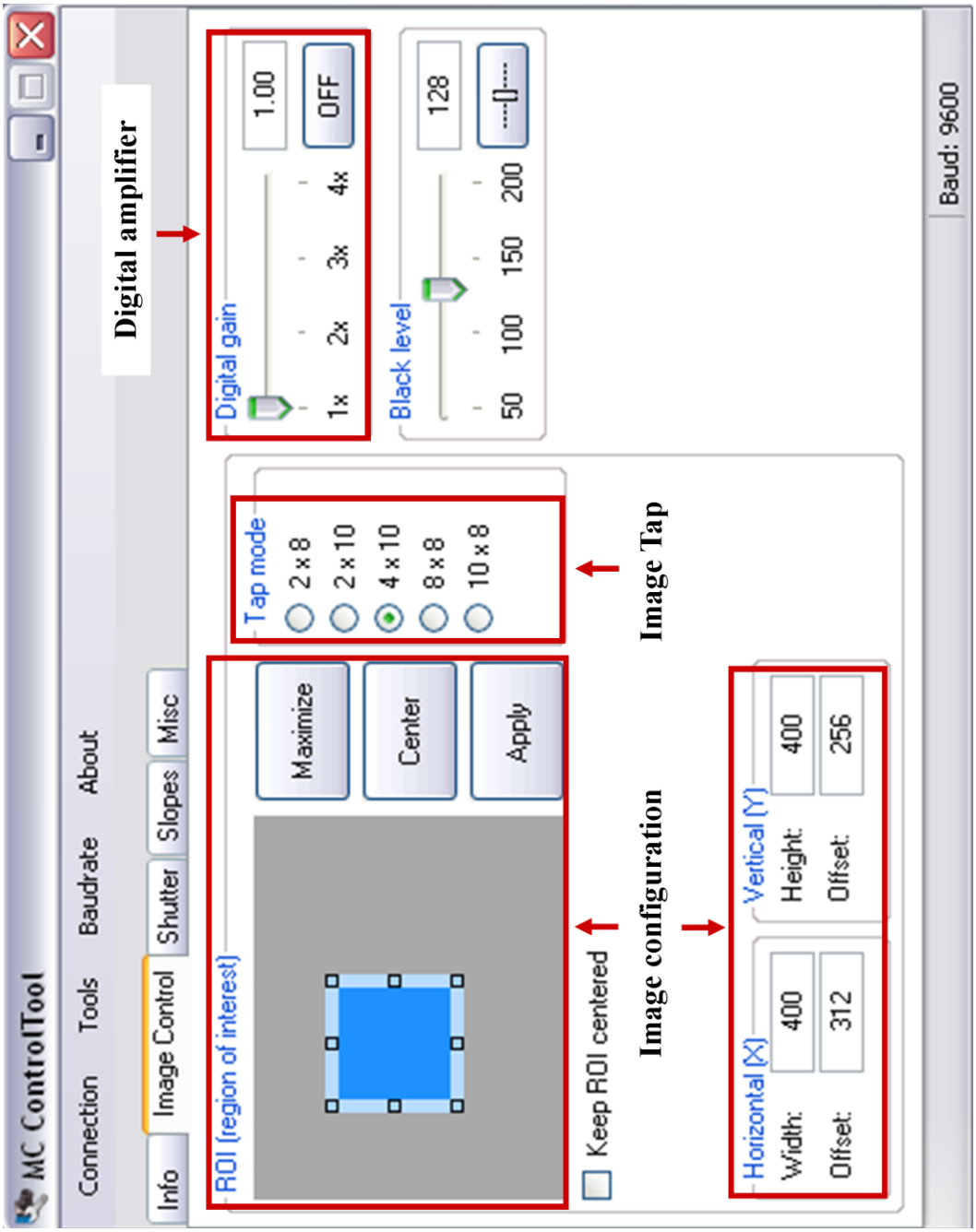

III. FRONT PANEL OF CAMERA CONFIGURATION SOFTWARE (2)

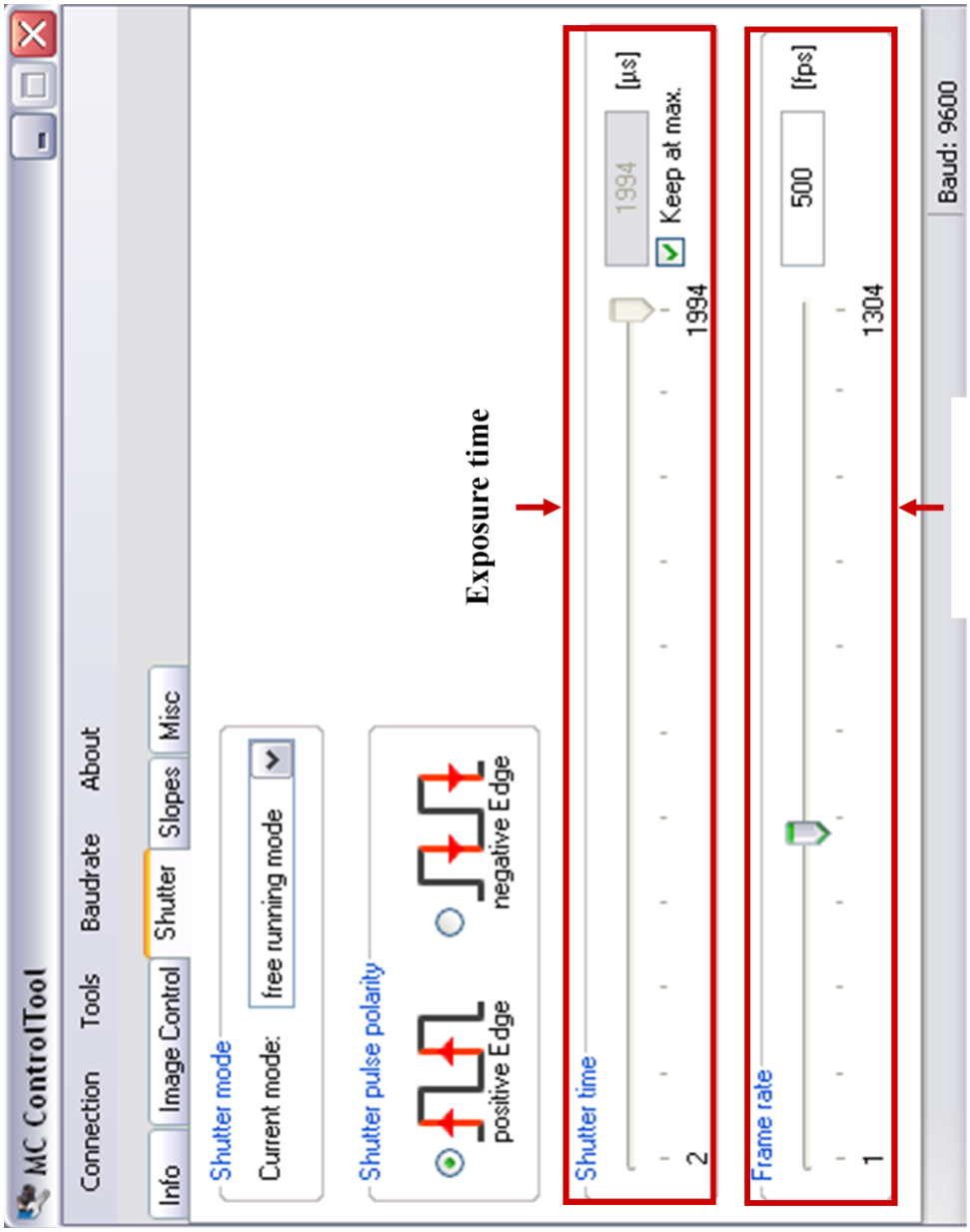

IV. FRONT PANEL OF THE IMAGE ACQUISITION SOFTWARE